FOSSIL ENERGY

DOE/BC/15203-3
(OSTI ID: 790861)

A METHODOLOGY TO INTEGRATE MAGNETIC RESONANCE AND ACOUSTIC MEASUREMENTS FOR RESERVOIR CHARACTRIZATION

Annual Report
April 2000-April 2001

By:
Jorge O. Parra
Chris L. Hackert
Hughbert A. Collier
Michael Bennett

Date Published: February 2002

Work Performed Under Contract No. DE-AC26-99BC15203

Southwest Research Institute
San Antonio, Texas

National Energy Technology Laboratory
National Petroleum Technology Office
U.S. DEPARTMENT OF ENERGY
Tulsa, Oklahoma

DOE/BC/15203-3
Distribution Category UC-122

A Methodology to Integrate Magnetic Resonance and Acoustic Measurements for Reservoir Characterization

By
Jorge O. Parra
Chris L. Hackert
Hughbert A. Collier
Michael Bennett

February 2002

Work Performed Under DE-AC26-99BC15203

Prepared for
U.S. Department of Energy
Assistant Secretary for Fossil Energy

Purna Halder, Project Manager
National Petroleum Technology Office
P.O. Box 3628
Tulsa, OK 74101

Prepared by
Southwest Research Institute
6220 Culbera Road
San Antonio, TX 78238

TABLE OF CONTENTS

TABLE OF CONTENTS (cont'd)

FOREWORD AND ACKNOWLEDGMENTS

The work reported herein represents the second year of development work on a methodology to interpret magnetic resonance and acoustic measurements for reservoir characterization. Project coordination and supervision, as well as the integration of acoustic, NMR and petrophysical data, were performed by Dr. Jorge Parra, Applied Physics Division, Southwest Research Institute. Dr. Chris Hackert and Mr. Stan Silvus, of the same organization, performed computer modeling and processing of acoustic image data and SEM core analysis, respectively. Dr. Hughbert Collier from Collier Consulting was the liaison between the South Florida Water Management District, Core Labs, and Baker Atlas. The ultrasonic and NMR core measurements were performed by Core Laboratories, and the well log data acquisition was conducted by Baker Atlas.

The assistance of Mr. Purna Halder, project manager from the U.S. Department of Energy, is gratefully acknowledged. We thank Springfield Exploration, especially Ms. Mary Irwin de Mora, for providing in-kind contribution to the project. Next, we thank Chevron Production USA, in particular Dr. Mike Morea, for his contribution of Buena Vista Hills field data. Also, we thank Mr. Michael Bennett, South Florida Water Management District, who is manager of the Speciality Geophysical Logging Project. This organization provided the ultrasonic and NMR core measurements and well logs for the project. In addition, Mr. Bennett revised the geology and the results of the petrophysics.

The Siberia Ridge data used in this study was collected by Schlumberger Holditch-Reservoir Technologies, Inc., for the "Emerging Resources in the Greater Green River Basin" project, GRI contract 5094-210-3021. We thank the GRI project manager Mr. C. Brandenburg for his help.

This report is organized in four parts: (1) introduction; (2) integration of NMR and acoustic data with core imaging to characterize vuggy carbonates; (3) technology transfer activities; and (4) follow-on work for Phase III.

I. INTRODUCTION AND SUMMARY OF THE PROJECT

A. Background

Over the years, traditional reservoir characterization techniques have evolved into multidisciplinary processes. In particular, the integration of engineering, geoscientific, and geological data over multiple scales has been used to characterize reservoirs by honoring petrophysical well log data as well as sedimentological models.

Recently, great effort has been dedicated to the integration of well logs with seismic data. Conventional seismic measurements have been used to delineate reservoir structures in the lateral extent, but vertical resolution is limited. And although seismic data is routinely and effectively used to estimate reservoir structure, it plays no role in the essential task of estimating rock physical properties, which are derived from well logs. Simultaneous analysis of seismic and borehole data leads to better estimates of rock physical property distributions in comparison with estimates generated from seismic or well log data alone.

Accurate reservoir description and simulation are dependent on measures of properties such as porosity, permeability, fluid viscosity, and fluid saturation. Porosity is routinely available from wireline log data, which, in conjunction with 3-D seismic data, can be used to generate excellent reservoir porosity models. Acoustic measurements based on Stoneley wave attenuation have been used to indirectly extract information about formation permeability. In this case, attenuation measurements are affected by the heterogeneity and viscoelasticity of the rock, rather than fluid flow interactions alone (or intrinsic properties of the reservoir such as permeability and porosity). To use attenuation and dispersion measurements to predict flow properties, the effects of scattering must be understood so velocity measurements can be corrected for such effects.

Nuclear magnetic resonance (NMR) logging techniques do provide vertically continuous pore-size distribution, but they do not measure permeability directly, nor are they foolproof in distinguishing the amount of oil in an oil-water mixture. Combined with other measurements (resistivity, etc.), reasonable permeability models can be obtained. The permeability models at the borehole scale can be integrated with surface seismic data to map flow units at the interwell scale.

The integration of NMR well log data and acoustic data has the potential to provide reservoir parameters for constant velocity-permeability models at the borehole scale, which can then be used to map reservoir parameters at interwell scales (crosswell seismic and 3D surface scales). This requires properly calibrated well logs as well as petrophysical information, which facilitate an understanding of heterogeneity and fluid flow effects on the acoustic signal.

The objective of this project is to develop an advanced imaging method, including pore scale imaging, to integrate NMR techniques and acoustic measurements to improve predictability of the pay zone in hydrocarbon reservoirs. We are accomplishing this by extracting the fluid property parameters using NMR laboratory measurements and the elastic parameters of the rock matrix from acoustic measurements to create poroelastic models of different parts of the

reservoir. Laboratory measurement techniques and core imaging are being linked with a balanced petrographical analysis of the core and theoretical modeling. These concepts will allow us to relate intrinsic acoustic properties with fluid flow interactions at the pore, core, and borehole scales, and to establish the use of acoustic and NMR data to define flow units to eventually provide input to reservoir simulation modeling at interwell scales. The laboratory measurements are being compared with petrographic and imaging analysis results to determine the relative roles of petrographic features such as porosity type (micro- and macro-porosity and vuggy porosity), mineralogy, texture, and distribution of cement in creating permeability heterogeneity.

In this second annual report we include a comprehensive study of the carbonate reservoir rock from South Florida. We analyzed the reservoir formation at the pore, core and borehole scales, including processing thin sections, scanning electron microscope (SEM) and computed tomography (CT) images with petrography. We also analyzed and processed NMR and acoustic core measurements to implement calibration techniques for NMR and acoustic well logs. Simulations of NMR signatures based on pore size distribution obtained from image processing are used to explain observed NMR signatures. In addition the relation of P-wave velocity to permeability, based on flow units at the core scale, is developed to predict dispersion and attenuation at the borehole scale, allowing us to evaluate the applicability of sonic logs in detecting vuggy porosity in the formation. We include a technology transfer section consisting of two manuscripts submitted for publication in peer review journals.

B. Summary of Project Efforts to Date

1. Project Phase II

Based on standard core measurements and image analysis, we determined that the carbonate rock from South Florida is formed by micro-porous, macro-porous and vuggy porosity. The thin section analysis and SEM photomicrographs provided information on the matrix porosity and the CT scan image provided information on the vuggy porosity. We constructed vuggy porosity models to calculate synthetic ultrasonic responses based on the finite difference method, and we compared the synthetic and ultrasonic data. The results explain the velocity changes associated with vugs in the carbonate rock at the core scale. We used these modeling results to explain the scattering of velocity versus permeability relations based on core measurements for different flow units of the carbonate aquifer. The velocity correlated very well with the permeability for each carbonate flow unit. To determine whether we could assess the degree of connectivity between vugs or between the matrix and the vugs based on acoustic data, we calculated the squirt-flow lengths using a poroelastic model by fitting the calculated and observed velocities at the ultrasonic dominant frequency of 250 kHz. The results showed a good correlation between the squirt-flow lengths and the increase in permeability for each flow unit. In addition, we calculated dispersion and attenuation curves based on core data in the frequency range of sonic logs. We found that the attenuation is directly related to the fluid flow between the matrix and the vugs. The sonic log data therefore has the potential to estimate whether vugs contribute to permeability in the region surrounding the borehole, when coupled with an examination of the P-wave attenuation and dispersion.

Photographs of carbonate rock reveals that matrix and vuggy porosity are encountered in most of the cores in different proportions. To determine whether the matrix and/or the vugs are controlling permeability, one must understand the pore structure of the carbonate rock. For this purpose we used CT, SEM and optical microscope (OM) images to characterize two carbonate core samples containing vugs. 3D CT images were obtained for cores #7 and # 41 from well PCF-10. The CT images were processed and analyzed for the presence of vugs and to construct finite-difference based velocity models to determine sensitivity to the presence of vugs in the ultrasonic and acoustic responses. Thin sections were selected from the two cores to study matrix porosity, pore size distribution, and the effects of each on permeability. To support the results a petrographic analysis of cores #7 and #41 was conducted.

In addition, we analyzed NMR/ultrasonic core data to establish links between NMR and acoustics, and we introduced new concepts on relating FZI units with the Biot and squirt-flow mechanisms. The NMR analysis based on saturated and desaturated core measurements provided several T_2 cut-offs associated with the heterogeneous conditions of the reservoir rock. This information was used to implement software to calibrate NMR well logs, including the NMR well log from well PBF10 in South Florida. As a result we calculated new porosity and permeability logs and we compared them with the original NMR derived porosity and permeability based on a single T_2 cut-off that was derived by Western Atlas.

We further characterized the pore structure based on the processing of SEM, OM and CT scan data. The application was to produce synthetic NMR signatures to evaluate observed NMR well log signatures. In particular, we simulated the NMR response based on pore size distribution including the SEM, OM and CT scan scales. The main objective was to relate micro-porosity, macro-porosity, and the vuggy porosity with the NMR signature, and to determine how these type of porosities are related to permeability in the Florida carbonate aquifer. A second objective is to verify the NMR well log calibration.

Furthermore, to evaluate the suitability of sonic and dipole sonic data to image the heterogeneous carbonate, the phase velocity and attenuation of the vuggy carbonate rocks in the sonic log frequency were calculated based on pore and core scale data. The results suggested strong attenuation in the frequency range of monopole/dipole sonic. In this case the flow was associated with the connectivity between the vugs and the matrix. This analysis implies that sonic logs have the potential to capture fluid flow interactions between the matrix and the vugs. Specifically, the P-wave attenuation and phase velocity will capture the degree of connectivity between the matrix porosity and the vugs or the connectivity between vugs.

We recorded monopole and dipole sonic data in the PBF10 borehole that transects at the Florida aquifer. The objective was to extract Stoneley wave permeability from sonic logs and to compare that permeability with the NMR log-derived permeability to determine which technique is more suitable to use on a regular basis to characterize the aquifer. Since the Stoneley waves are sensitive to washout zones, and the small changes on the diameter of the borehole, and the PBF10 caliper log shows variability as a function of depth, the Stoneley wave permeability does not give good results. However, the P-wave events were easy to identify in the microseismograms. The next step is to produce synthetics based on the core data containing vugs and compare them with the

observed data to determine whether we can infer from the P-wave sonic data the degree of connectivity between vugs and between the matrix and vugs. To fully evaluate this concept we will use the NMR-derived permeability log, porosity log, density log, Vp and Vs logs.

2. Technical Transfer Activity

Since one of our goals is to transfer the technology to the oil and gas industry, we have submitted several manuscripts for publication. Two of these manuscripts (see Section III) include simulations and interpretation of field data based on the knowledge of the pore structure and the Biot/squirt-flow mechanisms.

The first manuscript has been accepted for publication in *Petrophysics*. It is titled "A poroelastic model with azimuthal anisotropy to analyze flow unit responses at the Siberia Ridge field, Greater Green River Basin." In it a modeling scheme is presented and applied to analyze the response of reservoir flow units to a variety of acoustic/seismic measurement techniques, and to determine the frequency band in which flow units can be observed and characterized. The model estimates attenuation in a broad frequency range to include sonic, crosswell, VSP, and 3D seismic scales. Because flow units in a reservoir are characterized by permeability, porosity, and fluid saturation, and because fluids are characterized by their viscosity, density, and velocity, we use the theory of poroelasticity. This theory provides the physics involved in the interactions between the fluid and the rock matrix as an acoustic wave propagates in the medium. Energy losses due to the relative movement of pore fluids and the rock matrix are described using the unified Biot and squirt-flow theory. We apply this theory to a layered poroelastic medium with azimuthal anisotropy to analyze whether flow units penetrated by a borehole can be detected at seismic scales (crosswell, VSP and 3D seismic). We model a sand-shale-coal sequence from the Siberia Ridge field, a tight gas sand reservoir located in Wyoming, as an example. The results give responses in the frequency domain containing the effect of scattering and intrinsic attenuation. By comparing total attenuation with scattering attenuation, we observe the differences associated with the flow units. Flow units can be identified because the increase in attenuation is due to the interaction of fluid flow with the rock matrix. The modeling results show scattering effects of shales and coals and demonstrate that coals control the scattering attenuation. The elastic attenuation is shown at all frequencies and the fluid flow effects are observed in the sonic and crosswell frequency ranges. This model study suggests that low frequency measurements such as 3D seismic would not be able to map fluid flow. Only borehole related seismic measurements have the potential to map fluid flow effects in tight gas sands at the Siberia Ridge field.

The second manuscript is titled "Characterization of fractured low Q zones at the Buena Vista Hills reservoir, California." In it we simulate a system of fractures by considering two scales: (1) squirt-flow length of less than 1 mm to represent flow in low permeability shales, and (2) squirt-flow length on the order of centimeters to represent fluid flow in fractures. Two types of fractures at the site are joint-like tectonic fractures and sigmoidal vein fractures. Their permeability of about 5 md and squirt-flow lengths between 1-2 cm predict a quality factor of about 20 that fits the observed Q in a Brown Shale zone. The Q was determined via velocity dispersion by integrating crosswell seismic data with well logs and cores. The permeable zones are associated with fractures having patchy saturation, with patches having dimensions of 1-2 cm.

II. INTEGRATION OF NMR AND ACOUSTIC DATA WITH CORE IMAGING TO CHARACTERIZE VUGGY CARBONATES

A. Summary

We integrated NMR and acoustic data at the core and borehole scales with core imaging to enhance the description of a reservoir in a complex carbonate aquifer in Palm Beach, South Florida. X-ray CT imaging of the core revealed a vuggy porosity, and the thin-section image provided information on the macro- and micro-porosity of the rock matrix. These two imaging techniques helped us determine pore size and shape distributions so we could relate the pore structure with permeability in carbonate rock samples. We created computer models using CT scan imaging to simulate ultrasonic data to analyze the effect of vugs on velocity and attenuation at the core scale, based on finite difference and stochastic solutions. The stochastic analysis suggested that there were two correlation lengths that characterize the core structure. The stochastic results and the finite difference models gave information on velocity variations due to vuggy porosity in the cores. These results were used to explain the relationship between P-wave velocity and permeability at the core scale of the carbonate aquifer. NMR core data were used to determine the different T_2 cut-offs for calibrating NMR logs, and a relaxivity grouping method was used to calibrate the NMR well logs and determine permeability and porosity at the borehole scale. Pore size distributions based on core images were used to produce synthetic T_2 distributions to refine T_2 cut-offs, which in turn led to better estimates of the matrix permeability from NMR well logs. Velocities from sonic logs were correlated with NMR-derived permeability and porosity for the different flow units in the carbonate aquifer, and the resulting equations were compared to those derived at the core scale, to devise a scaling relationship for mapping permeability at the interwell scale from velocity images based on crosswell seismic measurements.

B. Introduction

The objective of this study is to determine the feasibility of applying NMR and acoustic measurement techniques to relate velocity with porosity and permeability in carbonate rock at the core/borehole scales, and to predict these reservoir parameters at the interwell scale. To accomplish the objective we used core and well log data from well PBF10, which intercepts a brackish-water Floridan aquifer, South central Palm Beach County, Florida.

The carbonate rock of the Florida aquifer in South Florida, in general, have broad pore size distributions, from microcrystalline to large vugs. These pore spaces and their geometries are crucial to an understanding of hydrocarbon reservoir characterization and hydrological and environmental issues including those related to aquifers, which are often found in carbonate rock. The pore system of carbonates has been recognized as physically and genetically complicated by Choquette and Pray (1970), who published a review on the geological nomenclature and classification of carbonates and introduced terminology that emphasizes interrelations between porosity and other geological features. In Choquette and Pray's review, seven dominant porosity types in sedimentary carbonates were considered. These porosity types are inter particle, intra particle, inter crystal, moldic, fenestral, vug and fracture. The Florida aquifer in South Florida contains all these types of porosity except fracture porosity, but vugs are the most important. In most

of the cores the vugs were recognized visually; both separated vugs and touching vugs were observed in the cores. Touching-vug pore geometries usually consist of large interconnected cavities and channels (see Choquette and Pray, 1970). The typical vug diameter is about 16 mm in cores from well PBF10. The cores are longer in the vertical direction than in the horizontal direction.

Lucia (1983) extended the classification made by Choquette and Pray (1970) by grouping rocks with similar petrophysical characteristics. Lucia (1983) emphasized petrophysical aspects of carbonate pore space, as did Archie (1952). However, by comparing rock-fabric descriptions with laboratory measurements of porosity, permeability, capillary and Archie m-values, Lucia (1983) showed that the most useful classification of pore types for petrophysical purposes is that of pore space between grains or crystals, called interparticle porosity, and all other pore space, called vuggy porosity. Vuggy pore space was further subdivided by Lucia (1983) into two groups depending on how the vugs are interconnected: (1) vugs interconnected only through the interparticle pore network are separate vugs, and (2) vugs that form an interconnected pore system are touching vugs. We attribute to Lucia and Archie the concept that pore-size distribution controls permeability and saturation and that pore-size distribution is related to rock fabric.

Anselmetti et al. (1998) described a method of characterization of carbonate samples based on quantitative observations from digital environmental SEM (ESEM) and OM thin section images. This approach has the advantage of avoiding descriptive bias by the geologist, but also has a disadvantage in that quantitative data obtained by image analysis are dependent on thin-section selection and field of view under the microscope.

Our approach includes thin section/SEM and X-ray CT data to characterize the carbonate pore space, with size varying by more than five orders of magnitude in the sample space. The CT method produces 3D images of the pore structure by revealing the vugs present in the core sample. In addition, we use NMR core measurements to produce T_2 distributions based on saturated and unsaturated samples. These data provides the pore size distributions of a core sample and the capillary-bounded water in the core. Several measurements are made to apply the relaxivity grouping technique to estimate the T_2 cut-offs for well log calibration in carbonates. Thin section/SEM image analysis is used to confirm quantitatively/qualitatively the expected relation between NMR T_2 signatures and pore size distributions.

The objective of the thin section/SEM, CT image, and core data analyses is to provide supporting information to evaluate whether the variable T_2 cut-off method can be used to calibrate NMR well logs for extracting porosity and permeability data to characterize vuggy carbonates.

In addition, our approach includes ultrasonic and acoustic data to evaluate whether the vuggy porosity can be characterized and detected in the region surrounding the borehole with sonic tools. Based on standard core measurements and image analyses, we constructed vuggy porosity models to calculate synthetic ultrasonic responses based on the finite difference method, and we compared the synthetic with the ultrasonic data. We used the modeling results to explain the scattering of velocity versus permeability relations based on core measurements for different flow units of the carbonate aquifer. To determine whether we can assess the degree of connectivity

between vugs or between the matrix and the vugs based on acoustic data, we calculated the squirt-flow lengths using poroelasticity . We calculated dispersion and attenuation curves based on core data in the frequency range of sonic logs to determine whether P-wave attenuation can be related to the fluid flow between the matrix and the vugs and to establish the application of sonic logs for estimating whether vugs contribute to permeability in the region surrounding the borehole.

Full waveform monopole sonic data (recorded in the PBF10 borehole intersecting the Florida aquifer) is used in the signal analysis. The original objective was to extract Stoneley wave permeability from sonic logs and compare Stoneley wave permeability to NMR-derived permeability to determine which technique is more suitable to use on a regular basis to characterize the aquifer. Since the Stoneley waves are sensitive to washout zones, and the PBF10 borehole has many washout zones, Stoneley wave permeability does not produce good results. However, the P-wave events are easy to identify in the microseismograms. Therefore, our next goal is to produce synthetics based on the core data containing vugs and compare them with the observed data to determine whether we can infer from the P-wave sonic data the degree of connectivity between vugs and between the matrix and vugs. To fully evaluate this concept we will use the NMR-derived permeability log, porosity log, density log, Vp and Vs logs and the lithology.

The present work is discussed in detail in the next six sections: (Section C) site geology, (Section D) pore and core scale images, (Section E) ultrasonic wave modeling and velocity analysis, (Section F) NMR core measurements and analysis, (Section G) NMR well log calibration, and (Section H) acoustic well log analysis.

C. Geology/Hydrology

1. Background Geology

The zone under study includes the Florida aquifer rock units comprising the Avon Park Limestone, the Ocala limestone, and the Suwannee Limestone. The rocks that form the Florida Aquifer system are between the Surficial Aquifer on the top and the boulder zone on the bottom. Figure 1 shows a generalized cross section of the typical stratigraphic relationship between the Florida Aquifer System and the adjacent strata (Gleason, 1984). The Surficial Aquifer System consists of sands, sandy and shelly limestones, sandstones and silts and contains water table and semi-confined aquifers. On the other hand, the Florida Aquifer System is a regionally extensive, deep, artesian limestone aquifer with generally high but variable transmissivity. As shown in Figure 1, the Hawthorn Group acts as a confining unit separating the Surficial Aquifer System from the underlying Florida Aquifer System.

Our study is based on well PBF10, which intercepts the Miocene Arcadia, the upper Eocene Ocala limestone, and the middle Eocene Avon Park formations. The Avon Park consists of highly microfossiliferous, cream-colored, chalky limestone and lies above the Oldsman Formation. The Lake City Formation is no longer used and is now referred to as the Avon Park Formation.

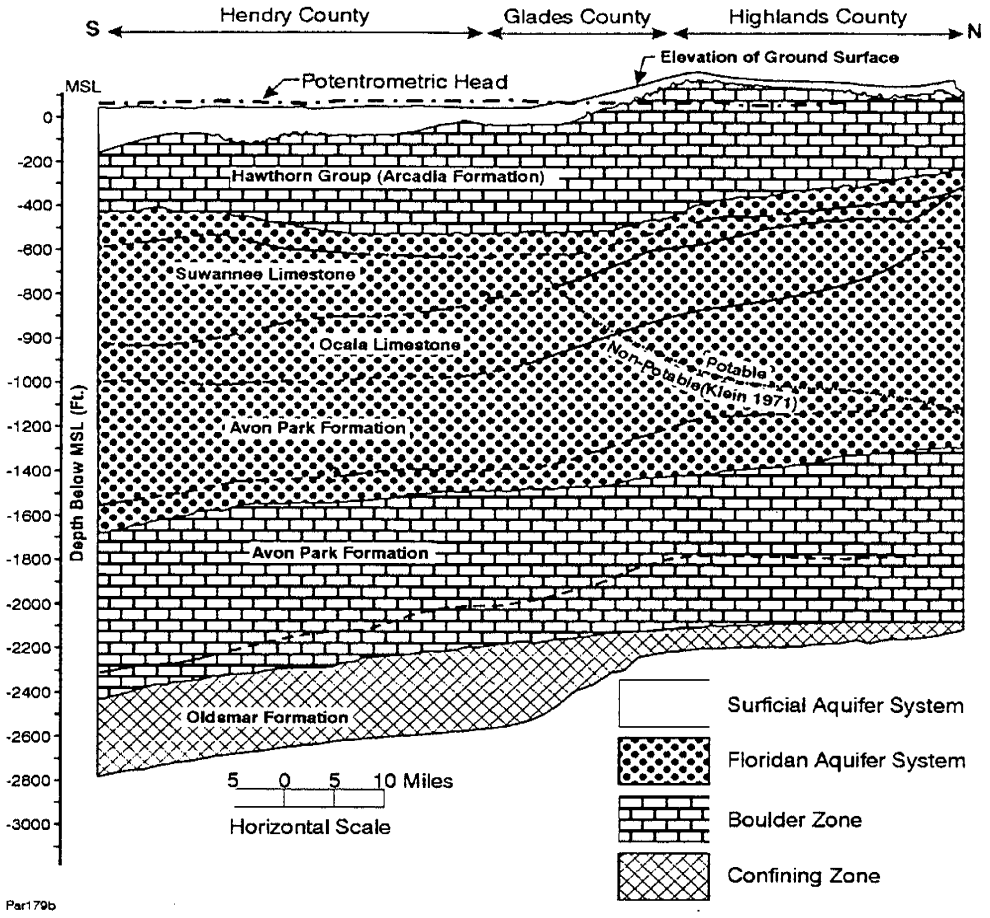

Figure 1. A generalized cross section of the typical stratigraphic relationship between the Florida Aquifer System and the adjacent strata.

The Avon Park Formation contains a distinctive faunal assemblage including various species of *Dictyoconus, Lituonella,* and *Fabularia.* The upper part of the Avon Park is a light brown to tan limestone or dolomite, which is distinctly different from the overlying lithologies in the Ocala Limestone. The base of the formation is a thick, non-fossiliferous, brown to dark brown, and fine to medium crystalline dolomite bed lying above the Oldsman Formation which contains highly carbonaceous carbonate units at its top in north Florida. These beds do not occur throughout south Florida. The lower boundary between the Avon Park and the Oldsman Formation is difficult to recognize because of localized dolomitization across the contact. However, both the upper and lower Avon Park contacts are identifiable on electrical logs. The Avon Park Formation ranges from 400 to 700 feet in thickness beneath south Florida.

The upper portion of the Ocala limestone is a white to very light gray or tan, soft, chalky coquina consisting predominantly of large foraminifera. The lower portion is a light cream colored limestone, generally harder than the upper unit, and commonly composed of small miliolid molds. Fossil species common in the upper unit include *Lepidocyclina* ocalana,

Heterostegina ocalana, and *Nummulities willcoxi*. The lower unit also contains these species, but smaller foraminifera, predominantly miliolids, are more abundant.

In south Florida, the Ocala Limestone is differentiated from other stratigraphic units as follows. The bottom part of the formation is a soft white to light gray limestone, in contrast to the hard tan dolomite and limestone of the underlying Avon Park Formation. Lithologically, the Ocala is a light gray to white to tan limestone that contains numerous large Foraminifera. It also contains beds of unlithified or poorly lithified lime mud. The Ocala has a maximum thickness of about 400 feet along the southwest Florida coast. It thins to the southeast and does not occur along much of the southeast coast, where it pinches out between the Oligocene Suwannee Limestone and the middle Eocene Avon Park Formation.

The next geological unit of interest is the Hawthorn Formation, which consists of Miocene aged sediments. This formation is the most lithologically complex stratigraphic unit in Florida and varies considerably from southwest to southeast Florida. The formation does have a few common characteristics throughout south Florida. First, the lower section of the formation contains a mixture of predominantly carbonate sediments with some clastic units. Second, the percentage of clastic sediments increases going up section. Third, the top of the formation is dominated by dolosilts and quartz sands. Fourth, nearly all Hawthorn sediments contain phosphatic sediments.

2. Hydrology of the Floridan Aquifer System

The hydrological area of interest of this work is in the Western Hillsboro site, which is located approximate 25 miles west of the Atlantic Ocean and approximately 15 miles west of the western boundary of the City of Boca Raton in unincorporated Palm Beach County ,Florida. In this area an exploratory well was constructed to provide hydrological information on the Floridan aquifer system. The results of the well log analysis and the petrophysics of this exploratory well is given by Bennett et al. (2001). Based on this report, the Upper Floridan aquifer in the western Hillsboro Basin consists of thin, high permeable water bearing horizons interspersed within thick, low permeable units of Oligocene to middle-Eocene aged sediments. These units include the Suwannee Limestone, Ocala Limestone, and Avon Park Formation. At this site the top of the Floridan aquifer system occurs a depth of 985 feet bpl. The lithology from this depth to 1010 feet (bpl) is composed primarily of moderately indurated wackestones and packestones containing approximately 15-50% shell fragments and 10-15% quartz and phosphatic sands and silts. The sonic, induction and caliper logs all indicate a competent, low porosity unit at a depth of 1010 that continues to 1025 feet bpl. The caliper log indicates a relatively gauge borehole (i.e., similar to the diameter of the drill bit) which corresponds to well-indurated yellowish-gray packestone unit.

Sediments from 1025 to 1070 feet bpl consist of yellowish gray, moderately indurated wackestones interspersed with thin fine-grained calcitic sandstones. A change in lithology occurs at 1070 feet bpl from a yellowish-gray, phosphatic wackestone to light-gray, clean, moderately indurated wackestone-packestone. These changes at 1070 feet bpl may represent a flow zone that occurs near the top of the Early Eocene ages, Ocala Limestone.

The light-gray moderately indurated wackestones and packestones continue from 1070 feet to 1170 feet bpl, a zone of minor water production. A light orange to yellowish gray, moderately to well indurated packestone unit is encountered from 1170 to 1205 feet bpl. The fluid-type logs (e.g., flow, temperature logs) indicate good production from flow zones between 1050 and 1170 feet bpl and 1190 to 1205 feet bpl. Below 1210 feet bpl, the productive capacity is limited suggesting lower permeable units near the based of the storage horizon. The monitor well PBF 10 (located about 330 feet from the exploratory well) shows consistent lithologic and geophysical trends with depth which indicate lower permeable sediments. The lower permeable sediment at 1225 feet bpl marked the base of the production interval of the exploratory well

D. Pore and Core Scale Images

We analyzed carbonate rock samples at the pore and core scales by including image processing of OM thin section, SEM and CT data. The samples are from well PBF10, which intercepts the brackish water aquifer of the upper Floridan aquifer. This site includes the lower Arcadia Form (Hawthorn Group), Ocala limestone and upper Avon Park Formation.. CT images from cores #7 and #41 were processed and analyzed to measure the vug size distributions and then compared with core photographs. The images were also modeled to simulate ultrasonic waveforms, to analyze the effects of saturated and unsaturated vuggy core samples on compressional wave velocity. The optimal application is to devise methods to characterize vugs at the core and borehole scales based on acoustic and ultrasonic measurements.

The types of minerals and porosities was provided by petrographic analysis of the thin sections. Analysis of the SEM and OM images provided information on the pore size distribution of the rock matrix, which was used to calculate synthetic T_2 distributions to evaluate the NMR well log signatures. Since the SEM/OM images gave a good indication of whether the micro- and macro-pores were connected, a more accurate T_2 cut-off could be determined to calibrate the NMR well logs.

In general, the image analysis helped us characterize the pore structure of the carbonate rock. The goal is to determine whether permeability is controlled by the matrix and/or vuggy porosity. The integration of CT, OM, and SEM images with petrography answers this question.

1. Processing of X-ray Computed Tomography (CT) Data

Cores #7 and #41 have extensive cavities that were captured by the tomographic images. The data contained in the tomographic images is called CT number, and it refers to the amount of X-ray scattering and absorption occurring at a particular point. The CT number is approximately proportional to the density, at least for more-or-less single mineral materials. Some preprocessing was applied to the CT data to extract the core from the surrounding media and to correct for beam hardening. Beam hardening refers to the fact that X-rays of some energies are more easily scattered than others, and these tend to leave the X-ray beam first. Therefore the X-ray beam that penetrates to the core center is more resistant to scattering than that

which first encounters the core edge, and the core falsely appears to be less dense in the center than around the edges. Corrections for this were made in the data acquisition lab, and we clipped a few extra pixels from the core edges to ensure that all non-core material was removed from the data.

Our first goal in processing the CT data was to convert the CT number into density. Many assumptions go into this conversion, so we cannot claim that the resulting core model is an exact representation of the true core. We can say, however, that the core model is based on the structure measured from the true core, and perhaps this is sufficient for our purposes. The density conversion was accomplished by looking at the average, peak, and minimum CT numbers. We also noticed a bias toward weaker CT number with increasing depth in core #41, and we corrected for this bias by using slice-by-slice averages and cutoffs. In each slice, then, the highest density material should be non-porous calcium carbonate grains, which have a density of around 2.7 g/cc. The lowest density material should be the cavities in the core, which have a density close to zero. Unfortunately, while the cavities are readily apparent in the CT data (see Figure 2), there is no strong low-end cut-off. The CT numbers gradually shade from cavity into hard rock.

In the face of this uncertainty, we used an empirical method to fix the conversion process. Accordingly, we set the high-end cut-off so that 99% of the data has a smaller CT number, and we assigned this value a density of 2.7 g/cc. We further assumed the maximum localized matrix porosity in the core is 35%, and that anything appearing to be less dense is really a cavity. We then chose the slope of the conversion curve so that the average density of the model core is equal to the physically measured average density of the real core.

The success of this technique may be observed in the following three images. Figure 2 shows a slice of the raw CT data (core #41, top slice). Figure 3 shows the computed density for the same slice, using the previously described conversion method. Figure 4 shows a photograph of the end of the core, approximately 2 mm removed from the slices of Figures 2 and 4. Comparing the photograph and the computed density slice, there is a good correlation between real and predicted cavities and their boundaries. The computed profile appears to slightly overpredict the sizes of the cavities, but it also misses several smaller cavities seen in the photograph. We assert, then, that while we may not have a model which perfectly reflects the physical core, it should be sufficient for most purposes.

a. Extracting stochastic quantities

After the core data has been converted to density, it may be processed for several other quantities of interest. The portion of the core porosity which is vuggy porosity (observable cavities) is directly obtained from the processed density image. The matrix porosity is also directly obtainable, since we have assumed a grain density of 2.7 g/cc. Thus, any bulk porosity less than 2.7 g/cc is due to matrix porosity at that location. The saturated bulk density of the core may then be predicted by fluid substitution using the known porosities. Table 1 expresses some of these properties.

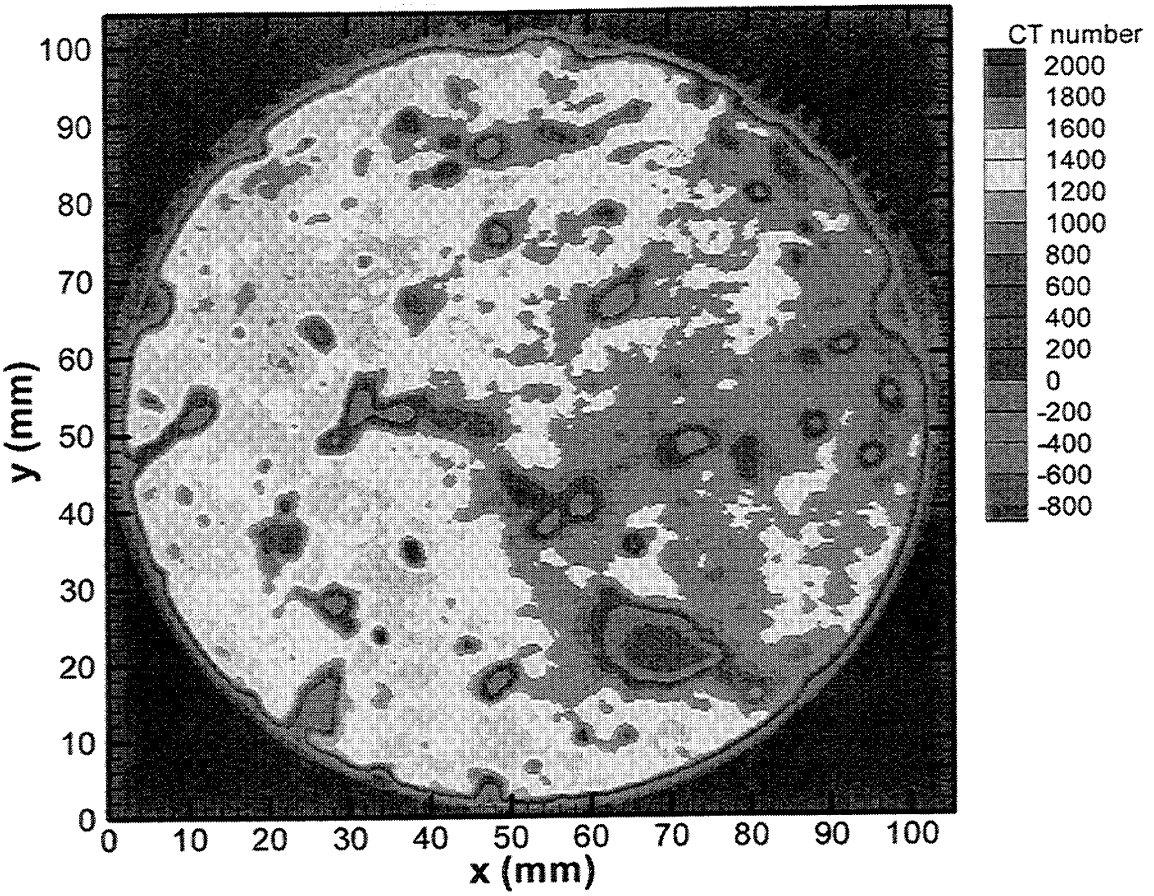

Figure 2: A slice of the raw CT data from core #41. Data plotted is CT number.

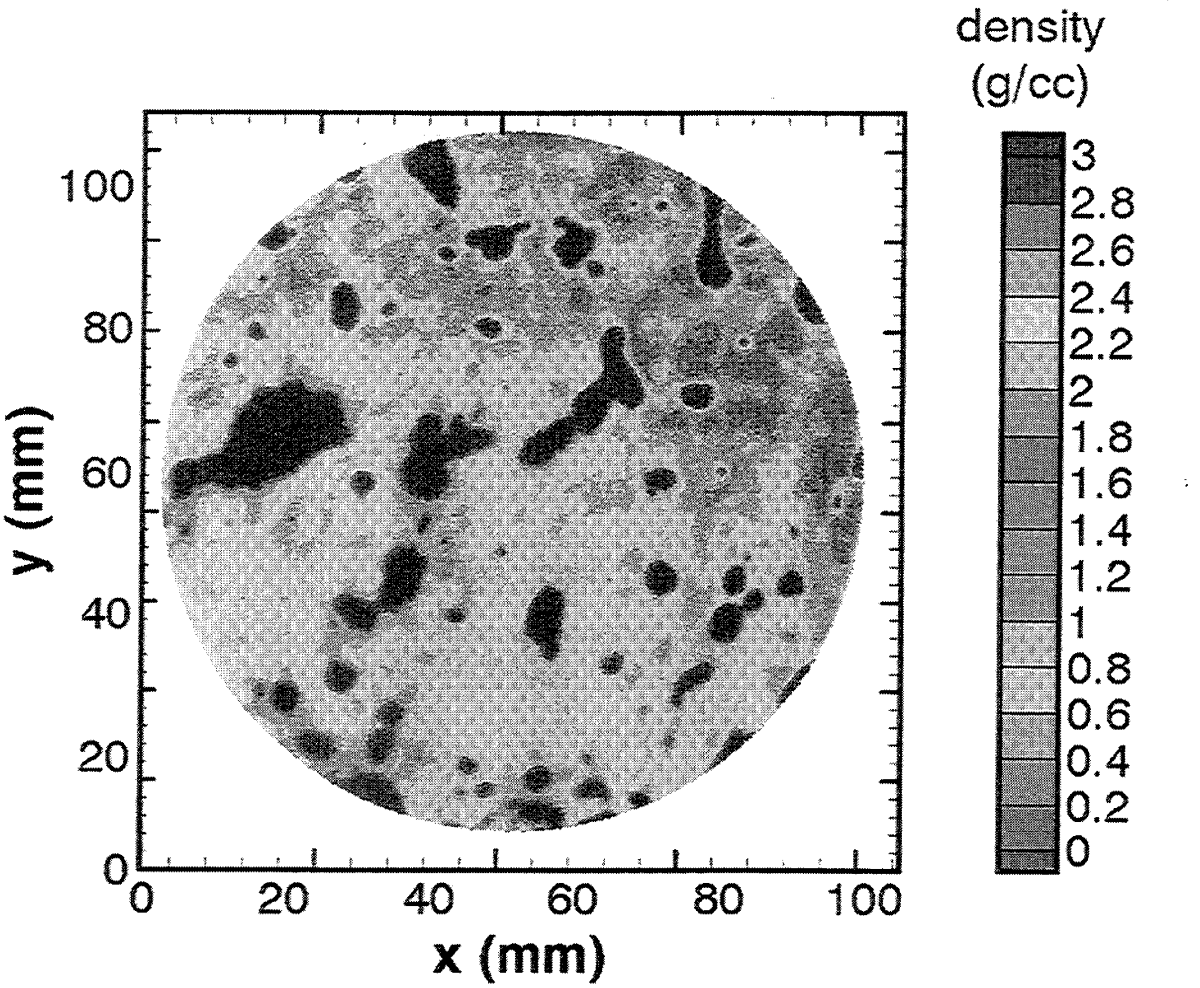

Figure 3. Calculated density from the X-ray CT data for a slice from core #41. Data plotted is dry density in g/cc.

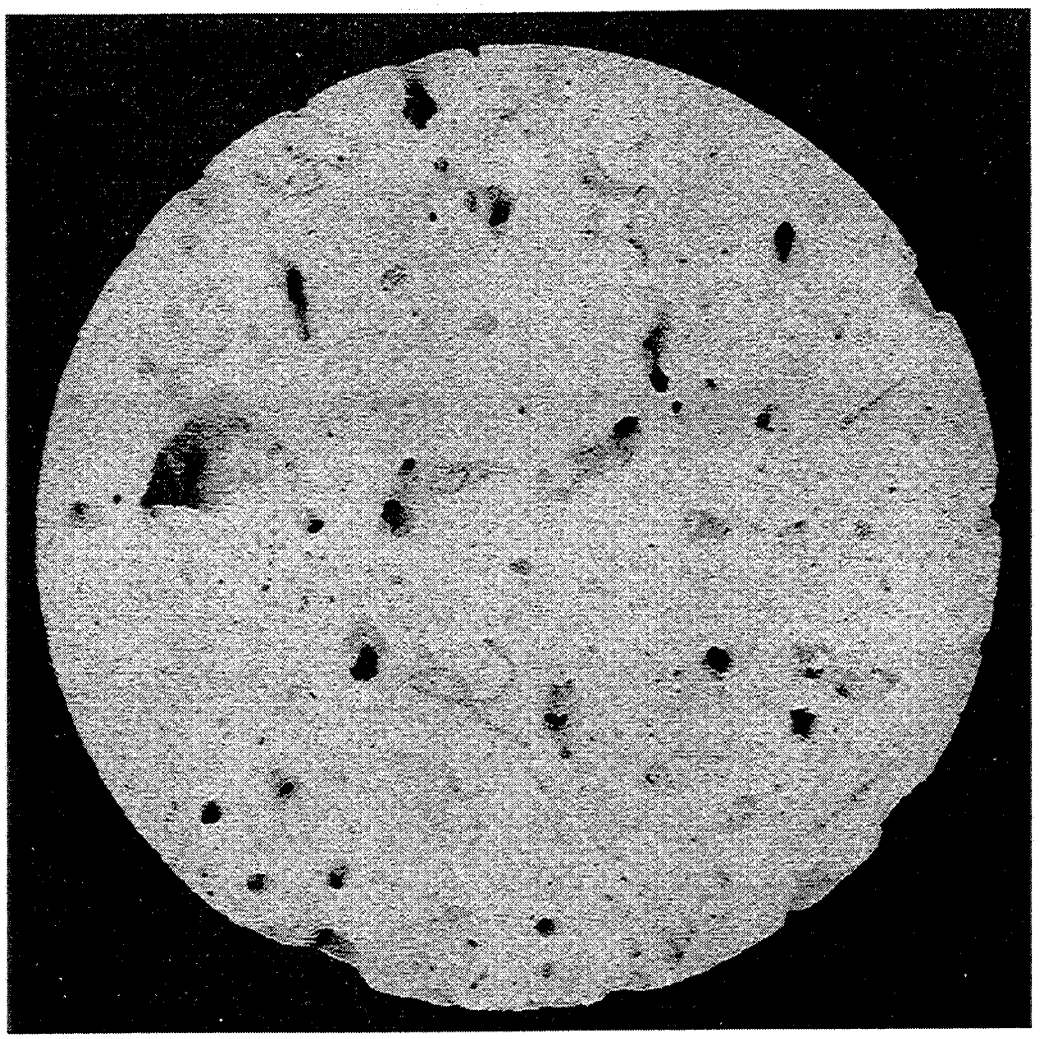

Figure 4: Photograph of an end of core #41, parallel to and approximately 2 mm removed from the X-ray CT slice of Figures 2 and 3.

Table 1: Computed and observed core properties.

property	Core #7	Core #41
computed vuggy porosity	4.5%	13.4%
computed matrix porosity	11.6%	20.9%
computed total porosity	15.6%	31.5%
observed dry density	2.20 g/cc	1.85 g/cc
computed dry density standard deviation	2.28 g/cc 0.53 g/cc	1.87 g/cc 0.76 g/cc
observed saturated density	2.42 g/cc	2.17 g/cc
computed saturated density standard deviation	2.44 g/cc 0.34 g/cc	2.18 g/cc 0.48 g/cc

Here, the matrix porosity is the porosity of the non-cavity matrix. Thus, the total porosity is

$$\phi_{total} = \phi_{vuggy} + \left(1 - \phi_{vuggy}\right)\phi_{micro} \quad . \quad (1)$$

Looking at the standard deviations, it is apparent that there is a great deal of variability within the core. This is true even when comparing two horizontal slices within the same core, as seen in Figures 5 and 6.

b. Length scales

The length scales associated with the random variability in the cores can be quantified by computing the 3D autocorrelation function. The autocorrelation, expressed as a function of separation ("lag") between two points, provides a measure of how closely related one might expect those two points to be. If the autocorrelation is one, then the two points have identical properties. If the autocorrelation is zero, then the properties at the two points are statistically independent, and their relationship is random. In Figure 7, we show a plot of the 3D autocorrelation function for core #41. It is apparent that the autocorrelation is fairly independent of azimuth, but that the z-direction does behave differently than the x-y plane. For small lags, the autocorrelation function is nearly isotropic. At larger lags, the autocorrelation is much higher along the z-axis than the x- and y-axes.

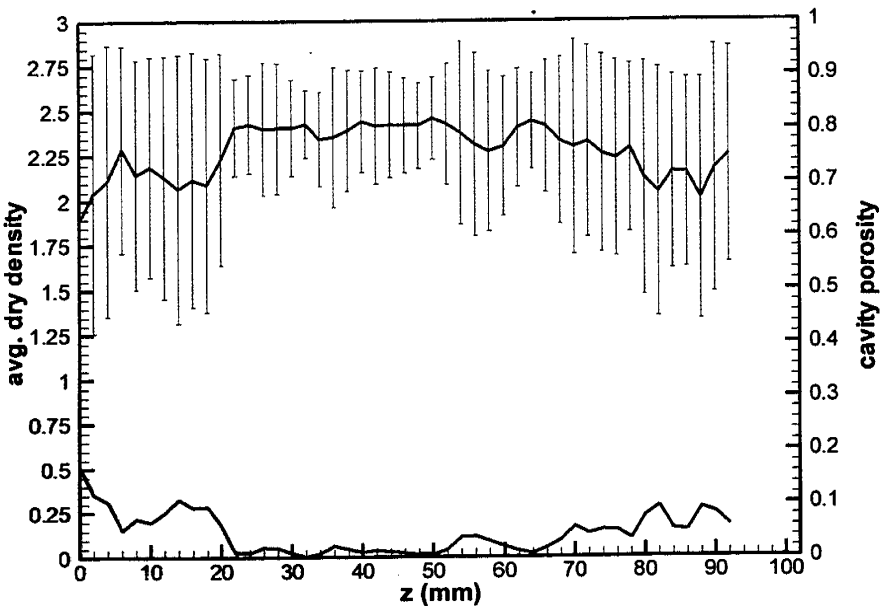

Figure 5: Core #7 slice-by-slice properties. Green curve is dry density (with standard deviation), and red curve is cavity porosity.

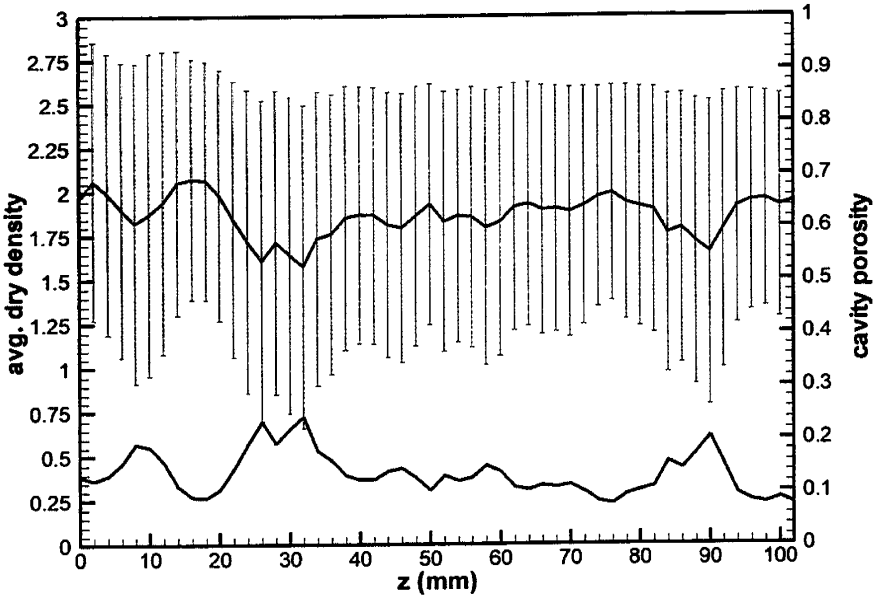

Figure 6: Core #41 slice-by-slice properties. Green curve is dry density (with standard deviation), and red curve is cavity porosity.

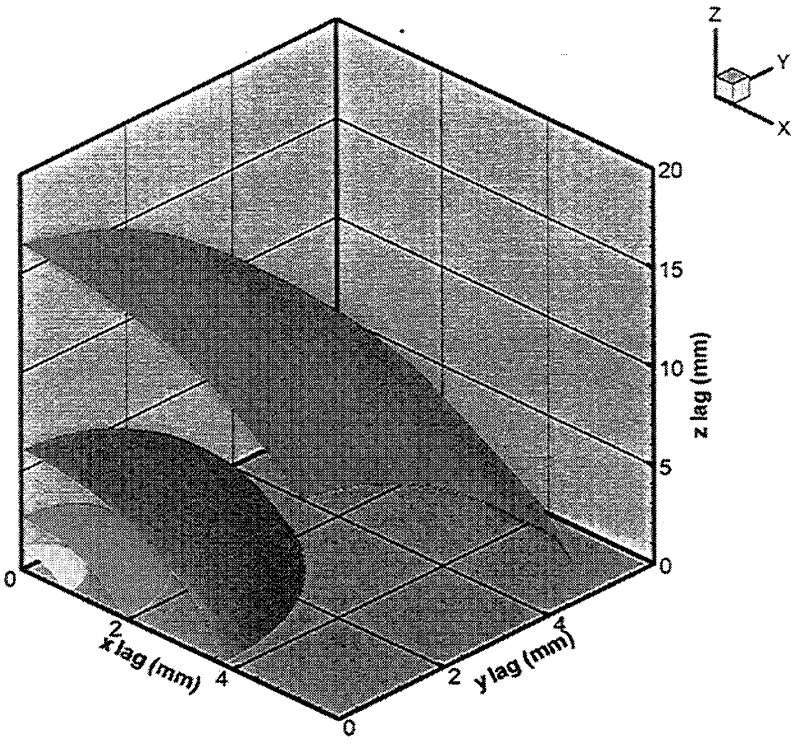

Figure 7: Three dimensional autocorrelation function of core #41. Isosurfaces are at autocorrelations of 0.8, 0.6, 0.4, and 0.2, with the maximum value of 1 at (0,0,0). Note the vertical exaggeration.

We can quantify the length scales involved in the autocorrelation function by fitting functions along the various axes. As a function of the lag, a, we will fit the autocorrelation with the following function chi:

$$\chi(a) = w\exp\left(-a/L_1\right) + (1-w)\exp\left(-a/L_2\right) \qquad (2)$$

where w is a weight, $0 < w < 1$. We chose a double exponential representation because in many cases there is more than one operative length scale in random fields.

We applied this function to the autocorrelation along each of the three principal axes in cores #7 and #41. In both cores we found that, as expected, the x and y profiles are essentially identical. Therefore, we used the same scales and weights to fit both the x and y profiles. In core #7, the autocorrelation was fit adequately by a single exponential function, so w was set to one, and only one length scale was used along each axis. The profiles and fits are shown in Figures 8 and 9. Table 2 gives the actual weights and scales extracted. These length scales and weights are independent of whether the cores are dry or fully saturated because they only depend on the spatial distribution of porosity.

Table 2: Length scales of random variability in cores.

core	weight	$L_{1,xy}$	$L_{2,xy}$	$L_{1,z}$	$L_{2,z}$
#7	1	3.0 mm	-	2.0 mm	-
#41	0.5	2.4 mm	7.2 mm	2.2 mm	17.0 mm

c. Scattering Attenuation

Having established the degree of randomness in the standard deviation of the core density and the length scale of the random variations, we were able to apply the 3D stochastic medium theory to predict the degree of scattering attenuation experienced by high-frequency waves. The results for both cores are shown in Figure 10.

2. Thin Section and SEM Photomicrographs

We conducted thin section petrography and SEM of two carbonate samples (1021.7 and 1138.4 feet) from the PBF10 well. The objectives were to: (1) provide petrographic descriptions of rock texture, fabric and mineralogy; and (2) describe the pore system properties.

Both samples were carbonates, although their textures were quite different. The sample from 1021.7 feet (Sample # 7) is a grainstone (see Figures 11a-e), while the sample from 1138.4 feet (Sample # 41) is a wackestone (see Figure12a-e).

The skeletal grainstone exhibits the greatest diversity of carbonate allochems, including echinoderms, miliolid and rotalid forams, worm tubes, pelecypods, peloids, intraclasts, various algal grains, gastropods, bryozoans, and ostracodes. Upper very fine to lower fine-grained quartz and feldspar sand is distributed throughout the sample in moderate amounts. The skeletal assemblage, grain size, and limited carbonate mud are indicative of high energy sedimentation in a normal marine environment. In contrast, the wackestone sample contains a less diverse assemblage of framework grains, which includes forams, ostracodes, peloids, intraclasts, algal grains and corals. Also in contrast to the grainstone sample is the abundance of carbonate mud. This wackestone is low energy, normal marine sedimentation.

The pore system of the skeletal grainstone comprise moldic, vuggy, intergranular, interparticle and inercrystalline pores, and visible porosity is approximately 17% by point count. Macropores associated with micritic grains such as peloids and intraclasts are present in minor amounts; however, they do not contribute to the effective pore volume. Syntaxial overgrowths and fringing and equant calcite cements are the most abundant pore-filling constituents in this sample; dead oil is locally present.

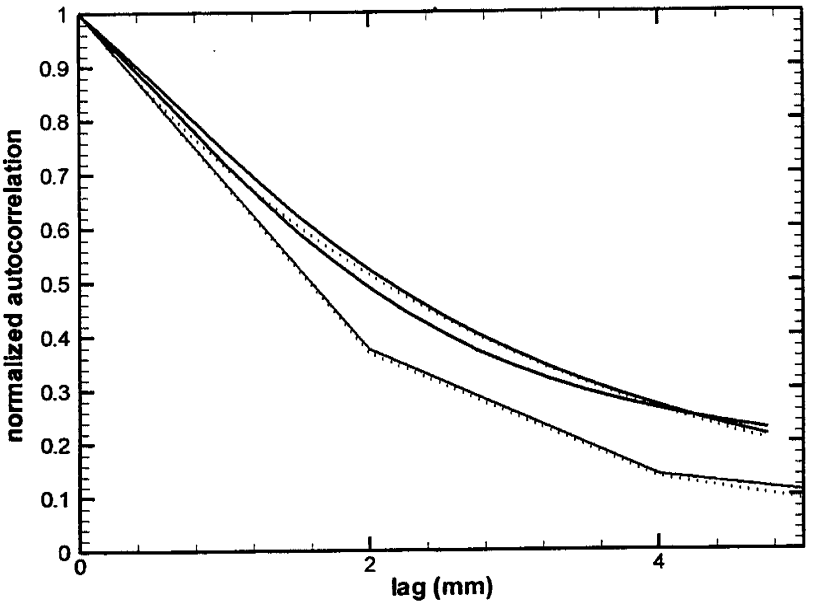

Figure 8: Red, green, and blue curves are the autocorrelation profiles along the x, y, and z axes respectively in core #7. The dotted lines are the best fits.

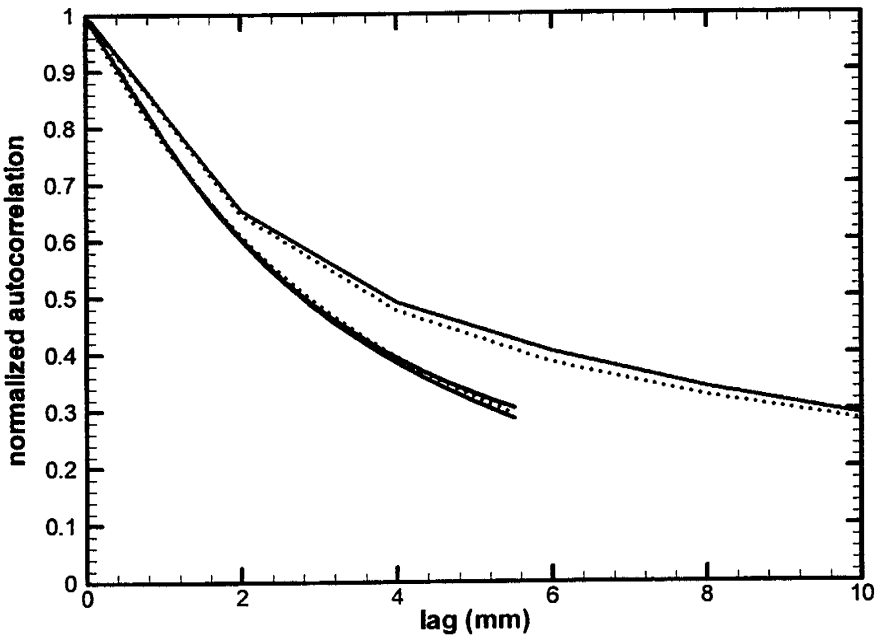

Figure 9: Red, green, and blue curves are the autocorrelation profiles along the x, y, and z axes respectively in core #41. The dotted lines are the best fits.

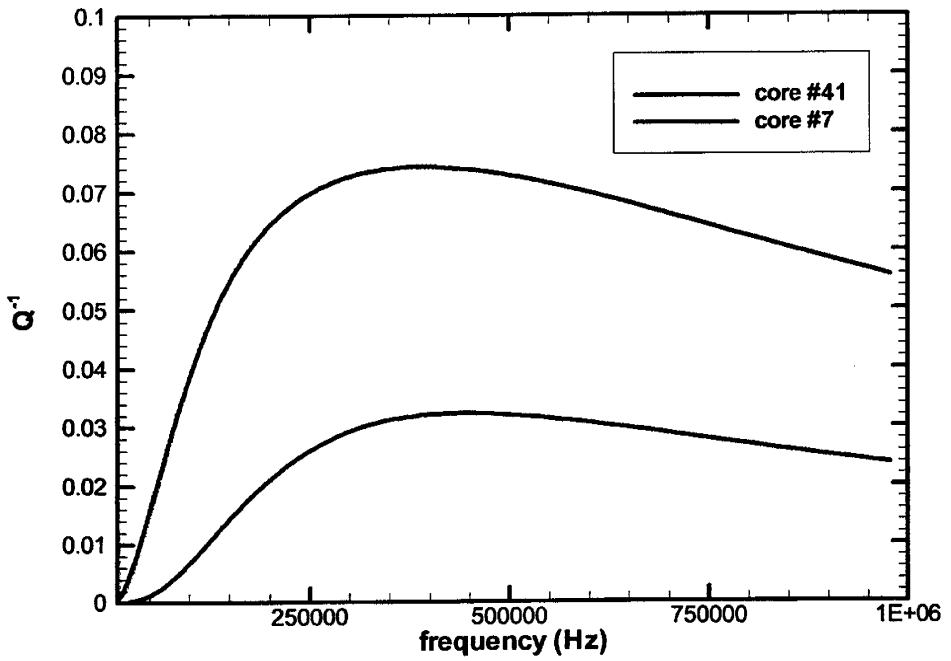

Figure 10: Predicted Q values from each core due to scattering from the random variability in structure (saturated conditions).

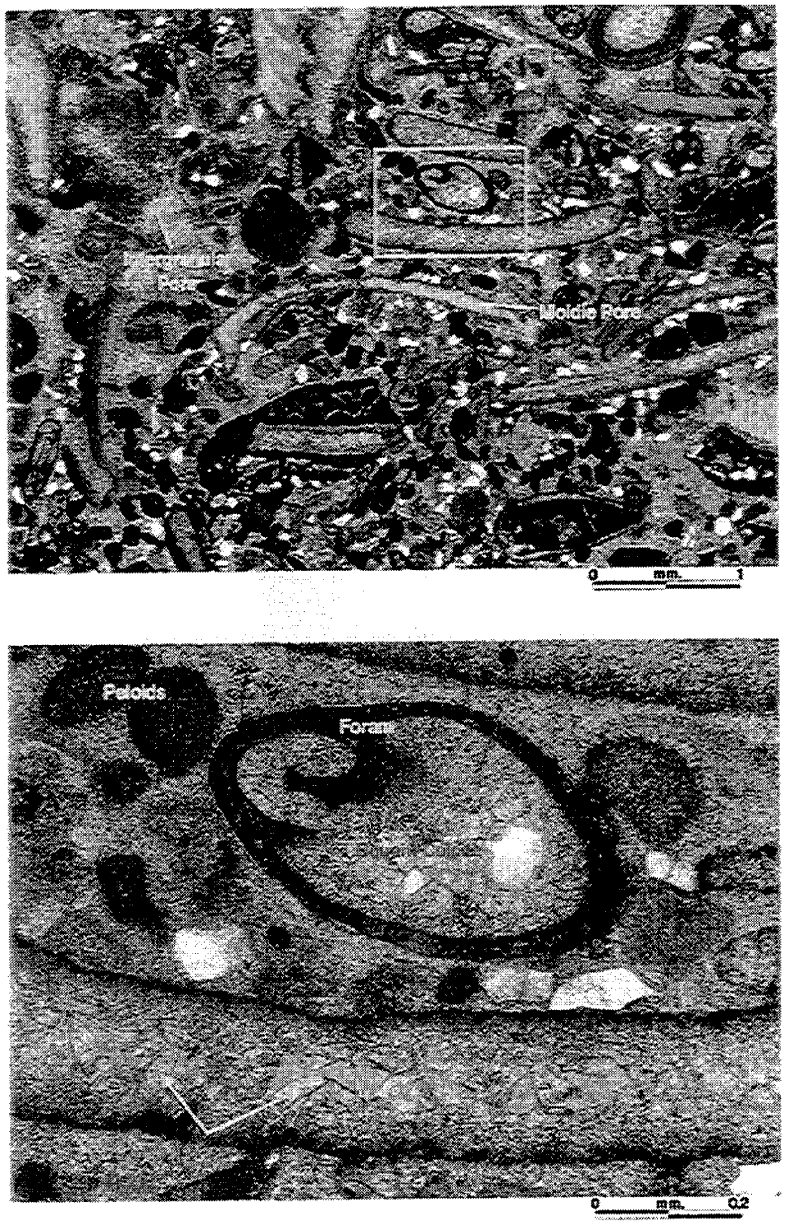

Por 200

Figure 11a-b. OM 20X and 100X magnifications showing peloids, foraminifera, and equant calcite

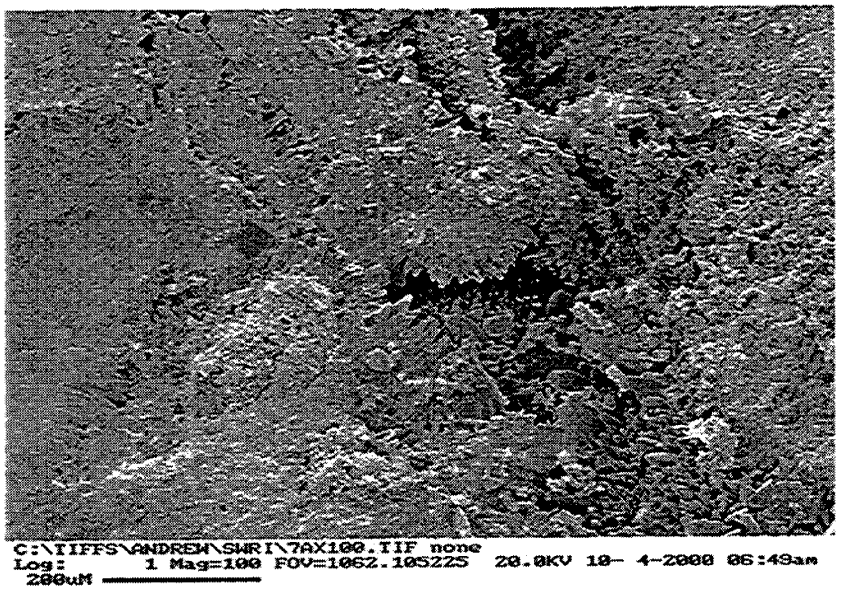

(c)

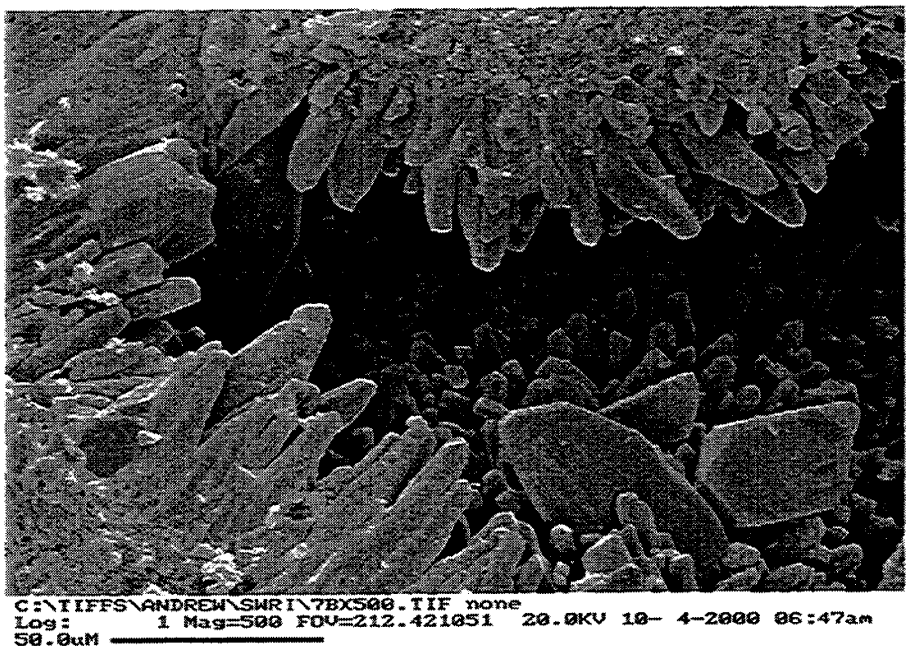

(d)

Figure11c-d. SEM 100X and 500X magnifications showing intergranular pores and calcite spar.

(e)

Figure 11e. Sample of Core #7 approximately 5 centimeters long, showing separated and connected vugs.

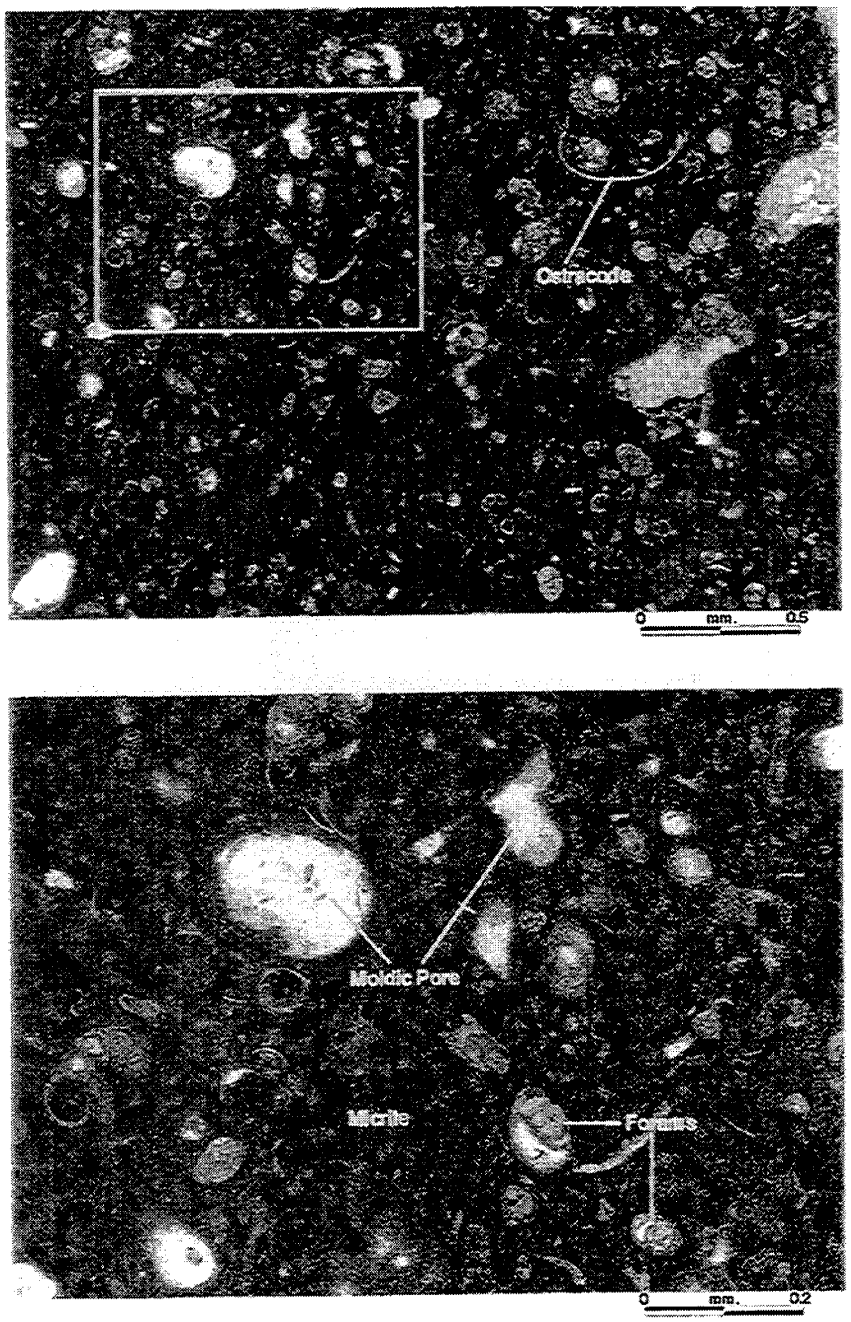

Figure 12a-b. OM 40X and 100X magnifications showing moldic pores, micrite, and foraminifera.

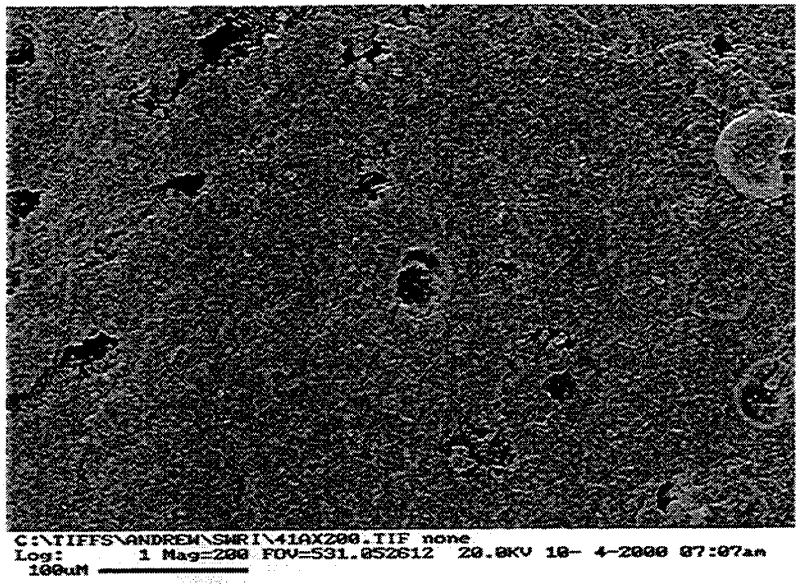

(c)

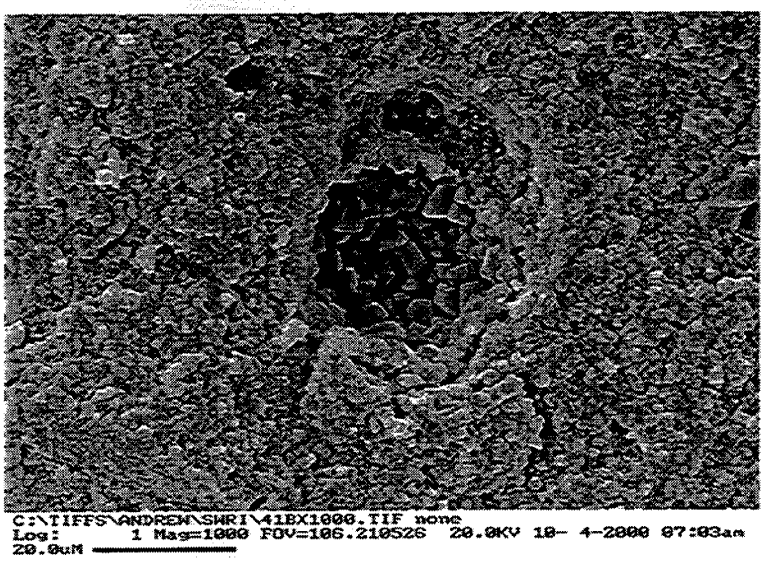

(d)

Figure 12c-d. SEM 200X and 1000X magnifications showing microporosity.

(e)

Figure 12e. Sample of core #41, approximately 5.7 centimeters long, showing vugs.

Very little primary porosity is present in the wackestone sample. Moldic and vuggy pores dominate the assemblage of visible pores, with fewer intercrystalline and intraparticle pores. Total visible porosity was determined to be approximately 8% by point count. Micropores are common in the micritic matrix and contribute significantly to the total porosity of the sample. However, despite their large contribution to the total pore volume, these micropores do not contribute to the effective pore volume or permeability of this sample.

a. Thin sections and SEM photomicrographs for Core #7

This core is a slightly sandy limestone with a grainstone texture. The pore system of this skeletal grainstone is rather well-developed and comprises moldic, vuggy, intergranular, intraparticle and intercrystalline pores. Micropores are present in minor amounts and are typically associated with micritic framework grains. The macropores have been partially to completely filled by a combination of syntaxial overgrowths, bladed fringing calcite cement, and equant calcite cement. The diverse assemblage of allochems includes echinoderms, foraminifera, annelid tubes, pelecypods, peloids, intraclasts, various algal grains, gastropods, bryozoans, and

ostracodes. Many of these grains exhibit endolithic algal coatings. Upper very fine to lower fine-grained quartz sand is distributed throughout the sample in moderate amounts.

b. Thin sections and SEM photomicrographs for Core #41

This core is a limestone with a wackestone texture. The pore system of this skeletal wackestone is dominated by moldic and vuggy pores; intercrystalline and intraparticle pores are uncommon. However, due to their isolated nature, these pores contribute little to the effective porosity and permeability of this sample. Micropores are rather common within the micritic matrix of this limestone; however, despite their contribution to the total pore volume, they do not contribute to the effective porosity or permeability. The framework grain assemblage is dominated by forams; other allochems include ostracodes, peloids, intraclasts, algal grains and scleractinian corals. Sand-filled burrows were also noted.

3. Core Imaging and Relation to NMR T_2 Distribution

NMR T_2 distributions are commonly associated with pore size. This is the basis of NMR logging for permeability, as larger pores are assumed to be indicative of higher permeability formations. We examine core images on several scales (X-ray CT, OM, SEM) to identify pore size and shape distributions and relate these to NMR T_2 distributions.

We begin with three different core images using three different techniques, spanning a range of length scales. The first method, X-ray computed tomography (CT), produces three-dimensional images of whole cores with a pixel resolution of about 0.25 mm. This is primarily useful for imaging vugs. The second technique is optical microscopy (OM) of thin sections, which provides a pixel resolution on the order of 2 μm. This is useful for imaging moldic and interparticle porosity. The third technique is scanning electron microscopy (SEM) on polished core fragments, which we use to image microporosity with a pixel resolution of 30-300 nm.

To obtain the pore size and shape distribution from these images, we follow the method of Anselmetti et al. (1998) and use public domain software developed by NIH and Scion Corp., called Scion Image™. The first step is to convert the core images to TIF format grayscale files, where black represents pore space and white represents matrix. A macro written for the Scion Image program then cleans the image to eliminate single pixel noise, thresholds the image to divide pore from matrix, counts the pores, and determines the area, perimeter, and shape factor for each pore. These results may then be saved to a file.

A postprocessing program computes the pore radius and histograms of pore radius distribution. The pore radius is taken to be

$$r_{pore} = 2\left(\frac{area}{perimeter}\right), \tag{3}$$

$$\frac{1}{T_2} = \frac{2\rho}{r_{pore}} + \frac{1}{T_{2b}}, \tag{4}$$

where we assume that the ratio of volume to surface area is $r_{pore}/2$. The quantity ρ is the surface relaxivity, and it represents the tendency for molecules to relax their magnetization at the pore wall. Values usually range from 1 to 10 μm/s in carbonates (Chang et al., 1997; Ramakrishnan et al., 1999). The quantity T_{2b} is the bulk relaxivity, and it represents the time scale over which the magnetization is lost in a bulk (unbounded) fluid. In practice, workers almost always assume the bulk relaxation term is negligible compared to the surface relaxation term. However, in the Florida vuggy carbonates this assumption is unwarranted. Based on the data, it appears that the T_{2b} bulk relaxation time is about one second.

We can demonstrate the importance of the bulk term through simple analysis using equation (4). If the surface relaxivity rate is 5 μm/s, then a pore with radius 10 μm has a T_2 relaxation time of 1 second. This is a fairly small pore, but it is close to the bulk relaxation time. We know from examination of the core images that a significant fraction of the Florida carbonate porosity is in larger moldic and vuggy porosity, but this would not be apparent from the NMR logs. It can be argued that large pores do not contribute much to formation permeability, so it doesn't matter if the NMR log distinguishes them from smaller pores. An examination of the NMR log, however, might lead one to the erroneous conclusion that most of the porosity is in 10-20 μm pores. In consideration of this issue, Chang et al. (1997) recommended not using a T_2 larger than 750 ms when computing permeability in carbonates.

a. Results: Core #7

Core #7 is from a 1022-ft depth, in an interval which is transitioning between sandy limestones with few moldic pores and moldic, non-sandy limestones. Thin section images of Core #7 show isolated sand grains in the limestone matrix. As in Core #41, we used CT imaging with 0.25 mm resolution, OM with 40x magnification, and SEM with 300x and 3000x magnification. Some of the images used are shown in Figure 13. We extracted the pore size and shape distribution from these images, and the pore size histogram is shown in Figure 14. The comments made in the discussion of Core #41 regarding scales of view also apply here.

Table 4: Approximate breakdown of porosity by imaging method and porosity type.

CT (vuggy)	4%
OM (macro)	3%
SEM (micro)	12%
	---
total porosity from imaging	19%*
porosity from core	17%
porosity from NMR well log	24%
"Z" porosity from well log	17%

*Numbers do not add exactly because of overlap in SEM and OM length scales.

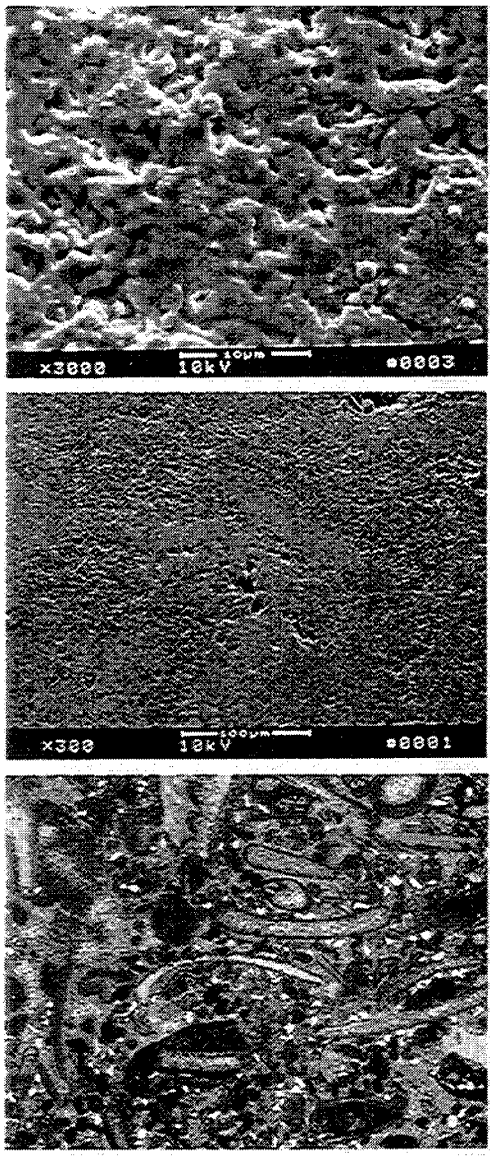

Figure 13. Images of core #7. (a) SEM 3000x magnification shows mostly microporosity. (b) SEM 300x magnification shows additional moldic porosity. (c) OM 20x magnification shows larger molds and intergranular porosity. White grains in image (c) are sand.

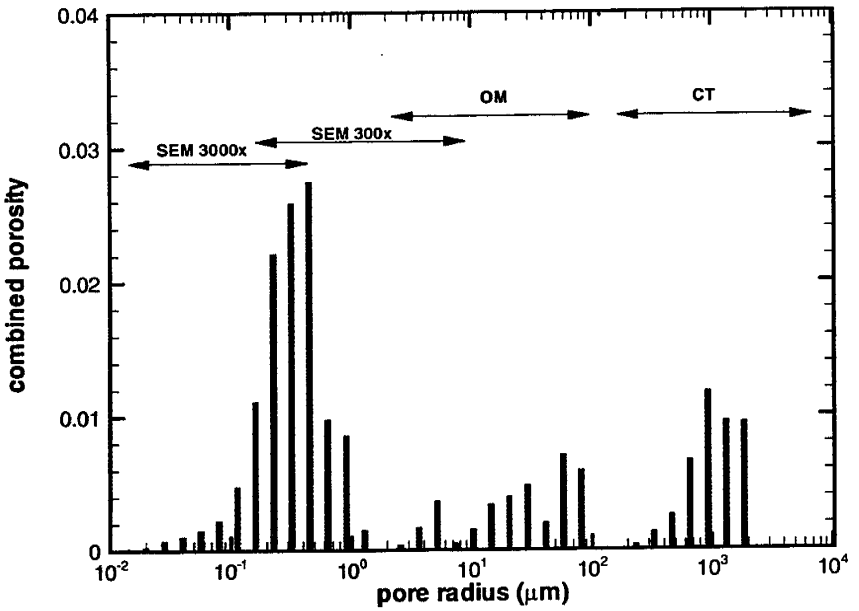

Figure 14. Pore size distribution for core #7 based on multiple imaging methods.

From pore size distribution, we can predict T_2 distribution. Matching the peaks of the pore size histogram and the well log T_2 distribution suggests that the formation relaxivity is near 5 μm/s, within the range of acceptable values for carbonates. The presence of sand is expected to increase the relaxivity somewhat (compared to core #41), as sandstones have higher relaxivities than carbonates. Figure 15 shows the predicted T_2 distribution from the core in the absence of any bulk relaxation using a relaxivity of 5 μm/s. In this case, the 32-ms peak from the well log reflects the matrix microporosity observed in the SEM images, and the bulk relaxation in larger pores accounts for the 0.5-second peak.

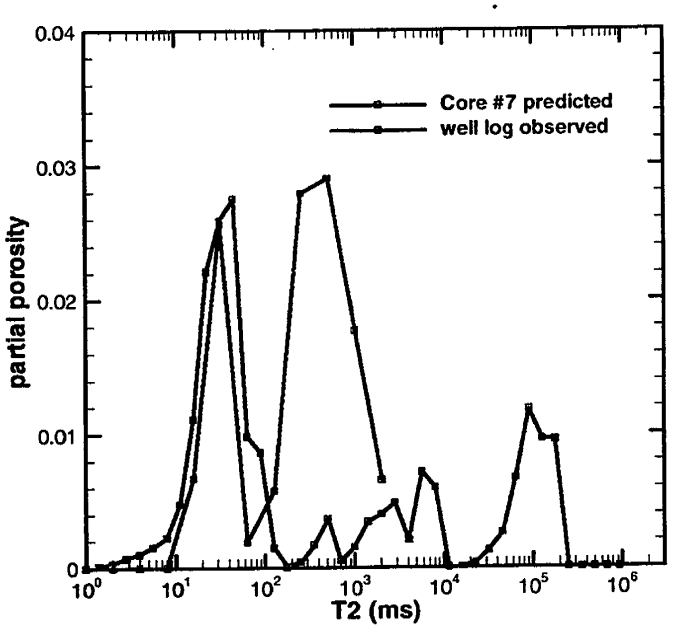

Figure 15. Predicted T2 distribution based on pore size histogram, compared to T2 distribution from well log. Only the porosity measured by the SEM imaging has a T2 decay time less than the bulk rate.

b. Results: Core #41

Core #41 is from an 1138 ft-depth, in an interval with a moldic and vuggy porosity. In examining this core, we used CT imaging with 0.25-mm resolution, OM with 40x magnification, and SEM with 300x and 3000x magnification. Some of the images used are shown in Figure 16. We extracted the pore size and shape distribution from these images, and the pore size histogram is shown in Figure 17. The two SEM magnifications and the OM image have overlapping scales of view, so there is a continuous distribution of pore sizes from 0.02 μm up to 50 μm. However, there is a gap in coverage between the largest pores observed by OM and the smallest pores observable by CT imaging. This is complicated by the fact that the smallest pores at each magnification are poorly resolved, while the largest pores are few in number. Thus, the accuracy of the pore size distribution falls off near the ends of the range of each technique. The overlapping coverage provided by the two SEM and OM magnifications is thus very valuable.

Table 3: Approximate breakdown of porosity by imaging method and porosity type

CT (vuggy)	13%
OM (macro)	4%
SEM (micro)	17%
	---
total porosity from imaging	33%*
porosity from core	32%
porosity from well log	39%

*Numbers do not add exactly because of overlap in SEM and OM length scales.

From the pore size distribution, we can predict the T_2 distribution. Matching the peaks of the pore size histogram and the well log T_2 distribution suggests that the formation relaxivity is near 1.5 μm/s. This is within the range of acceptable values for carbonates. Figure 18a shows the predicted T_2 distribution from the core in the absence of any bulk relaxation. Obviously, in this case about half of the porosity is distributed at T_2 decay times much longer that those recorded by the tool. By including the bulk relaxation time moves the large pores to a T_2 of about 800 ms, where it accounts for most of the deficit between the well log T_2 curve and the core T_2 curve between 200 and 1000 ms (Figure 15b). In an actual measurement, the spike at 500 ms would be diffused among neighboring times, because of both measurement uncertainties and the statistical nature of the process.

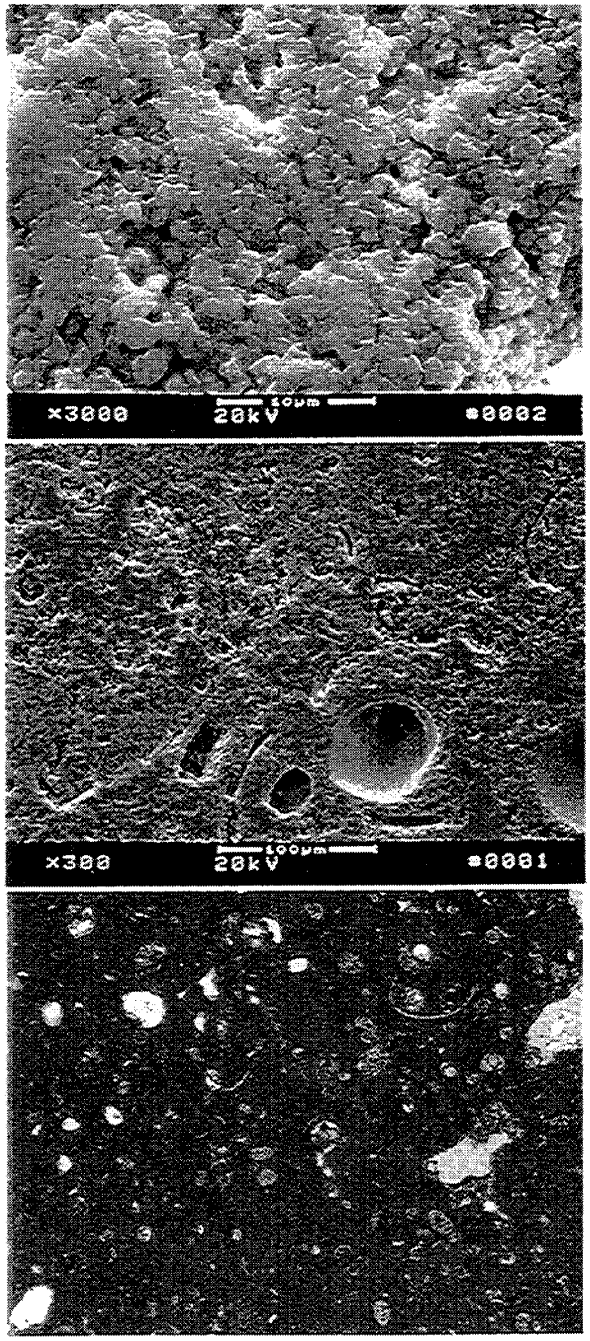

Figure 16. Images of core #41. (a) SEM 3000x magnification shows mostly microporosity. (b) SEM 300x magnification shows additional moldic porosity. (c) OM 40x magnification shows larger molds and intergranular porosity.

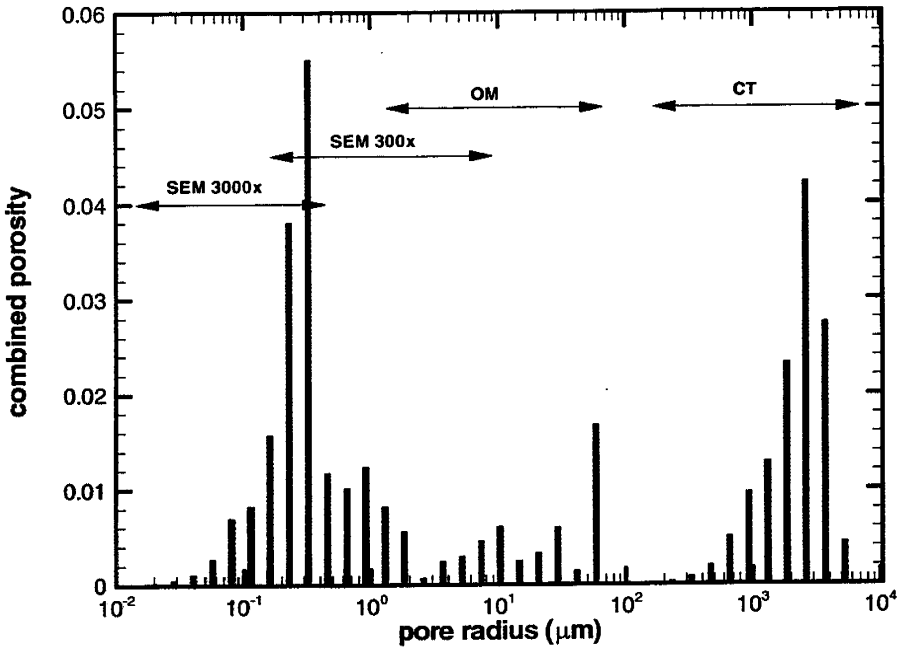

Figure 17. Pore size distribution for core #41 based on multiple imaging methods.

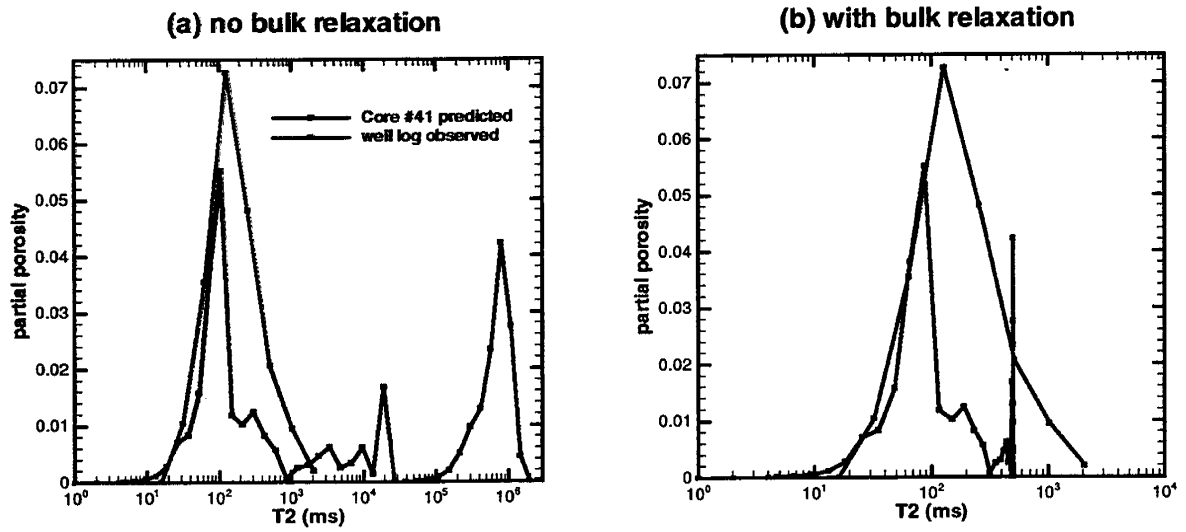

Figure 18. Predicted T_2 distribution based on pore size histogram, compared to T_2 distribution from well log. Only the porosity measured by the SEM imaging has a T_2 decay time less than the bulk rate.

E. Ultrasonic Wave Modeling and Velocity Analysis

1. Ultrasonic Waves in Vuggy Cores

We recorded waveforms for the P- and S-velocity measurements from 24 cores of the PBF10 well of the Florida aquifer. Most of the cores had only saturated measurements taken. In cores #7 and #41, both saturated and dry measurements were taken. The waveforms from these cores are shown in Figure 19. The early signal on each trace (at less than 10-20 microseconds) is an indirect signal from the transducer source. The late signal is believed to be ringing in the sample chamber. There is some reason to believe that the vuggy porosity may influence the waveforms. The wavelength of P-waves in the cores at the source frequency of 250 kHz is about 16 mm. This is approaching a typical cavity diameter, which might be in the range of 3-10 mm. In fact, many of the cavities are longer in the vertical direction than the horizontal direction, and many have lengths longer than 16 mm.

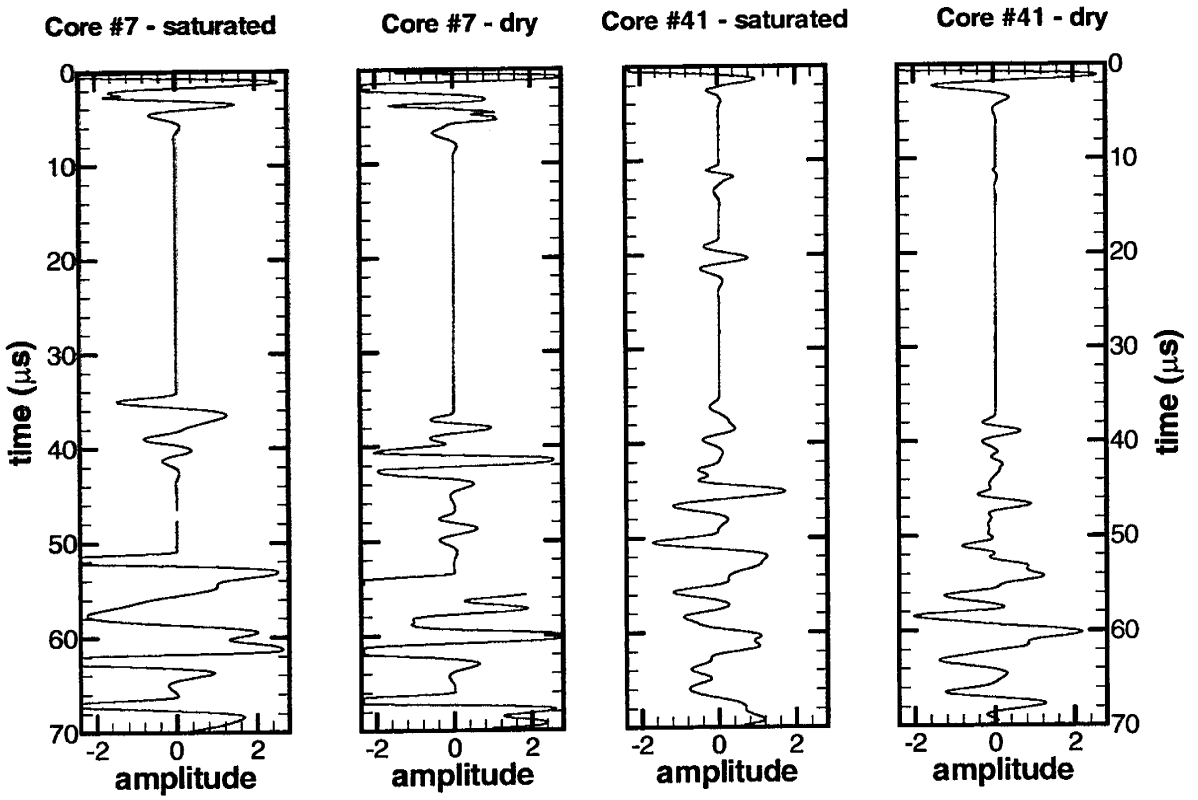

Figure19. Experimentally measured core P waveforms.

Working against us was the short core length. To be truly visible, wave dispersion should be such that the difference in time of arrival of different frequency components is a substantial fraction of a period. A wave period for these core measurements is about 4 microseconds. Since the P-wave travel time in these cores ranges from 13 to 43 microseconds, it requires a dispersion of 10-30% to be readily visible. Complicating matters, the transducer source is a resonant device, and it puts out a relatively narrow frequency band. For even a moderate quality factor (Q) of about 30, we can only expect approximately a 1% change in velocity due to dispersion over the frequency band of the source.

To observe any waveform signature it is best to look at the waveforms from the longest cores. Of the non-sandy cores (the sandy cores don't have cavities), #7 and #41 are the longest, with about a 25-microsecond P-wave traveltime. Since these are also the cores with both saturated and dry measurements and with X-ray CT measurements, these are the best to study. Time-frequency images of waveforms from these cores are in Figure 20. Much of the signal following the first arrival consists of multiple internal reflections and artifacts of the testing apparatus.

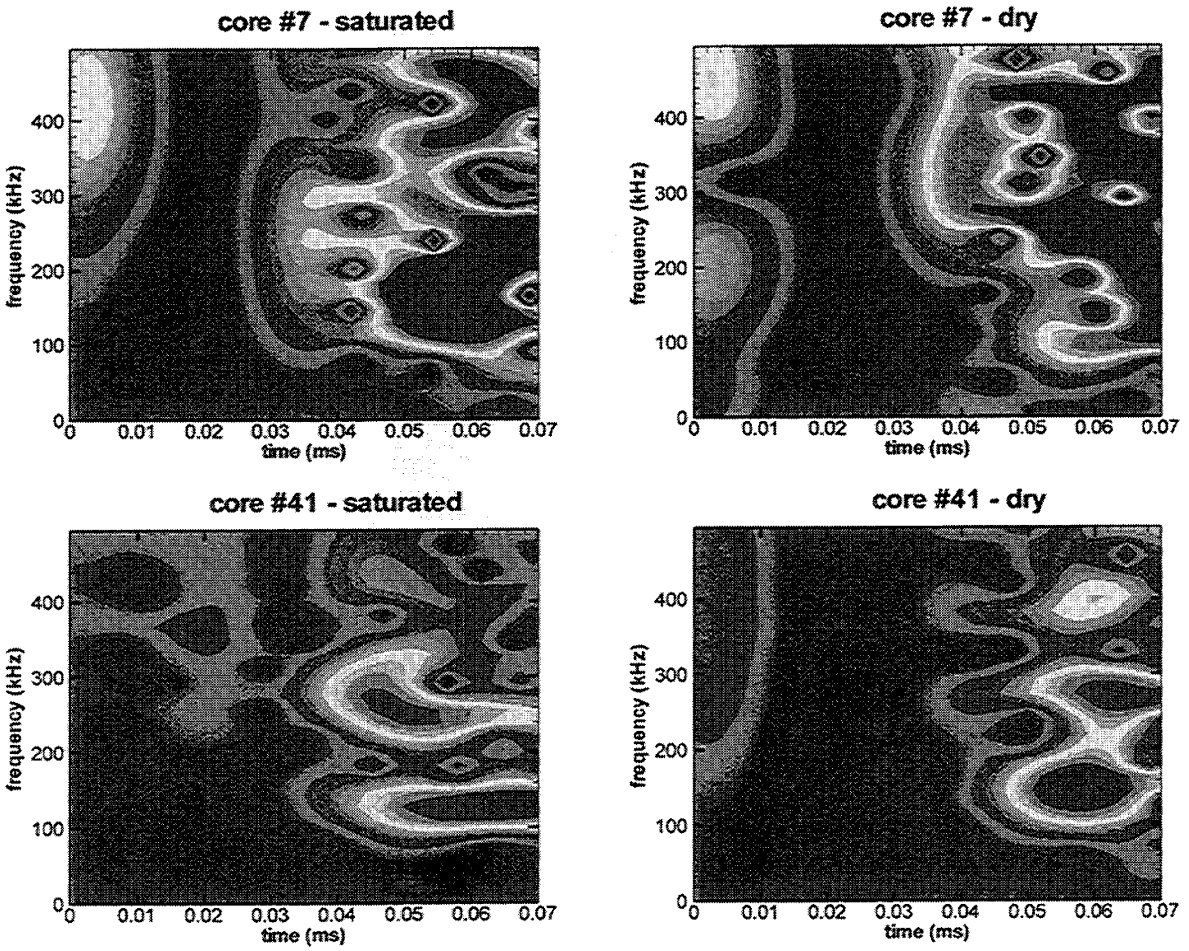

Figure 20. Time-frequency plot of observed core waveforms.

We can approximate the effects of the core and apparatus by performing a 2D finite-difference viscoelastic simulation of wave propagation. The detailed structure of the core is extracted from a vertical slice of the X-ray CT data (see Figure 3). This structure, with a horizontal resolution of 0.25 mm and a vertical resolution of 2 mm, is converted to density and assigned Vp and Vs values. The apparatus is simulated by steel piston end-caps for the core and a surrounding oil bath to maintain pressure, similar to the configuration described in Hokstad et al. (2000). A plot of this configuration is given in Figure 21.

Waveforms resulting from the finite-difference simulation are qualitatively similar to the experimental waveforms (Figure 22). We cannot expect them to be exactly the same because of differences in geometry (3D vs. 2D, and exact vs. approximate structure), source waveform, and experimental apparatus. Nevertheless, certain aspects of the synthetic waveforms are worthy of note. We ran three cases for each core. First, we produced a synthetic waveform using a uniform core, with constant density and constant elastic properties. The density of this uniform core is equal to the average density of (2.7 g/cc) the real saturated core. Second, we produced a synthetic waveform for the heterogeneous saturated core shown in Figure 21. Finally, we produced a synthetic waveform for a dry core. In this case, the cavities were filled with air rather than water, and the matrix had reduced density and elastic moduli associated with the removal of the fluid. These waveforms are of axial displacement measured in the lower endcap, and are the result of an axial signal originating in the upper endcap.

By using simulation, we can observe and quantify more directly some of the effects of the heterogeneities in the cores. In both cores, the amplitude is reduced as the transition is made from uniform water saturated to heterogeneous water saturated to heterogeneous dry core. This is indicative of the increase in scattering losses due to increasing core variability. Furthermore, we observe that in core #7, the arrival of the wave is almost simultaneous for the uniform and wet cases, while in core #41 the wet heterogeneous core has a wave arrival much earlier than the uniform case. This is a result of high velocity pathways in the heterogeneous core. Core #7 has few cavities and is much more uniform than core #41. This can also be seen in the waveform. The synthetic waveform for the heterogeneous core is almost identical to the waveform of the uniform, equivalent density core, although reduced in amplitude. In core #41, the waveforms for the two heterogeneous cases are noticeably different in shape when compared to the uniform core, and the dry and wet core waveforms are different from each other. In both cores, the substitution of air for water lowers the effective wave velocity, and delays the arrival of the wave.

We can compute the effective velocities for each media type since we know the model core length. The velocity of the homogeneous, uniform, water-saturated core is a fixed input to the model. Results are summarized in Table 5. The margin of error for the measured velocities is roughly 20 m/s.

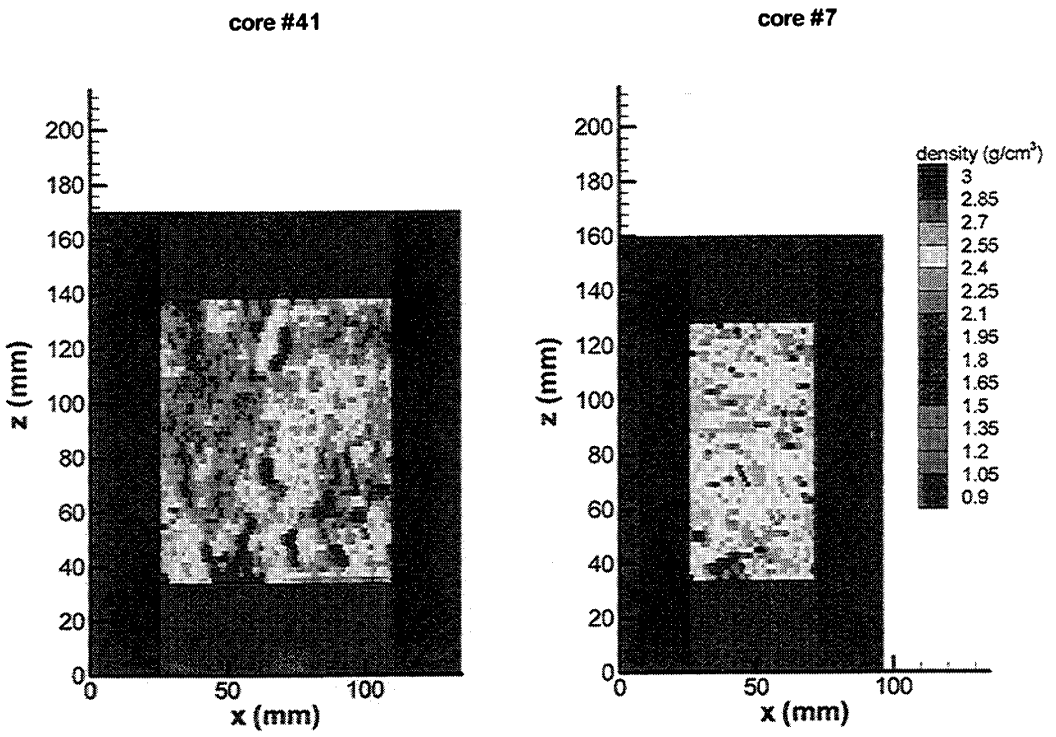

Figure 21. Density map of 2-D core for finite difference waveform calculation. Here, cores are assumed to be water saturated, capped by steel pistons, and surrounded by an oil bath.

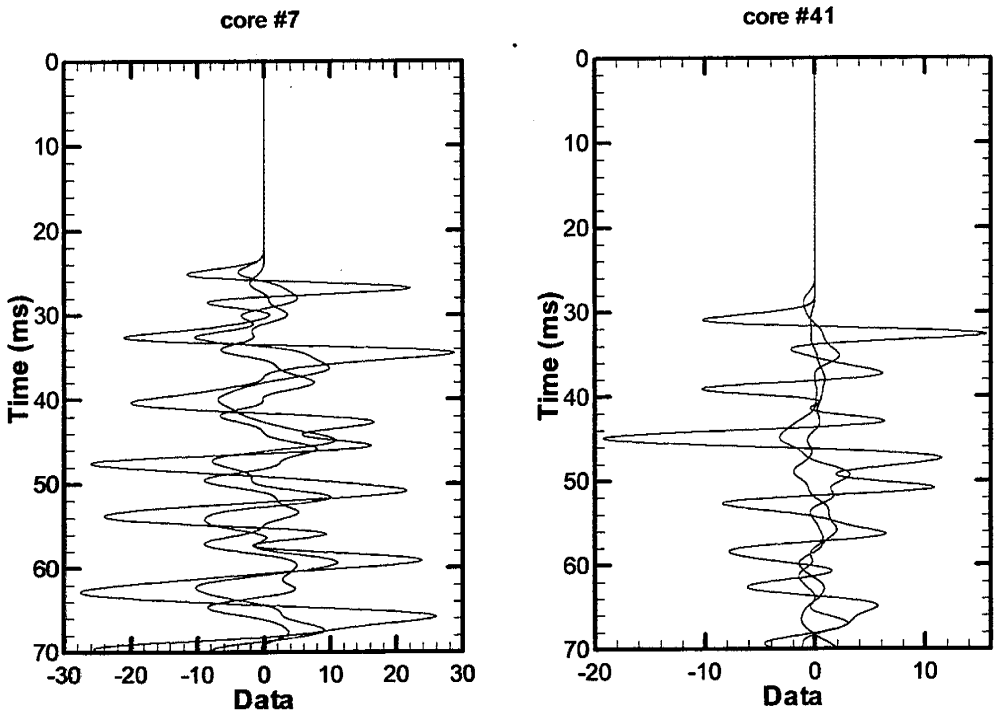

Figure 22. Synthetic waveforms from the 2-D core model. The black line is the waveform for a homogeneous saturated core, the green line is the waveform for the heterogeneous saturated core, and the red line is the waveform for the heterogeneous dry core.

Table 5. Velocities measured in synthetic cores.

Core Type	Core #7	Core #41
Uniform	4500 m/s	3900 m/s
Water sat., heterogeneous	4520 m/s	4360 m/s
Air sat., heterogeneous	4250 m/s	3970 m/s

The time-frequency representation of the synthetic waveforms also shows some interesting characteristics. In both core #7 (Figure 23) and core #41 (Figure 24), the uniform density core has a signal with a broad spectrum, consistent with the source center frequency of 250 kHz. The heterogeneous water saturated core attenuates the higher frequencies, especially in core #41. This is consistent with the predicted scattering attenuation due to the cavities. The dry heterogeneous cores show a slight increase in amplitude of early-arriving high frequencies. This is most likely also due to the cavities, as high-frequency, short-wavelength waves propagate through narrow, high velocity pathways around the cavities. The arrivals of the intermediate frequencies (200 - 300 kHz in core #7 and 100 - 200 kHz in core #41) are delayed in the dry core relative to the wet and uniform cores.

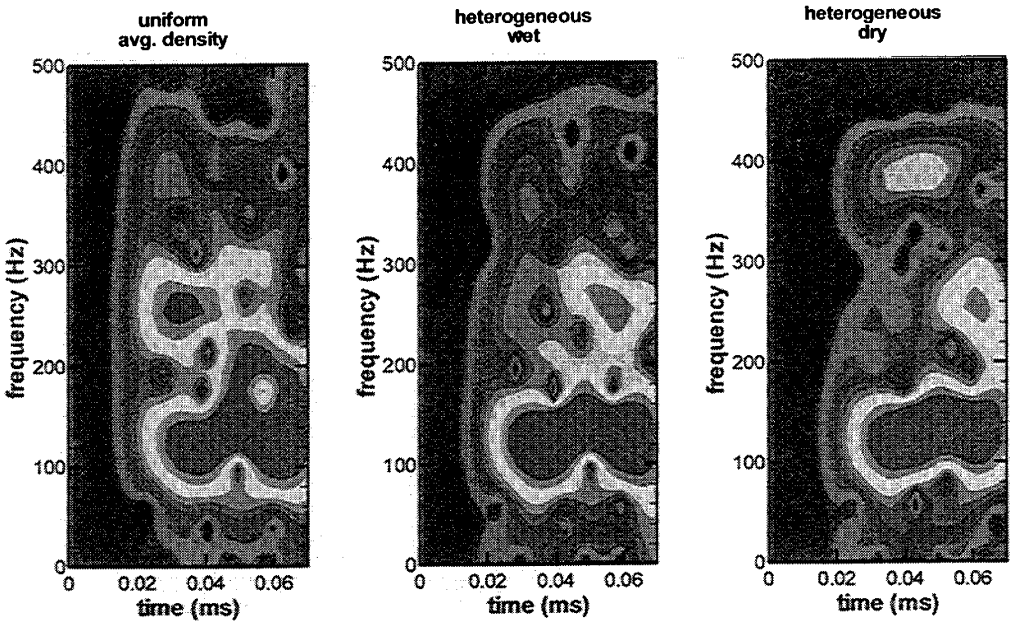

Figure 23. Time-frequency plots of core #7 synthetic waveforms. Amplitudes are in dB, and the color table spans 60 dB from blue to red.

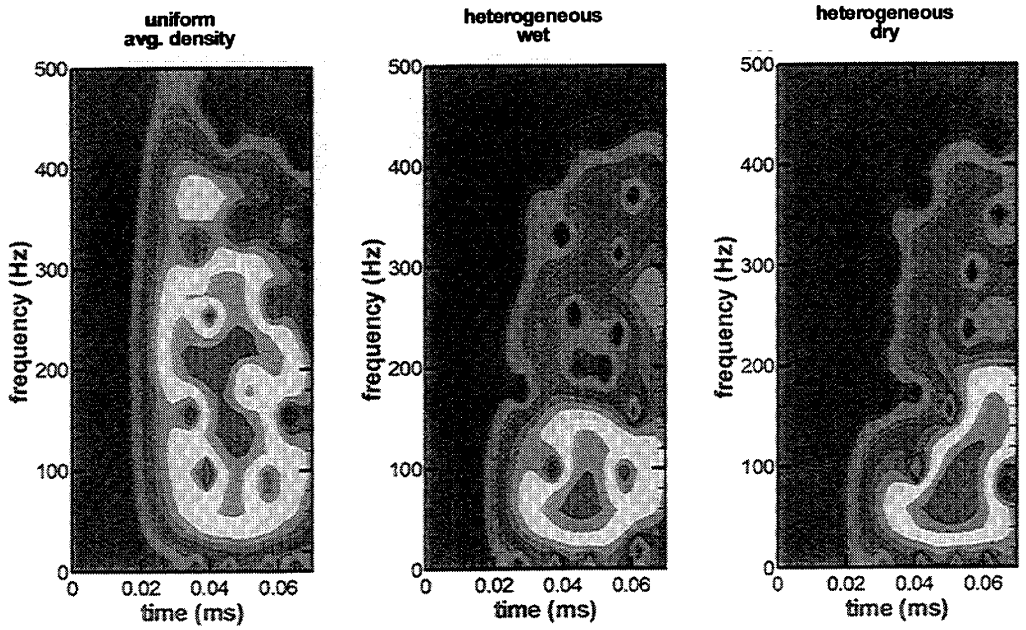

Figure 24. Time-frequency plots of core #41 synthetic waveforms. Amplitudes are in dB, and the color table spans 60 dB from blue to red.

We have computed attenuation values for the finite difference waveforms using a slightly modified spectral ratio technique. We take the waveform for the uniform core as a reference, and we compute attenuation in the heterogeneous cores in the spectral domain relative to this reference wave. Thus, most of the effects of geometric spreading and core end effects should be removed. The results are shown in Figure 25. We see a good agreement between the finite difference attenuation and the predicted stochastic attenuation, although the attenuation in the finite difference results is high at low frequencies. It is difficult to measure Q at low frequencies because the wavelength approaches the size of the core. The discrete reflections at the core ends also become more important and will impact the result.

Next we analyze the P-wave velocities from the 24 cores and we relate them with permeability for different flow units. We also use cores #7 and # 41 to investigate the effects of saturation and how cavities can be detected based on velocity analysis combined with poroelastic models. The velocity responses associated with the presence of the cavity of core #41 are analyzed and used to explained velocity distributions versus core permeability.

2. Velocity Analysis

The first part of this analysis established velocity-permeability relations grouped on the basis of flow zone indicators (FZI) on core samples. We applied the FZI concept given by Amaefule et al. (1993) to separate the P-wave velocity in flow units as a function of permeability. The second objective was to model the observed velocity core data using poroelasticity to determine squirt-flow lengths. The best fit between observed and calculated velocity provided the squirt-flow parameters and a better bulk modulus for each sample.

To determine the FZI units we produced scatter plots of RQI versus normalized porosity ϕ_z in logarithmic space for 44 samples. The RQI parameters are defined by

$$RQI = \sqrt{(k/\phi)} \qquad (5)$$
$$\phi_z = \phi / (1 - \phi)$$

As shown in Figure 26, the data fall on a straight line with a 45° slope. From the RQI plots we determined the FZI values of each hydraulic unit. The plots show that five hydraulic units, or flow, can be determined. These values are FZI = 8, 4, 2.5, 1.25, and 0.7, and they are used to calculate permeability and porosity curves, which are shown overlain on the horizontal versus porosity cross plots in Figure 27. Later, the FZI values were used to determine P-wave velocity versus log (permeability) curves to evaluate the Biot/squirt-flow mechanism for waves traveling in vuggy carbonates.

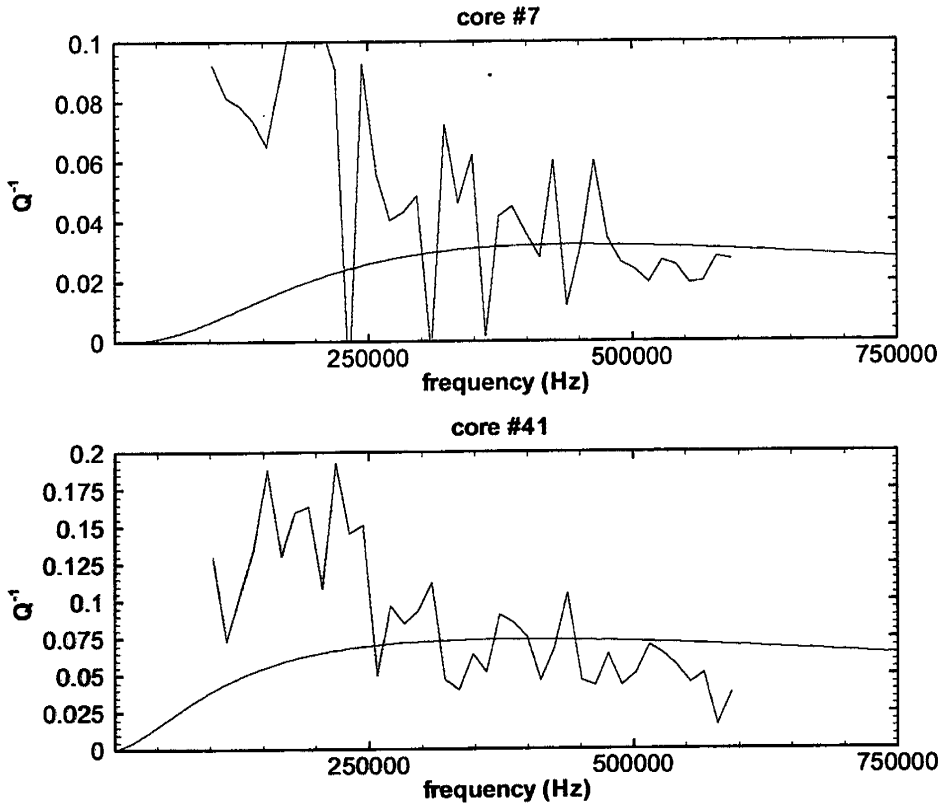

Figure 25. Computed Q from finite difference waveforms (red) compared to stochastic medium predictions. The attenuation in the finite difference results is high at low frequency because of discrete reflections at the core ends.

a. Velocity-porosity to permeability relation for the 44 samples

To correlate velocity and permeability parameters for the 44 samples, we first determined a relation between velocity and porosity based on the 24 samples available. This relation was obtained using a non-parametric transformation given in Datta-Gupta et al. (1997). Figure 28 shows the scatter plots between velocity and porosity and the function that best fits the points. This function has the following analytical representation,

$$Vp = -40.36\,\varphi_t^2 + 2094.4\,\varphi_t + 1182.8$$

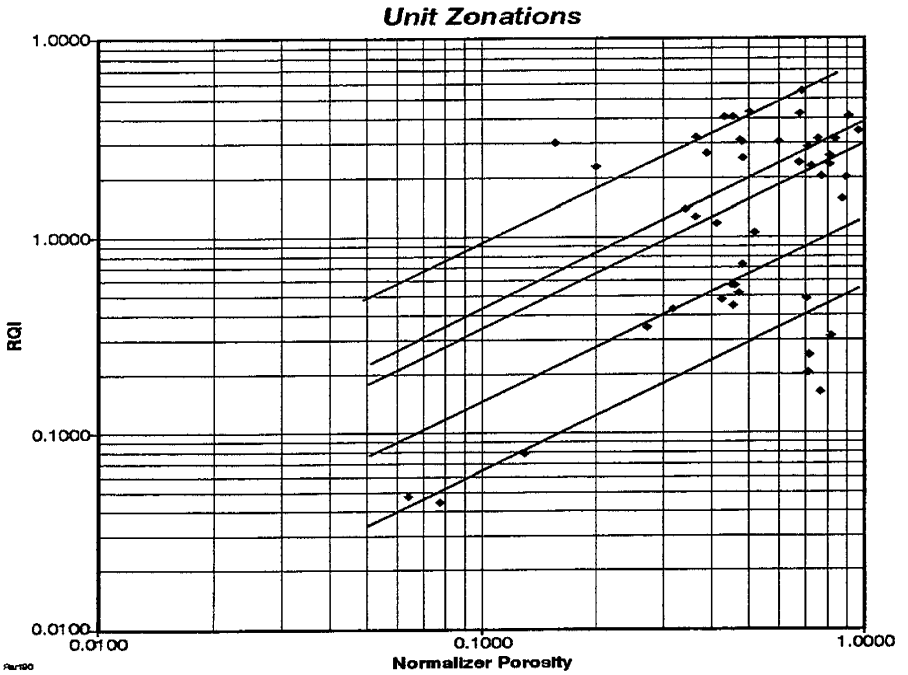

Figure 26. Crossplot of RQI versus log(ϕz) to determine FZI values.

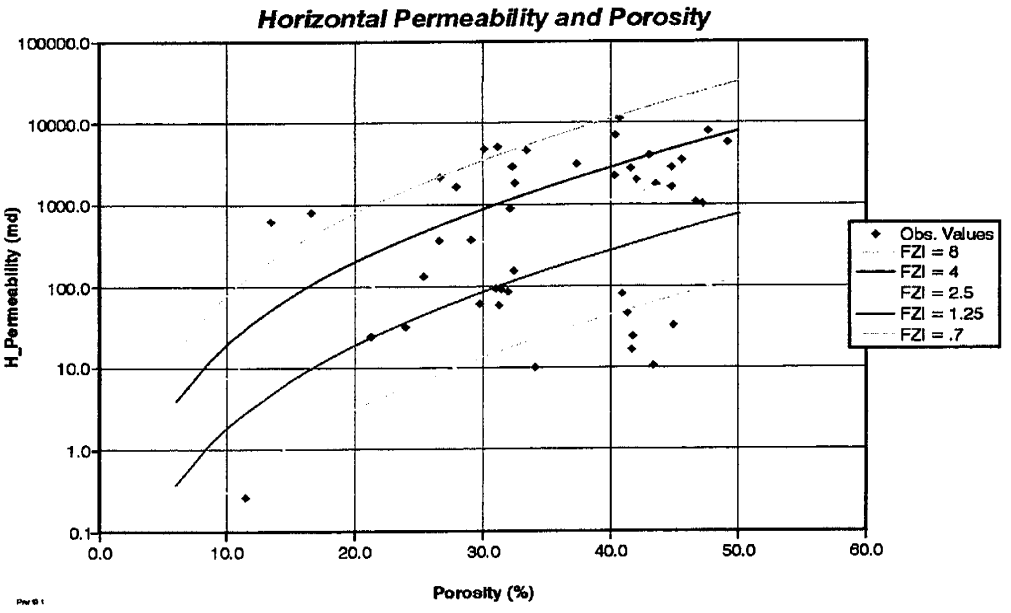

Figure 27. Crossplot of horizontal permeability and porosity (ϕ). The solid lines are calculated permeability and porosity for different FZI parameters.

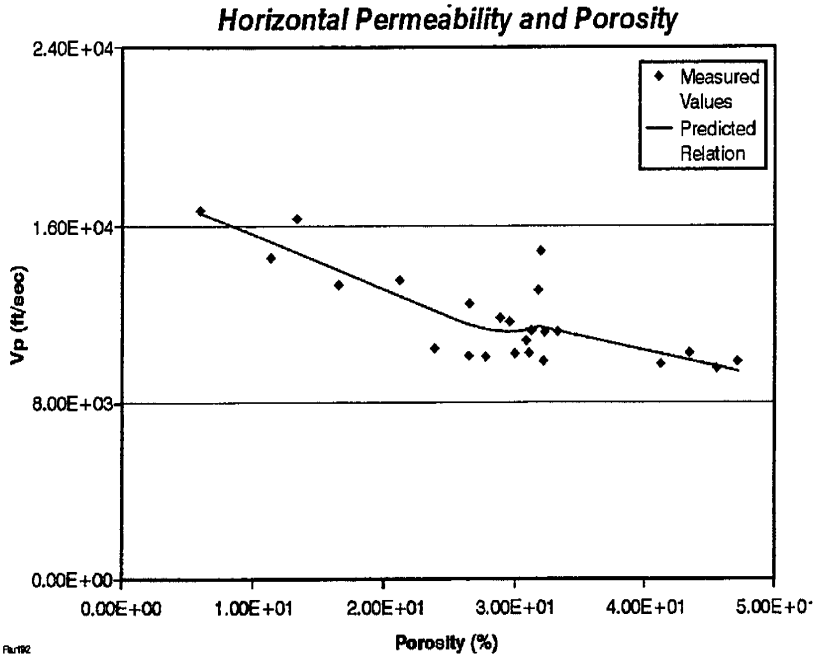

Figure 28. Crossplot of P-wave velocity versus porosity (ϕ). The solid line represents the best fit optimal transformation equation

where $$\varphi_t = 0.00155\,\varphi^2 - 0.1659\,\varphi + 3.344. \qquad (6)$$

Based on this equation we calculated 44 velocity values versus the 44 porosity values recorded for each of the samples. The predicted velocities are cross plotted with the horizontal permeability values for the five flow units in Figure 29. The plots show that velocity decreases as horizontal permeability increases, and when the flow units increase the horizontal permeability increases as well. The advantage of this analysis is that we can include all 44 core samples to predict velocity at the core scale. The disadvantage is that we are not including the observed velocity values. We will use this statistical approach for sonic log calibration and to calculate velocity-permeability relations at the borehole scale.

b. Velocity-porosity relation for the 24 velocity samples

Figure 30 shows the cross plots between velocity and horizontal permeability. The figure also depicts curves a, b, c, d, e, and f associated with six flow units. To determine the squirt-flow lengths for each sample based on the Biot squirt-flow mechanism, we used the theory given in Parra (2000). To calculate phase velocity, we used the rock physical and fluid

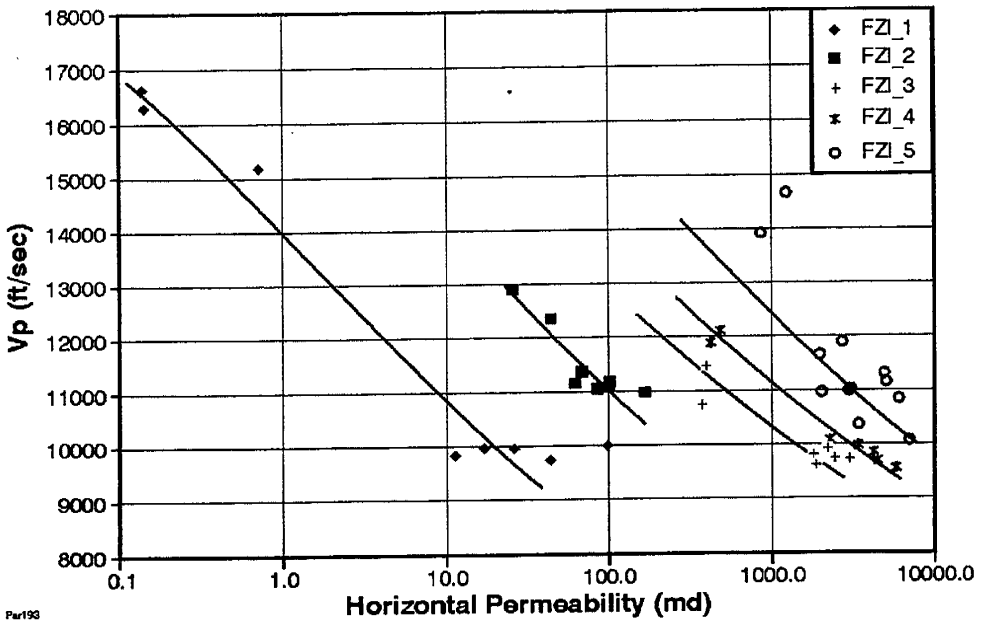

Figure 29. Crossplot of predicted P-wave velocity versus horizontal permeability. The 44 P-wave velocity values were produced using the velocity-porosity relationship determined in Figure 28.

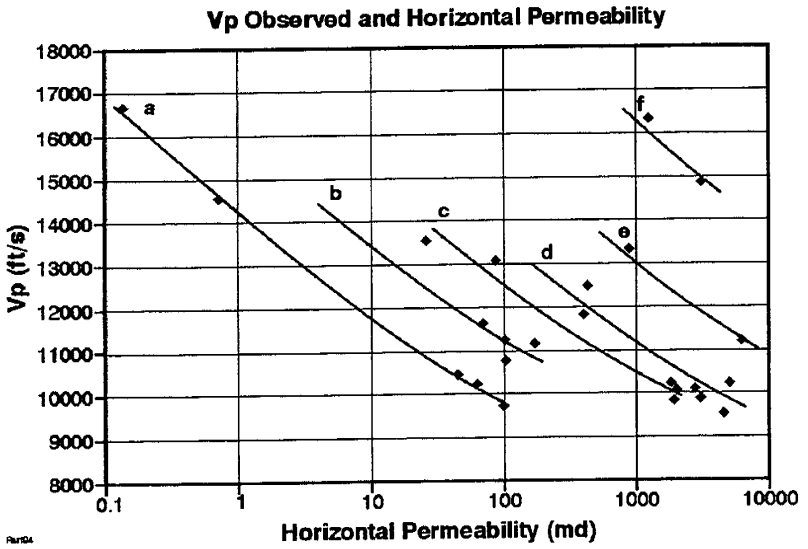

Figure 30. Crossplot of the 24 measured P-wave velocity samples versus horizontal permeability

properties of permeability, porosity, grain density, grain module, the drained Vp and Vs, fluid density, fluid velocity, and fluid viscosity. The model assumes that the poroelastic medium is homogeneous and isotropic. The drained Vp and Vs were calculated using Gasmman equations for fluid substitution. Thus, phase velocity data for the six flow units were calculated. In general, these curves show strong dispersion effects caused by the interactions between the rock matrix and fluid. The results of this analysis suggest a strong attenuation at ultrasonic signatures. We next selected the calculated velocities at 250 kHz, the frequency output used in the ultrasonic measurements. The calculated velocities are plotted in red, and the observed velocities are plotted in blue (see Figure 31). In the same scatter plots, the squirt-flow lengths for each of the calculated velocities are also included. There are a couple of velocities that we did not attempt to model. In this case we could not determine the undrained velocities using Gasmman equations. It is well know that Gasmman equations work better in homogeneous media and for low frequency velocity data. However, in our study, Gasmman equations worked well for predicting several of the dry velocities. For example, the observed and calculated velocities associated with the flow unit, FZI = 0.7, agreed very well in the low permeability region. In the high permeability region there was a slight difference between observed and calculated velocities. This difference is due to degree of heterogeneity of the pore structure. We can say that any difference between the calculated and observed data provides an assessment of the amount of vuggy porosity in the core.

For example, curve (a) in Figure 31 shows an increase in squirt-flow length as permeability is increased. The large permeability correlates with large flow lengths. In the same curve, the departures of the calculated velocities from the observed velocities reveals the amount of vuggy porosity that may be present in the sample. In curve (b) the fit between observed and calculated velocities is perfect. In this case the velocity is controlled only by intrinsic effects caused by the fluid flow. In curve (c), the cluster of observed and calculated velocities between 1 and 10 Darcies suggests that scattering effects due to vuggy porosity cause the difference between observed and calculated velocities. In this curve, a squirt-flow length of 2.5 cm was predicted, which correlates to the high permeability values. In a similar way, curves (d) and (e) show as the P-wave velocity decreases the permeability and the squirt flow length are increased.

The final curve (f) shows a big difference of about 1000 ft/s between the observed and calculated velocity for core #41. The image of this core gives some idea of what may happen as waves propagate in such a vuggy medium. Core #41 has two correlation lengths associated with the degree of heterogeneity of the vuggy porosity. In this heterogenous medium, Gasmman equations may not work very well. In fact, the dry Vp and Vs parameters were overestimated using Gasmman equations. As a result, we used measured dry velocity parameters for core #41. Although we used measured data, the calculated velocity based on the dry velocity data shows a big departure from the observed velocity. This demonstrates that the highly heterogeneous conditions of core #41 can be predicted by comparing observed and calculated modeled velocities, which are based on a homogeneous poroelastic model. To further verify this concept, we calculated velocities for all the cores, based on finite-difference modeling:

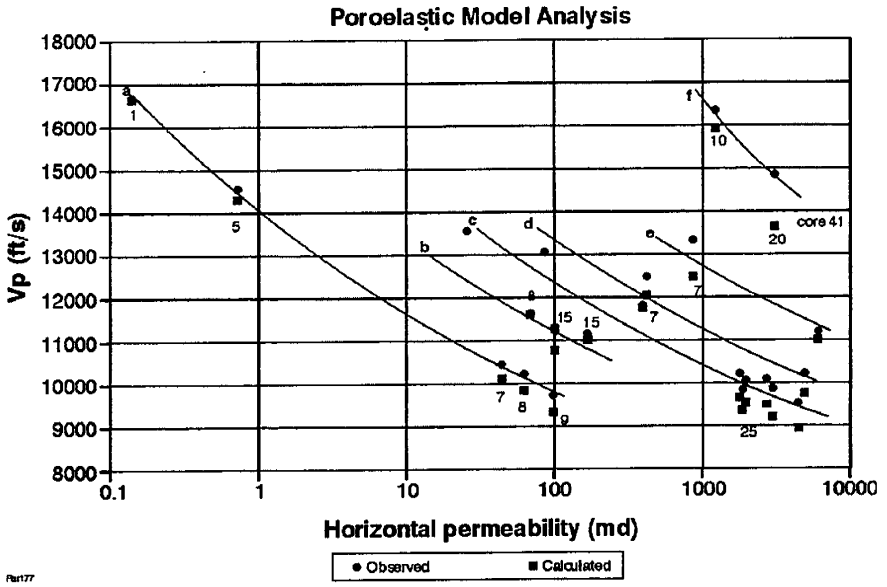

Figure 31. Cross plots of 24 measured and calculated P-wave velocity samples versus permeability. The curves represent six flow units. The numbers in the plot are squirt-flow lengths in millimeters

Uniform core (this is set as part of the model, not derived):
core 7: 4500 m/s
core 41: 3900 m/s

Water saturated, heterogeneous core:
core 7: 4520 m/s
core 41: 4360 m/s

Dry, heterogeneous core:
core 7: 4250 m/s
core 41: 3970 m/s

These velocities do not match well with the real core data because we do not yet have a good model to relate matrix density to P-wave velocity. However, we think the trends in velocity difference are reasonable. There is a 270 m/s difference between wet and dry conditions in core #7, and a 390 m/s difference in core #41. These are about the same differences that we observed using the poroelastic models.

In summary, the correlation between compressional wave velocity at the core scale yields a regression equation that can be used to relate velocity to porosity in a South Florida carbonate aquifer. In addition, the velocity versus horizontal permeability relation demonstrates that the compressional wave velocity strongly correlates with the horizontal permeability in each flow unit in the aquifer. This suggests that velocity tomography can be used to map permeability between

water wells. Furthermore, poroelastic modeling suggests that differences between observed and calculated data are due to the presence of vuggy porosity in the cores.

The next step in the analysis is to correlate log porosity with NMR-derived permeability using the RQI and FZI approaches. This will provide information as to how the flow units at the borehole scale relate with those at the core scale. It will also provide FZI values with which to cross plot the velocity from well logs with permeability for each flow unit. The velocity permeability relations will be compared with those derived from cores, and these results will provide a new understanding for deriving attenuation and dispersion mechanisms for carbonate rock with vuggy porosity. This in turn will be useful for modeling full waveform sonic and interwell seismic signatures based on velocity-permeability relations derived at the core and borehole scales.

F. NMR Core Measurements and Analysis

We conducted NMR core measurements on nine samples for NMR well log calibration. Saturated and desaturated T_2 distribution and capillary curves were obtained to derive permeability equations and we used a grouping technique to determine the T_2 cut-offs for the calibration.

1. Background: Flow Zone Indicators

Amaefule et al. (1993) developed an expression for FZI based on the Kozeny-Carman equation, which was first generalized to yield:

$$\sqrt{(k/\phi)}=[1/(\tau S_{gv}\sqrt{F_s})](\phi/(1-\phi)). \tag{7}$$

Equation (7) is formed by the parameters: k = permeability; ϕ = porosity, F_s = shape factor, τ = tortuosity, and S_{gv} = specific area per unit grain volume. The parameters F_s and τ represent pore throat tortuosity. In addition, Amaefule et al. (1993) introduced the concept of FZI units and defined the RQI. These two indices are expressed as:

$$\log (RQI) = \log (FZI) + \log (\phi_z) \tag{8}$$

where

$$RQI = 0.0314\sqrt{(k/\phi)} \tag{9}$$

and

$$FZI=1/(\tau S_{gv})\sqrt{F_s} \tag{10}$$

with

$$\phi_z=\phi/(1-\phi)$$

Equation (10) describes the relation between the pore space, defined by the parameters F_s, τ, and S_{gv}, and the FZI. FZI can be defined as the relation between the volumetric proportion of pore space to its geometric distribution. Using Equation (7), Amaefule et al. (1993) showed that the porosity-permeability relation within each FZI interval can be uniquely defined.

The relations τ^2, F_s, and S_{gv}^2 to permeability and porosity remain constant for data points with similar pore-space attributes; therefore, when RQI is plotted versus normalized porosity in logarithmic space, data fall on a straight line with a 45° slope. Where this straight line intersects the vertical axis (ϕ_z=1), the intercept is equal to log FZI. Samples with similar pore-space attributes exhibit similar vertical axis intercepts. Pore-space attributes control intrinsic flow properties, and samples with similar vertical intercepts belong to the same hydraulic unit. Any large deviation from this straight line indicates the existence of a separate hydraulic unit for which the relationship among τ, F_s, S_{gv}, porosity, and permeability is different.

2. Relation Between NMR Basic Equations and Flow Zone Indicators

The fundamental equations that relate the apparent relaxation rate for a single pore in the porous media are given by

$$1/T_2 = 1/T_{2b} + \rho\, S/V \qquad (11)$$

where

T_2 = observed transverse relaxation time.
T_{2b} = relaxation time of bulk fluid
ρ = surface relaxivity
S = surface area of the pore
V = volume of the pore body.

Since T_{2b} is significantly greater than the relaxation time T_2 in the porous medium, the above equation can reduced to:

$$1/T_2 = \rho(S/V) \qquad (12)$$

Georgi and Menger (1994) introduced a relation between the surface area-to-volume ratio of the pore space with the porosity and the specific surface per grain volume ratio (S_{gv}). This relation was also applied by Ohen et al. (1995) and is given by

$$S/V = S_{gv}\,(1-\phi)\,/\,\phi \qquad (13)$$

Thus, Equation (11) can be written as:

$$\rho T_2 = \phi\,/\,[S_{gv}\,(1-\phi)] \qquad (14)$$

or

$$T_2/\phi_z = 1/\rho\, S_{gv} \qquad (15)$$

Thus, we can relate Equations (13), (14) and (15) with the RQI defined by:

$$RQI = \sqrt{(k/\phi)} = \rho T_2 / (\tau \sqrt{F_s}) \qquad (16)$$

This suggests that RQI is related to relaxation time in the same way it is related to porosity group (ϕ_z). Therefore, using the above equations we can write a logarithmic equation for T_2 as

$$\log T_2 = \log (\phi_z) + \log [1/(\rho S_{gv})], \quad (17)$$

This equation relates relaxation time to porosity and forms the basis for the relaxivity group concept, which is analogous to the hydraulic unit concept. Equation (15) classifies samples that exhibit similar NMR relaxation (rock-fluid interaction) characteristics into a group. The average parameters for the group serve as calibration points for interpreting NMR logs. The factor $1/\rho S_{vg}$, often referred to as relaxivity product, represents both the relaxation power and textural attributes of the formation. As implied from Equation (15), the log plot of T_2 versus ϕ_z would result in a slope line, and $1/\rho S_{vg}$ would be constant for all data points on that slope line.

Formation rock samples or intervals with similar NMR relaxation characteristics lend themselves to the same group, with their log T_2 versus log ϕ_z clustering around the intercepting slope line. We refer to the samples or intervals from a given formation or reservoir with similar NMR characteristics as belonging to the same relaxivity group.

3. NMR Core Measurements and Analysis of Results

In performing the NMR core measurements, the nine samples were wrapped in Teflon material to prevent grain loss. The rock samples (1 inch in diameter and 1-1.5 inches in length) were saturated with a two-percent KCl brine solution of density 1.016 g/cm^3. The next step was to place the samples in a CoreSpec-1000 instrument that operates at a proton Lamor frequency of one Hz. The experiments measured the transverse relaxation time (T_2), with an inter-echo spacing time of 500 ms and various trains to achieve a high NMR signal-to-noise ratio. Once a sample was unloaded, a saturated weight was again recorded to confirm no loss of weight.

The T_2 spectrometry was performed on fully and partially saturated core plugs to obtain magnetization amplitude versus recovery time using the CoreSpec-1000. The output was processed using a multi-exponential fit based on the Levenberg-Marquardt algorithm. NMR porosity and relaxation time distributions were obtained from this process.

The nine samples were then loaded into a Beckman high-speed centrifuge and desaturated to 0.001 cm^3 stabilization. It took approximately 36 hours to desaturate each sample, using speeds corresponding to 300 and 400 psig capillary pressure. Immediately after the samples were unloaded from the centrifuge, they were wrapped in plastic wrap. They were then weighed, unwrapped, and individually loaded in the CoreSpec-1000 for NMR T_2 measurements. Each was weighed again immediately after the NMR measurement to check the material balance data.

Measurement results are given in Figures 32 a-i. These plots contain the T_2 relaxation distributions for both desaturated and fully saturated samples overlain on one plot. Optimum T_2 relaxation cut-off times (T_2c) for use in well log calibration were estimated by comparing the distribution curves.

Core analysis porosity was calculated from NMR measurements and from the Archimedes method. Figure 33 shows the relationship between NMR-derived porosity and helium porosity at a 0.50-ms echo spacing. The figure shows a reasonably good match. Since different relaxation rates are observed in the data associated with the different rock groups in the well, different T_2 cut-off times (T_{2c}) are needed to obtain the appropriate bound-volume index (BVI). As a result, we obtained three relaxation groups from the nine samples (see Figure 34). This was done by plotting log T_2 versus ϕ_z and by fitting Equation (17). The cut-off values, permeability, and porosity, as well as several other important parameters, are given in Table 1.

The main objective of building a model based on FZI-NMR core data is to be able to construct a reliable algorithm for accurately calculating log permeability. By using FZI, which comes from hydraulic unit analysis, we can model all pore types encountered in a reservoir or aquifer. In this study, we also determined the FZI parameter in terms of the BVI data. For example, a model was developed to determine permeability in terms of the BVI and FZI parameters for each T_{2c}. These cut-off transverse relaxation times for the nine samples range from 5 to 200 ms. Thus, relaxation group 1 has an average T_{2c} of 128 ms, group 2 has an average T_{2c} of 85 ms, and group 3 has an average T_{2c} of 6.5 ms (see Table 6).

Table 6. T_2 Cut-off.

Group	T2 cutoff	$T2_i/\phi_z$
1	128 ms	> 0.3728 s
2	85 ms	0.0729 - 0.3728 s
3	6.5	< 0.0729 s

To take the three cut-offs into consideration, we constructed an expression for the FZI given by (Ohen et al., 1999)

$$FZI = \left[\frac{b\left(1 - \frac{BVI}{\phi}\right)}{1 + a\left(\frac{BVI}{\phi} - 1\right)} \right]^c \tag{18a}$$

To obtain permeability based on FZI values and NMR porosity, we use the relation given by

$$k = 1014\, FZI^2 \frac{\phi^3}{(1-\phi)^2} \tag{18b}$$

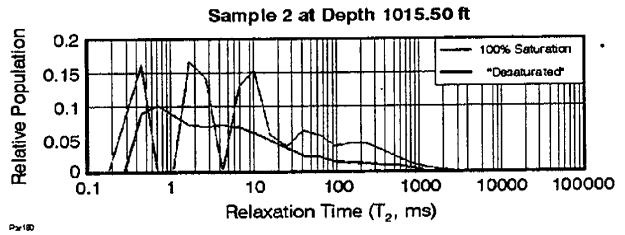

BVI = 5.6
POR. = 7 %
PERM. = .04 md

a.

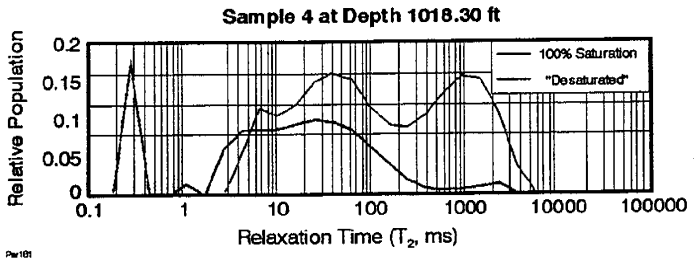

BVI = 4.1
POR. = 13. 7 %
PERM. = 1.14 md

b.

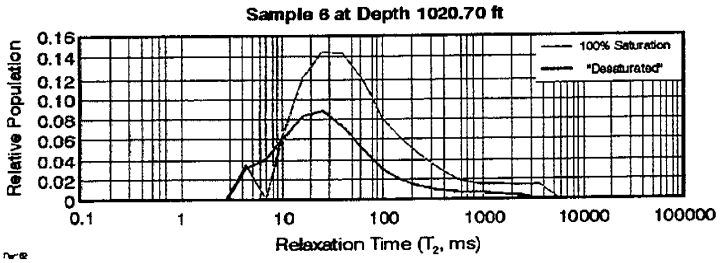

BVI = 6.61
POR. = 10 %
PERM. = 0.17 md

c.

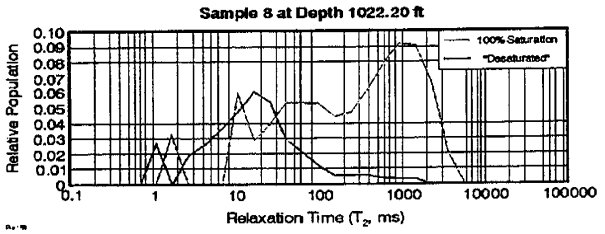

BVI = 5.1
POR. = 28.7 %
PERM. = 20 md

d.

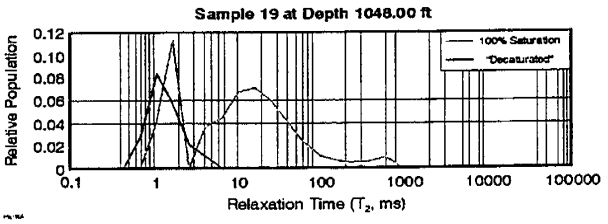

BVI = 8.23
POR. = 20.7 %
PERM. = 4.1 md

e.

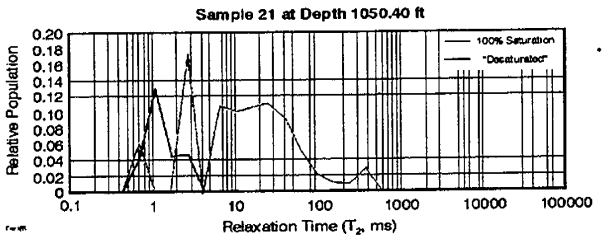

BVI = 9.8
POR. = 33.6 %
PERM. = 45.4 md

f.

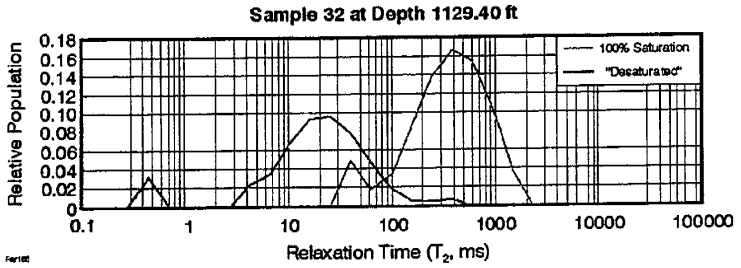

BVI = 4.
POR. = 42.2%
PERM. = 345 md

g.

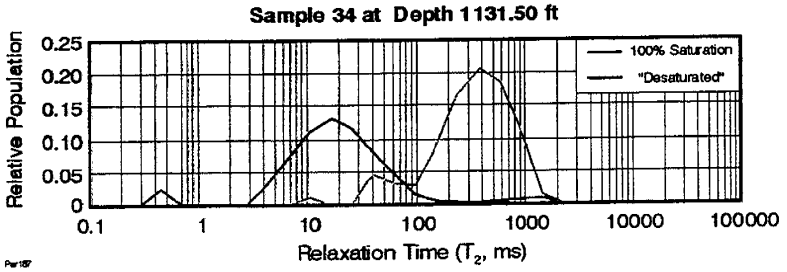

BVI = 3.8
POR = 43.9 %
PERM = 492 md

h.

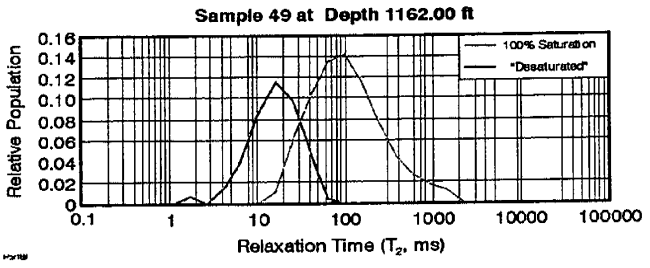

BVI = 10.22
POR. = 41.1 %
PERM. = 97 md

i.

Figure 32. Comparison of T_2 distributions for desaturated and 100% brine saturated samples (2,4,6,8,19,21,32,34, and 49) for determination of T_{2c} cut-off.

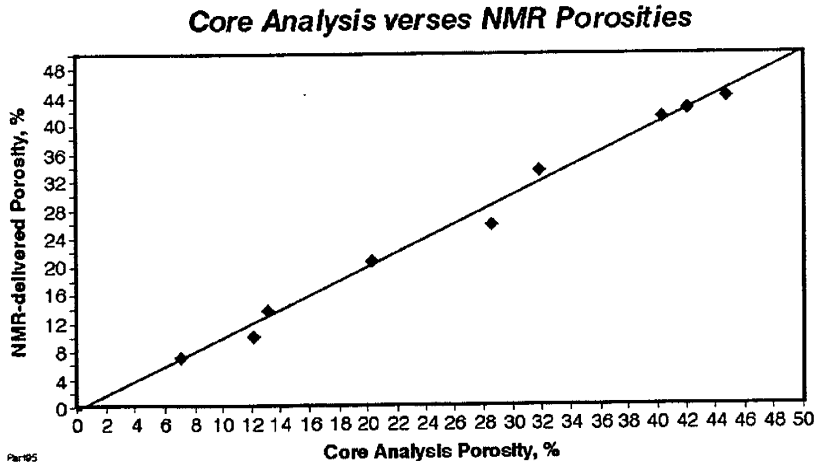

Figure 33. Cross plot of NMR-derived porosity and core analysis porosity.

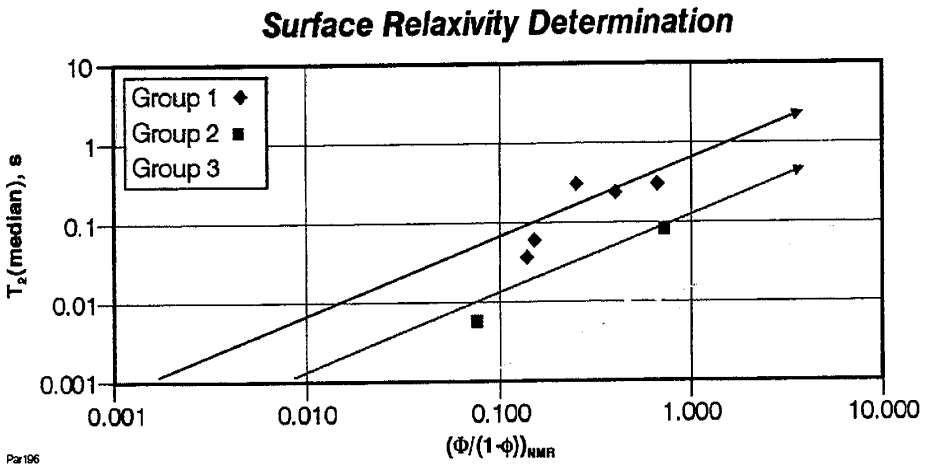

Figure 34. T_2 median versus normalized porosity (ϕz). The lines illustrate three major relaxivity groups for NMR well log calibration.

The T_{2c} cut-off parameters are given below. They were used to determine the BVI values, which were inserted in Equation (18a) to calculate the FZI units required to calculate permeability. Equation (18b) was used to calculate permeability from the NMR well logs recorded in well PBF10. The method used to calibrate NMR well logs is as follows:

1. Cross plot the NMR T_2 at 50 percentile (media) with normalized porosity (ϕ_z) from the well log of well PBF10.

2. Use the logarithmic Equation (15) to plot straight lines with a 45-degree slope. The objective is to separate the T_2 values into relaxation groups at the borehole scale. We expect that several groups will be derived.

3. Match the relaxation groups from well logs with those obtained from cores:
   (a) If the T_2/ϕ_z from well logs falls at or above 0.3725 second, the zone belongs to core relaxivity group 1, and we use $T_2c = 128$ ms.
   (b) If the T_2/ϕ_z from well logs falls between 0.3728 and 0.07288 second, the zone belongs to core relaxivity group 2, and we use $T_{2c} = 85$ ms.
   (c) I f the T_2/ϕ_z falls between 0.07288 and 0.04946 second, the zone belongs to relaxative group 3, and we use $T_{2c} = 6.5$ ms.

4. Use the T_{2c} cut-offs to determine the BVI from the well logs.

5. Calculate FZI and permeability using Equation (11). A plot of FZI versus BVI/ϕ is given in Figure 35.

G. NMR Well Log Calibration

NMR well logs from the Floridan aquifer were calibrated for permeability by using a variable T_2 cutoff to predict the irreducible bound fluid volume (BVI). The BVI was converted to permeability through the FZI method of Ohen et al., 1999. Values for the variable T_2 cutoff were obtained through NMR measurements on fully saturated and centrifuged cores.

1. Approach

The original method of computing permeability from NMR well logs using a fixed T_2 cutoff of 90 ms produced unsatisfactory results in the predominantly carbonate rocks of the Floridan aquifer. The primary reason for this is that the region of interest comprises several varied lithological units including sandstone and carbonates with varying degrees of vuggy porosity. A more accurate method of computing permeability takes into account the variations in pore structure which occur throughout the aquifer.

We used a variable T_2 cutoff to predict the BVI. The T_2 cutoffs were derived from experimental measurements on nine cores from the Floridan aquifer. The cores were fully saturated with water, and NMR measurements were taken before and after centrifuging. By comparing the T_2 distributions of the fully saturated cores and the cores with irreducible saturation,

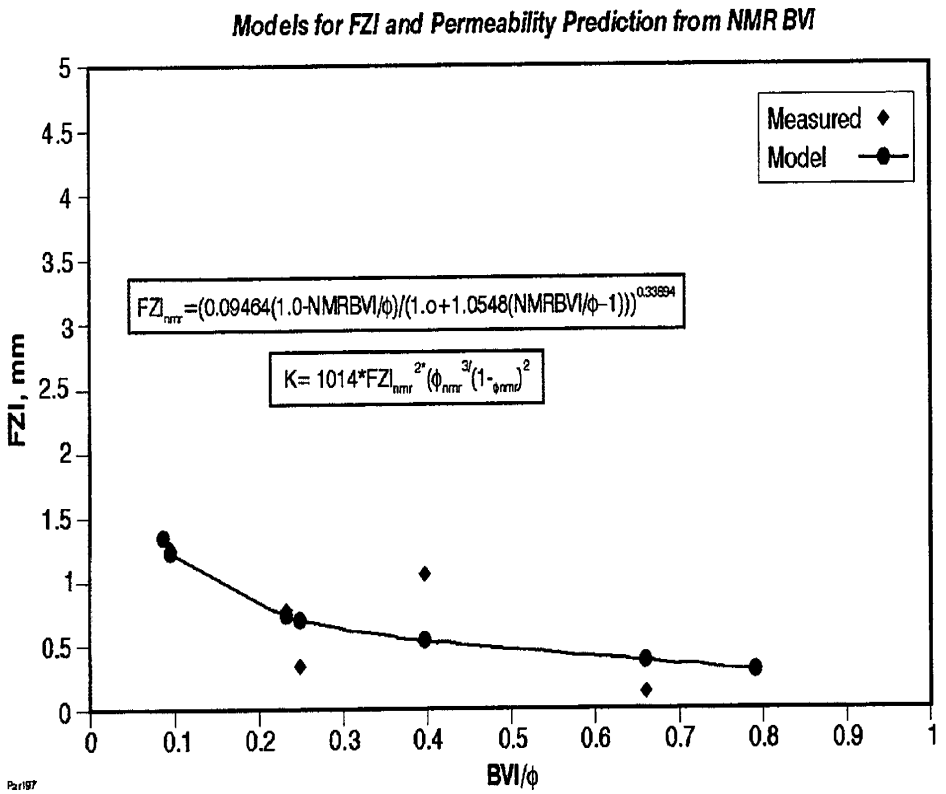

Figure 35. Crossplot of FZI (NMR) verus BVI /ϕ. The figure shows the models for FZI and permeability prediction from NMR BVI. The measured and calculated data are shown.

we obtained a T_2 cutoff separating the pore space which participates in fluid migration from the non-participating pore space. The nine cores examined so far appear to naturally separate into three relaxivity groups, based on the product of the NMR surface relaxivity and the surface area-to-volume ratio of the pore space. See Section II.F on NMR core measurements in this report for more details. Here, T_{2i} is the T_2 value of the median pore size, and the normalized porosity ϕ_z is equal to $\phi/(1-\phi)$.

The NMR well log is divided among these three groups by examining the median T_2 value at each depth. The BVI is then computed as the porosity with associated T_2 values less than the T_2 cutoff for that group. Once the BVI is known, we compute the flow zone indicator value and permeability for that depth using equations (18a) and (18b). Thus, the parameters *a*, *b*, and *c* are determined from the best fit to the core permeability measurements of the same nine cores used in the NMR experiment. Based on these nine cores, the optimal values are

$a = 1.05$
$b = 0.0946$
$c = 0.337$

2. Results

The result of using the variable T_2 cutoff based on the nine cores is shown in Figure 36. The overall effect is to lower the permeability, especially from the highest permeability zones. In these regions, the permeability is reduced by one order of magnitude. Some abrupt changes in permeability are also introduced, as the T_2 cutoff can vary sharply from one depth to the next. Also, the sandstone layer from 1050-1060 feet is probably predicted as having too high a permeability (~50 md) with this reprocessing, although the original prediction of $k < 0.1$ md is probably too low.

We expect some improvements in the permeability correlation if more cores are included in the study. Tests are now under way on an additional nine cores, which will double the amount information available. Presently, relaxation groups 2 and 3 are based only on two core measurements each, not a statistically significant sample. Unfortunately, the use of this method to calibrate NMR well logs can be prohibitively expensive and time-consuming for small producers because of the large number of core NMR measurements.

We are also beginning to explore methods of calibrating NMR well logs based on capillary pressure, or the shape of the T_2 distribution. These methods do not require core NMR measurements, but only core permeability measurements. Such measurements are relatively inexpensive and can be done fairly rapidly at many private service companies. If these new methods provide a degree of accuracy comparable or superior to the relaxivity group method, then they will be much more cost-effective.

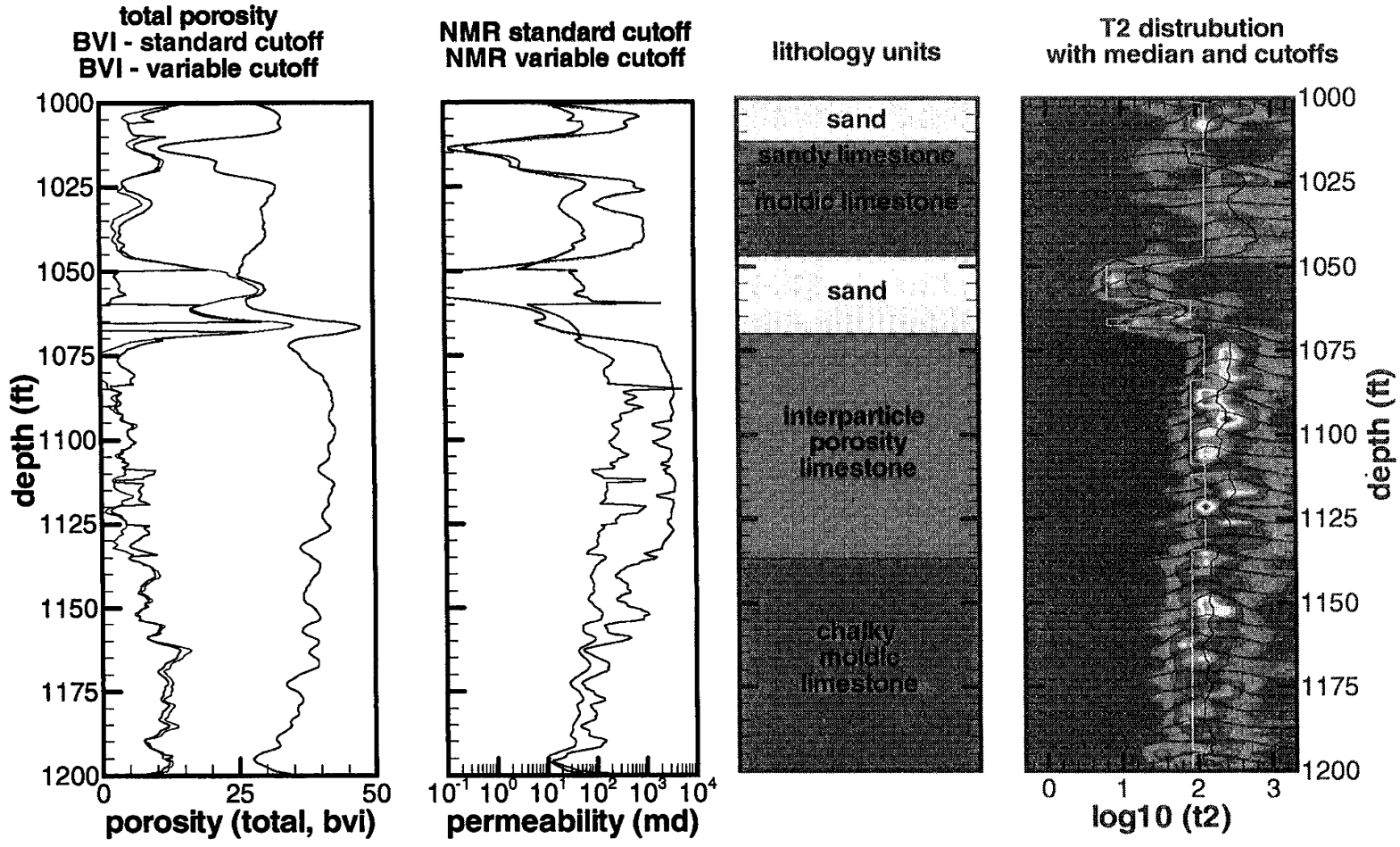

Figure 36: Interpretation of NMR logs using both a fixed (90 ms) T2 cutoff and a variable T2 cutoff derived from core NMR measurements. The far right plot shows the T2 distribution in the color scale and overlain red lines. The black curve is the median T2 value, used with the porosity to discriminate among relaxivity units. The white line is the variable T2 cutoff.

H. Acoustic Well Log Analysis

1. Flow Zone Unit Separation from Florida Well Logs

We apply the flow zone unit separation often employed in core analysis to well logs from the Florida carbonate aquifer. Treating each unit independently, we seek to find accurate correlations for predicting porosity and permeability from Vp. The ultimate application will be to create an interwell porosity and permeability map when we acquire high-resolution crosswell seismic data later this year.

Core analysts have recently emphasized the concept of dividing formations into natural flow units based on their petrophysical properties (Ohen et al., 1999). Some of the parameters defined in this concept are the reservoir quality index and the normalized porosity:

$RQI = 0.0314 \sqrt{k/\phi}$
$\phi_z = \phi / (1 - \phi)$

Analysts have found that the ratio of RQI to ϕ_z is often fairly constant for similar types of rock fabric, and so use the flow zone indicator,

$FZI = RQI / \phi_z$

as a means of identifying flow units. A plot of the log-derived FZI from the PBF10 well in Florida shows that large changes in FZI are well-correlated with known lithological boundaries (Figure 37).

We have divided the well log values into five groups on the basis of the computed FZI of each depth point in the well log. These groups are

1. $FZI < 0.2$,
2. $0.2 < FZI < 0.5$,
3. $0.5 < FZI < 1$,
4. $1 < FZI < 2$, and
5. $FZI > 2$.

Figure 38a shows these groups in RQI and ϕ_z space, while Figure 38b shows the physical location of points in each group. For the most part, the FZI groups are physically piecewise contiguous, although they may be in several sections over the 200-foot study interval. In Figure 38c, we show how the P-velocity is correlated with permeability in each FZI group. The correlation is reasonably good within each unit, and there is a well-defined separation between the units along the permeability axis. The correlation of porosity with P-velocity is shown in Figure 38d. There is not so much separation here along the porosity axis, but again there is at least a fair correlation between velocity and porosity within each unit. An expanded view of the relation between Vp and permeability is shown in Figure 39.

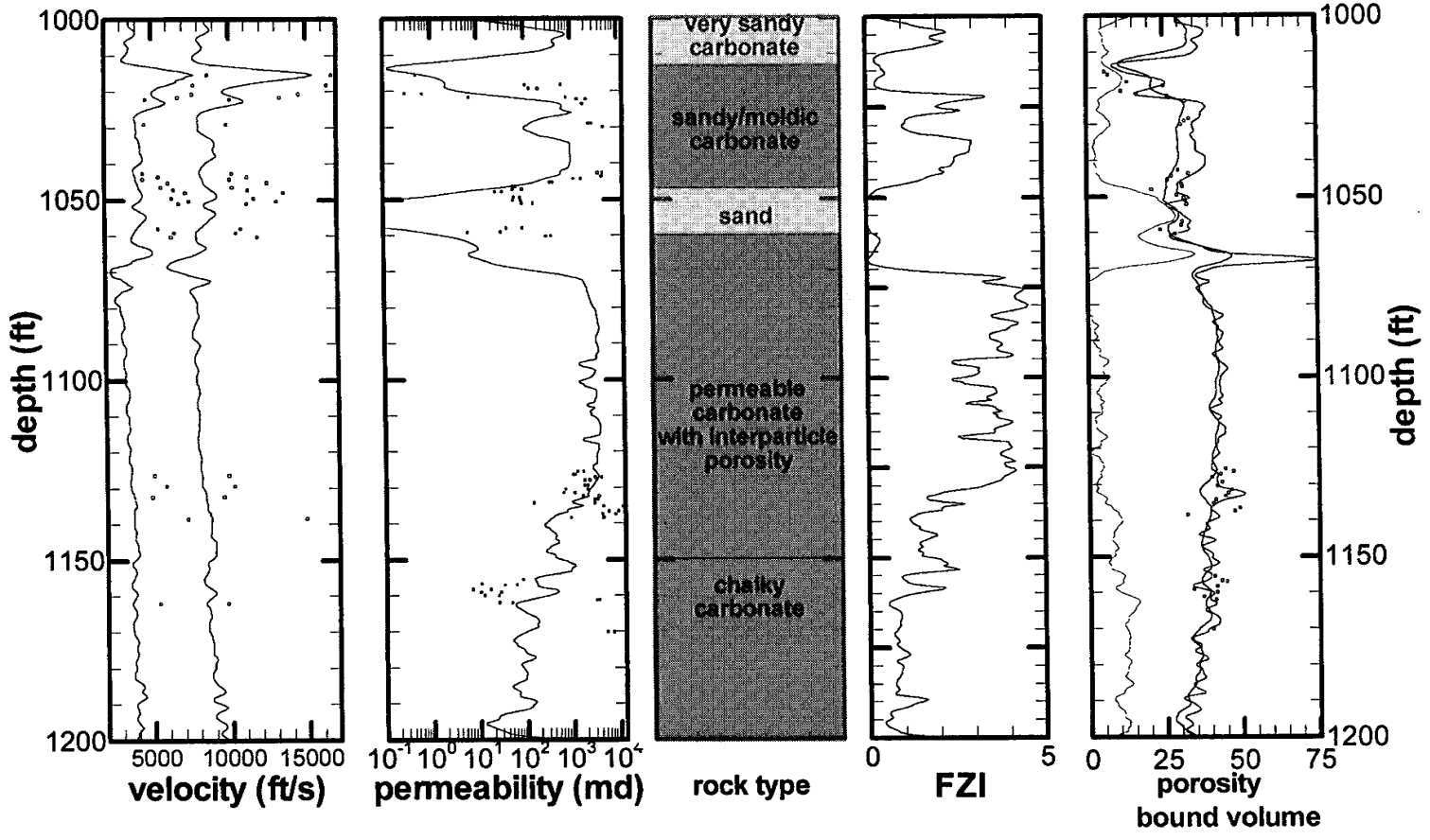

Figure 37. Comparison of well log and core values, along with lithology and FZI computed from well logs.

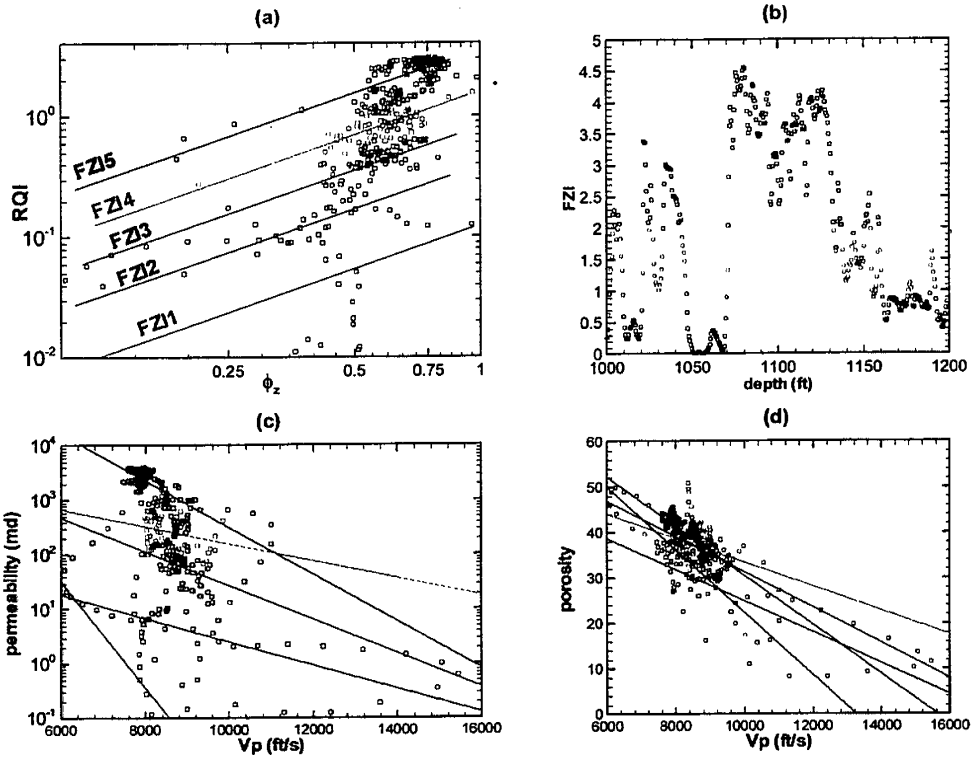

Figure 38. Separation of the well logs by FZI. (a) Plot of well log values in RQI and ϕ_z space. (b) Plot of FZI groups versus depth. (c) Correlation of permeability and P-velocity by FZI group. (d) Correlation of porosity and P-velocity by FZI group.

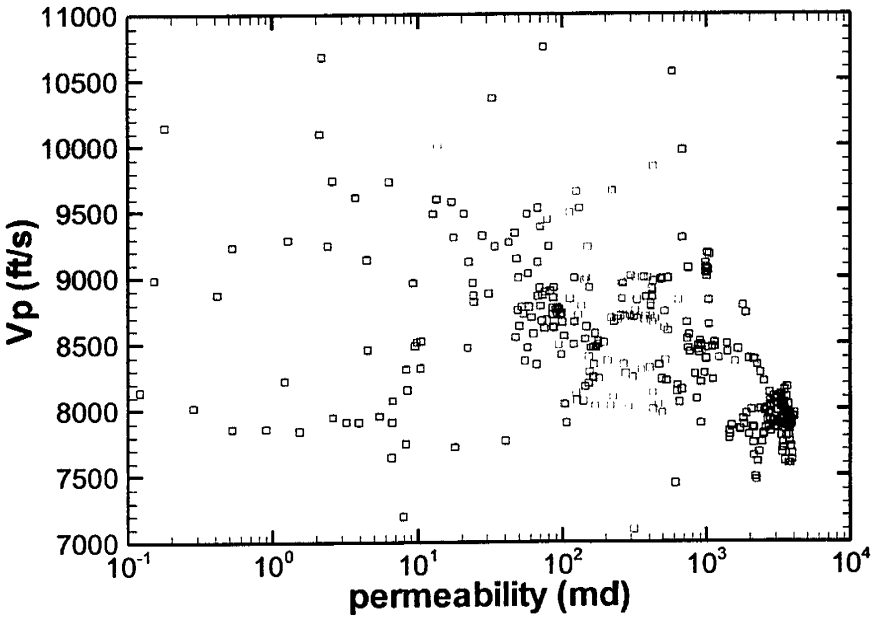

Figure 39. Plot of Vp as function of permeability by FZI group.

In Figure 40, we compare the FZI computed from well logs to that computed from the core measurements. Overall, the agreement is fair, although several individual cores have FZI values far from the well log FZI. The agreement is particularly poor in a moldic limestone section ranging in depth from 1020 to 1050 feet. In this section, the well log permeability is significantly less than the core permeability, leading to a poor match in FZI values.

2. Attenuation and Dispersion Based on the BISQ Mechanism

The poroelastic model to calculate the P-wave velocity at 250 kHz for each flow unit curve is based on the squirt-flow mechanism. To determine the phase velocity and attenuation of the vuggy carbonate rocks in the sonic log frequency, we chose the data from cores in curve (b) of Figure 31. The attenuation and dispersion curves for this flow unit are given in Figure 41(a-b). In general, the curves show strong dispersion effects caused by interactions between the rock matrix and fluid. The results of this analysis suggest a strong attenuation in the frequency range between 1,000 and 15,000 Hz. We also observed that the peak frequency moves toward the low frequency range as the squirt-flow length is increased. In this case the flow is associated with connectivity between the vugs and the matrix. That is, as permeability increases, attenuation becomes greater. This analysis implies that sonic logs have the potential to capture fluid flow interactions between the matrix and the vugs. Specifically, the P-wave attenuation and phase velocity will capture the degree of connectivity between the matrix porosity and the vugs or between vugs.

3. Analysis of Full Waveform Sonic

Monopole and dipole sonic data were recorded in the PBF10 borehole intersecting the Floridan aquifer. The objective was to extract Stoneley wave permeability from sonic logs and compare Stoneley wave permeability with NMR-derived permeability to determine which technique is more suitable to use on a regular basis to characterize the aquifer. Since the Stoneley waves are sensitive to small changes on the diameter of the borehole, and the PBF 10 caliper log shows variability as a function of depth, the Stoneley permeability does not show good results in the upper and the bottom part of the zone of interest (i.e., between 1000-1200 ft), Stoneley wave permeability does not produce good results. However, the P-wave events are easy to identify in the microseismogram of Figure 42a. The spectra of the acoustic waveforms show the attenuation of the P-wave events associated with the vuggy porosity in the region between 1014-1024 feet (see Figure 42b). The next step in the analysis was to produce synthetic signatures based on the core data containing vugs and compare them with the observed data to determine whether we could infer from the P-wave sonic data the degree of connectivity between vugs and between the matrix and vugs. To fully evaluate this concept we used the NMR-derived permeability log, porosity log, the density log, the Vp and Vs logs and the lithology.

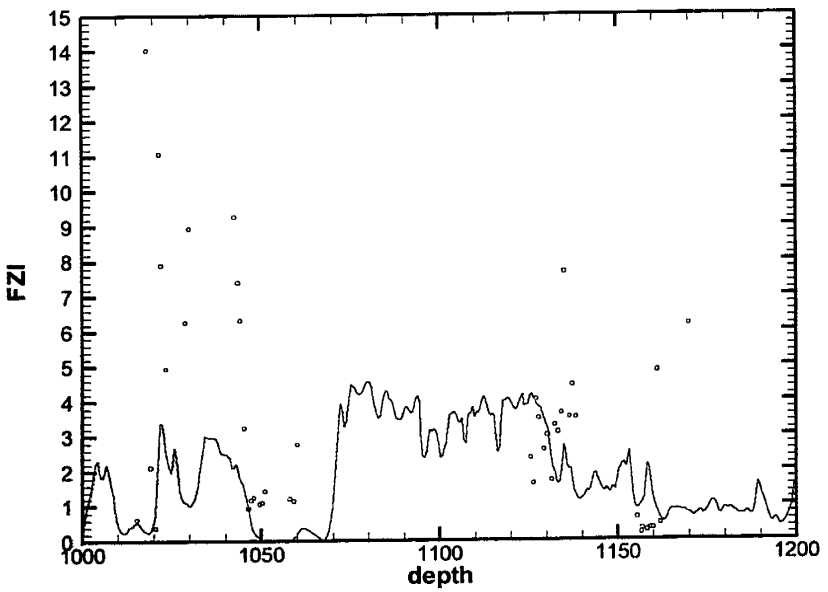

Figure 40. Comparison of FZI from well logs (red) and core measurements (green).

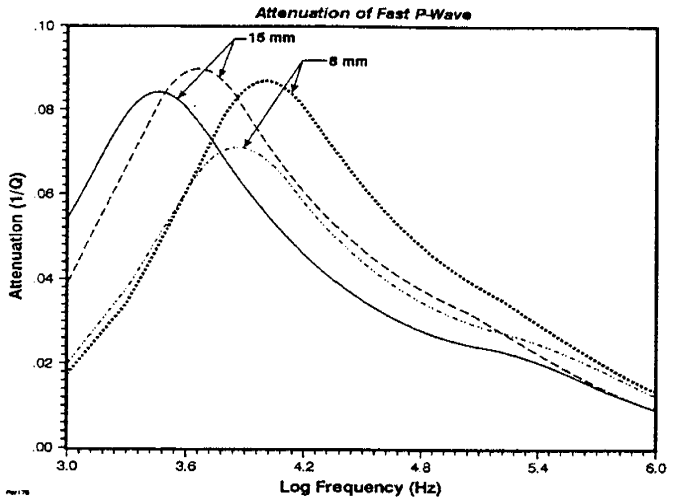

a.

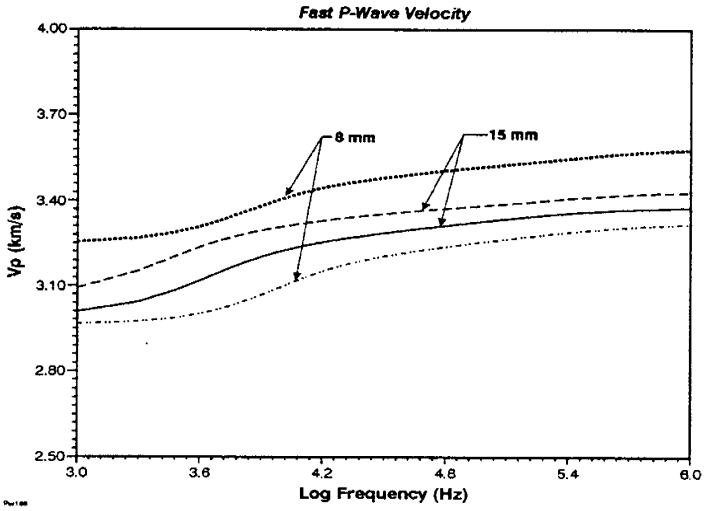

b.

Figure 41. Attenuation and dispersion curves of 4 samples. Response calculated for squirt-flow lengths of 8 and 15 mm.

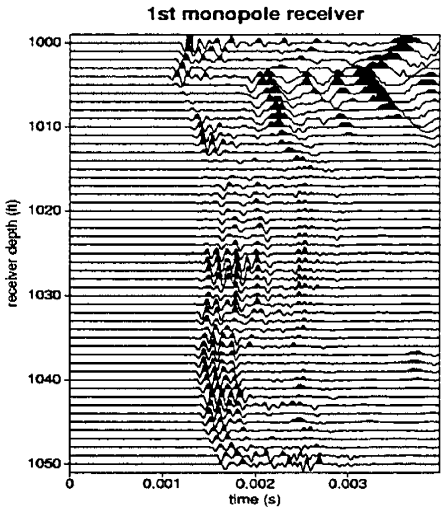

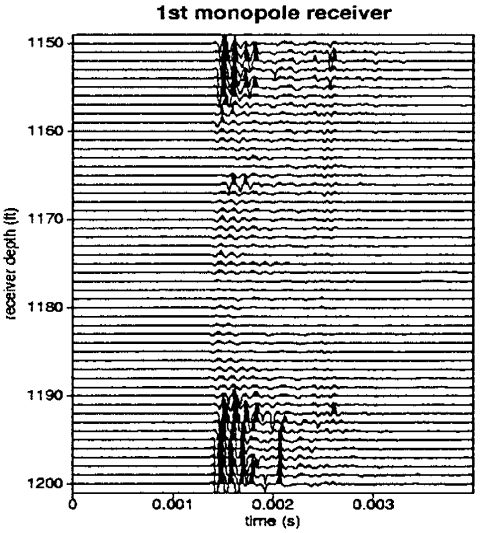

(a) (c)

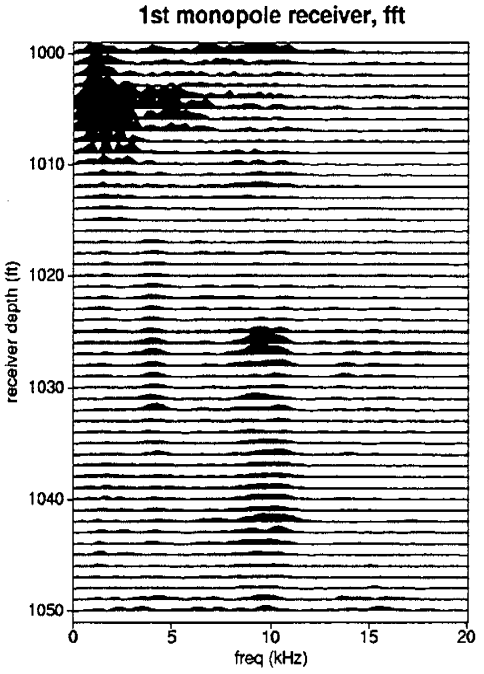

(b)

Figure 42: (a) Full waveform sonic micro-seismogram, (b) its spectra from first receiver, showing data only between 1000-1050 ft, and (c) Full waveform sonic micro-seismogram showing data only between 1150 -1200 ft.

I. Conclusions and Discussions

We used digital processing of OM, SEM and X-ray CT images, as well as petrography, to characterize the pore space and the pore system of vuggy carbonates in South Florida. The results of this analysis provided supportive information to evaluate NMR well log signatures for NMR well log calibration. We used saturated and desaturated NMR core measurements to estimate the irreducible water in the rock (associated with the matrix porosity) and estimated the variable T_2 cut-offs for the NMR well log calibration. The measurements established empirical equations to extract permeability from NMR well logs in South Florida. We demonstrated by the analysis of synthetic and observed NMR signatures that NMR well logs capture only the micro- and macro-porosities of the carbonate rock.

In addition, NMR well log signatures supported with thin sections and core images defined the matrix porosity of the carbonate rock, and the ultrasonic data detected vuggy porosity. In particular, NMR synthetic signatures based on pore size distributions, which were determined from image processing, fit very well the observed NMR well log signatures. This interpretation produced a relaxivity of 1.5 μm/s for the wackestone sample, and 5 μm/s for the grainstone sample. These two values are acceptable values for carbonates. We expected the presence of sands in the grainstone to increase the relaxivity compared to that of wackestones, as sandstones have higher relaxivities than carbonates. In addition, we found that the matrix porosity of both samples was captured by the NMR well log signatures. The vuggy porosity was not clearly identified by NMR measurements.

The CT image processing and the ultrasonic analysis provided information to characterize the acoustic signatures caused by interconnected and connected vugs in core samples. That is, connected and separated vugs can be detected with ultrasonic measurements. Moreover, the ultrasonic core and geotechnical data provided velocity versus porosity relationships based on flow zone indicators. These relationships, input in a poroelastic modeling program, helped us determine the squirt-flow lengths associated with the fluid flow between the matrix and the vugs and between the vugs. Based on this information, attenuation and dispersion curves of the vuggy carbonate rock were simulated in the frequency range of sonic logs. The velocity dispersion model results based on the pore structure and core data indicated that vugs in the formation surrounding the borehole strongly attenuate the full waveform monopole data. This suggests that full waveform sonic data can be used to image the vuggy porosity of carbonates. Therefore, NMR well logs, together with acoustic data, can be used to image the carbonate formation surrounding the borehole.

References

Amaefule, J.O., Attunbay, M., Tia B.D., Kersey, D.G., Keelan, D.K. (1993) Enhanced reservoir description: using core and log data to identify hydraulic (flow) units and predict permeability in cored intervals/wells: SPE 26436, 1-16.

Xu, G., and Datta-Gupta, A. (1996) A new approach to seismic data integration during reservoir characterization using optimal non-parametric transformations: SPE 36500.

Ohen, H.A., Enwere, P.M., and Kier, J. (1999) "NMR relaxivity grouping or NMR facies identification is key to effective integration of core nuclear magnetic resonance data with wireline log," paper SCA-9942 in Society of Core Analysts 1999 International Symposium *Proceedings*.

Ohen H.A., Ajufo, A., and Curby, F.M. (1995) A hydraulic (flow) unit based model for the determination of petrophysical properties from NMR relaxation measurements: SPE 0304626.

Georgi, D.T., Menger, S.K. (1994) Reservoir quality, porosity and permeability relationships. Paper presented at the Mintrop Seminar in Germany.

Parra, J.O. (2000) Poroelastic model to relate seismic wave attenuation and dispersion to anisotropy: *Geophysics*, 65, 201-202.

Hokstad, F., Sollie, R., and Nes, O.-M. (2000) Finite-difference modeling of viscoelastic wave propagation in core samples, paper RPB P1.7 in *70th Ann. Int. Mtg. Expanded Abstracts*, Soc. Expl. Geophys.

Anselmetti, F. S., Luthi, S., and Eberli, G. P. (1998) Quantitative characterization of carbonate pore systems by digital image analysis, *AAPG Bulletin* 82, pp. 1815-1836.

Chang, D., Vinegar, H., Moriss, C., and Straley, C. (1997) Effective porosity, producible fluid, and permeability in carbonates from NMR logging, *Log Analyst* 38, pp. 60-72.

Ramakrishnan, T.S., Schwartz, L.M., Fordham, E.J., Kenyon, W.E., and Wilkinson, D. J. (1999) Forward models for nuclear magnetic resonance in carbonate rocks, *Log Analyst* 40, pp. 260-270.

Bennet, P.G., Linton, P.F., and Rectenwald, E.E (2001) Hydrology investigation of the Floridan Aquifer system, Western Hillsboro Basin Palm Beach County, Florida: South Florida Water Management District, 3301 Gun Club Road, West Palm Beach, Florida 33406.

III. TECHNOLOGY TRANSFER ACTIVITIES

A home page for this project can be found on the SwRI web site at http://www.reservoirgeophysics.swri.org. The home page includes the first and second year Annual Reports as .pdf files. The home page also includes presentations and papers resulting from Phases I and II. We include two manuscripts as Sections III.A and III.B that have been submitted to *Petrophysics* and *Geophysics*, respectively.

A. A Poroelastic Model with Azimuthal Anisotropy to Analyze Flow Unit Responses at the Siberia Ridge Field, Greater Green River Basin

1. Abstract

A modeling scheme is presented and applied to analyze the response of reservoir flow units to a variety of acoustic/seismic measurement techniques, and to determine the frequency band in which flow units can be observed and characterized. The model estimates attenuation in a broad frequency range to include sonic, crosswell, VSP, and 3D seismic scales. Because flow units in a reservoir are characterized by permeability, porosity, and fluid saturation, and because fluids are characterized by their viscosity, density, and velocity, we use the theory of poroelasticity. This theory provides the physics involved in the interactions between the fluid and the rock matrix as an acoustic wave propagates in the medium. Energy losses due to the relative movement of pore fluids and the rock matrix are described using the unified Biot and squirt-flow theory. We apply this theory to a layered poroelastic medium with azimuthal anisotropy to analyze whether flow units penetrated by a borehole can be detected at seismic scales (crosswell, VSP and 3D seismic). We model a sand-shale-coal sequence from the Siberia Ridge field, a tight gas sand reservoir located in Wyoming, as an example. The results give responses in the frequency domain containing the effect of scattering and intrinsic attenuation. By comparing total attenuation with scattering attenuation, we observe the differences associated with the flow units. Flow units can be identified because the increase in attenuation is due to the interaction of fluid flow with the rock matrix. The modeling results show scattering effects of shales and coals and demonstrate that coals control the scattering attenuation. The elastic attenuation is shown at all frequencies and the fluid flow effects are observed in the sonic and crosswell frequency ranges. This model study suggests that low frequency measurements such as 3D seismic would not be able to map fluid flow. Only borehole related seismic measurements have the potential to map fluid flow effects in tight gas sands at the Siberia Ridge field.

2. Introduction

Accurate reservoir description and simulation are dependent on measures of properties such as porosity, permeability, fluid viscosity, and fluid saturation. Porosity is routinely available from wireline log data, which, in conjunction with 3-D seismic data, can be used to generate excellent reservoir porosity models. Until recently, cores were the only source of permeability data measured on a small enough scale to provide critical reservoir heterogeneity data. Cores are almost useless for permeability estimates in fractured formations; if a fracture is missed,

only the matrix permeability is estimated. If a fracture, especially a larger one, is penetrating the core, the chance is good that the core will not be intact and that permeability will not be measurable.

Permeability can also be derived from core-based permeability-porosity cross-plots, but such an approach is flawed, as the porosity-permeability correlations are often poor and core data may be sparse and expensive to obtain. At present, nuclear magnetic resonance (NMR) measurements calibrated with core data are often used for permeability estimations in reservoirs. Also, permeability estimates are made using core-calibrated well log data from a variety of tools (Tang et al., 1998).

Acoustic measurements based on frequency-dependent Stoneley wave attenuation and dispersion have been used to extract information about formation permeability from measured fluid mobility. Stoneley permeability measurements work well in fractured rock (Tang et al., 1997, 1991). In this case, attenuation measurements are affected by the heterogeneity and viscoelasticity of the rock, rather than fluid flow interactions alone (or intrinsic properties of the reservoir such as permeability and porosity). To use attenuation and dispersion measurements to predict flow properties at field scales, the effects of scattering must be understood so velocity measurements can be corrected for such effects.

In natural rocks, variations of the local permeability, density, and compressibility cause impedance variations, leading to poroelastic scattering. The same variability causes local fluid flow on the length scale of the rock. Both effects cause dispersion and attenuation of the propagating wave.

To properly model flow units in a reservoir we use the theory of poroelasticity. The theory assumes that when a P-wave propagates through a porous medium it forces the pore spaces to alternately expand and contract. This local change in pore volume and pore pressure may cause the saturating fluid to flow from contracting to expanding pores. The internal motion of a viscous fluid thus extracts energy from the passing wave and also affects the rigidity of the porous volume as a whole, which in turn alters the wave velocity. Biot (1956, 1962) presented a theory describing the frequency dependent behavior of attenuation and dispersion for fluid motion parallel to the direction of wave propagation by assuming homogeneity on the scale of the probing wavelength. Alternatively, the squirt-flow mechanism accounts for fluid motion perpendicular to the direction of wave propagation and it only appears with introduction of the squirt-flow length in the porous rock.

One theory describing a squirt-flow mechanism on the pore scale was developed by Dvorkin and Nur (1993), who presented a unified analysis of the Biot and squirt-flow (BISQ) mechanism. The BISQ mechanism relies on a heuristic parameter (the squirt-flow length) and may not be applicable to all rock types. Nevertheless, the BISQ mechanism has been demonstrated to be quantitatively consistent with measurements of attenuation in sandstone samples as a function of permeability and saturation. The BISQ theory was extended by Parra (1997) to include permeability anisotropy with a vertical axis of symmetry. This model was applied to crosswell data (in the frequency range of 400 to 2000 Hz) from the Gypsy test site to analyze

whether dispersion is sensitive to vertical permeability. Parra (2000) further modified the BISQ theory to include azimuthal anisotropy with a horizontal axis of symmetry. The theory was tested using a crosswell data set acquired at the Buckhorn test site in Illinois, and rock/fluid properties from the Kankakee Limestone Formation. The results of the crosswell seismic experiments and processing are given in Parra (1995).

While fluid motion may dominate attenuation for wave propagation in porous media over certain frequencies, it is certainly not the only mechanism that reduces wave amplitude. Scattering, in the form of reflections from variations in the medium's impedance, has long been recognized as a significant contributor to attenuation. Gurevich et al. (1997) provided a study considering the combined effects of scattering and Biot flow in layered media. Interlayer flow (a squirt-type local flow on the length scale of the layering) dominates at the lowest frequencies for reservoir rock in the seismic frequency range from 10-100 Hz. At frequencies in the kHz range encountered by borehole acoustic data, scattering caused by the poroelastic impedance contrasts in the layered medium is dominant. The Biot global flow dominates in high frequencies and in high permeability zones. The work of Gurevich et al. (1997) demonstrates that flow-based and scattering-based attenuation can be treated independently and added to produce the total attenuation. Only recently, Hackert and Parra (2000) modeled a finely layered sedimentary sequence from Buena Vista Hills, California, to investigate the relative importance of scattering and fluid flow attenuation.

Here, we present an application of this model to demonstrate whether acoustic/seismic measurement techniques can be effectively used to map flow units in a reservoir. To properly predict attributes at acoustic and seismic frequencies requires a good understanding of the lithology and poroelastic reservoir properties at the borehole scale.

In this paper we present the theoretical solution of a plane wave incident to a layered isotropic poroelastic medium with a horizontal axis of symmetry. The complete theoretical development is given in Appendix A, beginning on pg. 100. We also apply the theory to a real model from the Siberia Ridge tight gas reservoir.

3. Geology and Petrophysics

The Siberia Ridge Field is a stratigraphically trapped gas accumulation on the north flank of the Wamsutter Arch in the Greater Green River Basin, Wyoming. Gas production is from the Almond and overlying Lewis reservoirs. A detailed study of the Almond Formation and methods to aid the exploration of tight gas sandstones is given in a report written by Sturm et al. (2000).

Sturm et al. described the Almond Formation as alternating sandstones, shales, and coals of Late Cretaceous age. Within the field area, the Almond can be stratigraphically divided into an Upper Almond marine sequence (10,575 to 10,650 feet at the Amoco Siberia Ridge 5-2 well) and a brackish to non-marine Main Almond sequence (below 10,650 feet). The 5-2 well was drilled at a 45° angle through the Almond Formation. The Main Almond is approximately 450 feet thick and the Upper Almond is 30 to 50 feet thick. Coals occur only in the Main Almond and

are the source of the gas. Most of the gas production, however, is from the Upper Almond, which is a transgressive marine sequence consisting of shore face to foreshore deposits. The sequence is predominantly a laterally continuous barrier bar sandstone (the Almond Bar) with a classic coarsening upward profile. It is bounded by shales. The barrier bar sandstone is 50 feet thick on the log and has a true vertical thickness of approximately 30 feet. Borehole data indicate that fractures in the Siberia Ridge Field are aligned regional extension fractures.

Siberia Ridge fracture density ranges up to 5.5 fractures per foot, and fracture density increases markedly with depth in the Siberia Ridge wells. This increase coincides with a change in lithology from mostly marine sands and shales to a more heterogeneous mixture of sands, muds and coals of the coastal plain. The low porosity and matrix permeability suggest that the source of the produced water causing problems in this field is from high permeability fractures. Natural fractures, as determined by image logs and anisotropy based on cross dipole analysis, distinctly increase in the lower Main Almond and Ericsson sands. In this reservoir, the flow units are fractured tight gas sands.

4. Method

a. Model to simulate a fracture system

To simulate fractured zones containing fluids we use a poroelastic model characterized by the tensor permeability and the squirt-flow tensor. We simulate a system of aligned fractures by defining the horizontal x-axis as the axis of symmetry. Figure 43 shows a 3D view of the fracture medium with the horizontal axis, x, illustrating an arbitrary plane characterized by an azimuthal angle measured from the horizontal x-axis, and an incident angle measured from the z-axis. In the plane of the fractures, yz, the permeability is large, and in the direction perpendicular to the fractures, x, permeability is low, as is that of the tight sand. The model assumes that the principal axis of the elastic stiffness tensor is aligned with the permeability tensor and squirt-flow tensor axes. To simulate the fracture system, we consider two scales: (1) squirt-flow length on the order of centimeters to represent fluid flow in fractures, and (2) squirt-flow length less than or equal to 1 mm to represent grain scales. The concept of using two squirt-flow lengths to simulate attenuation associated with fluid transport properties in a partially saturated porous medium was introduced by Akbar et al. 1994, who considered wave-induced squirt fluid flow at two scales: (1) local microscopic flow at the smallest scale of saturation heterogeneity, and (2) macroscopic flow at a larger scale of fluid-saturated and dry patches. They observed two peaks of acoustic wave attenuation – one at low frequency (caused by macroscopic squirt-flow) and another at higher frequency (caused by microscopic squirt- flow). In the model study described below, the macroscopic squirt-flow (in the yz-plane) represents fluid flow within the fracture plane. To be applicable for a system of fractures based on macroscopic squirt-flow, nonuniform fluid distribution within a fracture plane is required – an assumption that appears reasonable.

b. *Model to simulate a layered isotropic poroelastic medium with azimuthal anisotropy*

To simulate the seismic response of a shale-sand sequence containing vertical fractures, we present in Appendix A the solution of a plane wave incident to a layered poroelastic transversely isotropic medium having a horizontal x-axis of symmetry. The solution is aimed at simulating azimuthal anisotropy caused by vertical fractures in the layers. Fluid flow in the fractures is characterized by permeability and squirt flow tensors, as addressed in the previous section. Each layer has its own rock and fluid properties as well its own degree of anisotropy. Therefore, the complete seismic response is formed by scattering associated with multiple layer boundaries, fracture-induced anisotropy due to vertical fractures, and fluid flow in fracture-induced anisotropy.

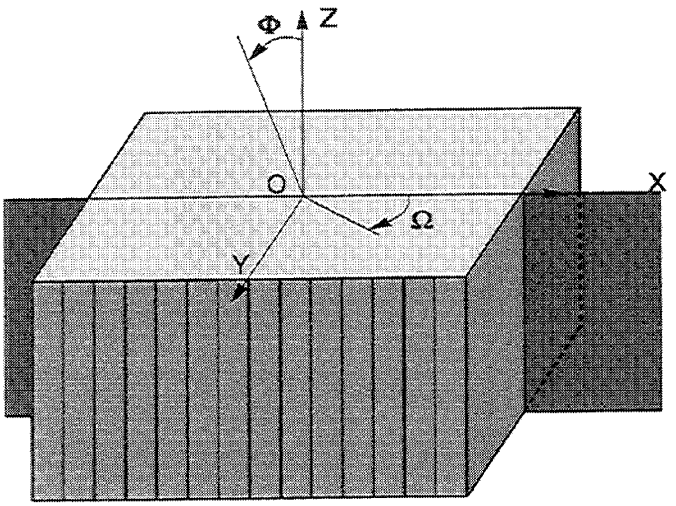

Figure 43. Three-dimensional view of the fracture system, illustrating the orientation of the azimuthal angle and the angle of propagation relative to the Cartesian system of coordinates (x,y,z).

c. *Model limitations*

The theory used to calculate attenuation curves is based on fracture-induced anisotropy and fluid flow in fracture-induced anisotropy (a concept described in Appendix A). As previously noted, fracture-induced anisotropy is represented by the tensor of stiffness constants, and fluid flow in fractures is represented by both the permeability and squirt-flow tensors. Scattering effects associated with fracture lengths, fracture apertures, fracture orientations, and multiple fractures cannot be modeled with the plane wave layered earth solution given in Appendix A. The finite difference modeling scheme or a boundary integral equation approach is more suitable to model specific fracture geometries or a multiple fracture system.

5. Data Example: Modeling Results

We first created a model of the Almond Bar sandstone using core and log data from the 5-2 well in the Siberia Ridge field. Core data provided density, permeability, and porosity, while acoustic logs provided compressional and shear velocities. The squirt-flow lengths for the tight sand matrix were derived from thin-section analysis. Fracture permeabilities were estimated from apertures extracted from microresistivity imaging logs (Sturm et al., 2000). We chose a fracture permeability of 50 millidarcies, which is approximately the average vertical permeability of the Almond formation intercepted by well number 5-2 at Siberia Ridge (Sturm et al., 2000). The model treats the sandstone as a horizontally transverse isotropic (HTI) homogenized medium, with permeability and stiffness anisotropy. Individual fractures are not modeled. Because elastic wave attenuation is sensitive to the presence of fluids in fractures, from this model we computed poroelastic attenuation for a plane wave traveling at different azimuths relative to the system of vertical fractures in the tight sands. The sandstone model parameters are given in Table 7.

Figure 44 shows attenuation maxima at low and high frequencies for a squirt-flow length of 0.2 mm in the tight sands and a system of fractures having a squirt-flow length of 5 cm. Attenuation peaks are observed at 1000 Hz (in the frequency range of 10 to 1500 Hz), at azimuths of 0 (normal to the system of fractures) and 30 degrees. These observations suggest that squeezing fluid in and out of the fractures requires acoustic or seismic energy in the range of about 150-1000 Hz (e.g., crosswell, reverse VSP, and long space logging).

In Figure 44, attenuation maxima are also observed at higher frequencies at azimuths of 60 and 90 degrees (parallel to the fracture plane). For these azimuths, elastic waves excite fluid motion in the porous matrix, and attenuation is controlled by fluid flow in tight sands (or microscopic squirt-flow). Figure 45 illustrates attenuation curves for the model parameters given in Table 7. In this example we increase the squirt-flow length to 7 cm, and the attenuation peaks shift to the lower frequency range. The attenuation peaks computed at azimuths of 0 and 30 degrees are observed at about 600 Hz. Since the microscopic squirt-flow in the tight sands did not change, the locations of the corresponding attenuation peaks at higher frequencies remain the same as those in Figure 43 at azimuths of 60 and 90 degrees. Increasing the macroscopic squirt-flow length shifts the attenuation peak to lower frequencies, because to move fluid in and out of large, thin fractures requires wavelengths comparable to those associated with fracture lengths. On the other hand, when the macroscopic squirt-flow length is decreased, the fractures in the zy-plane eventually disappear.

Table 7. Rock Physics and Fluid Property Parameters for a Sandstone Unit

Parameters	Formation Values
P-velocity (m/s)	4200
Bulk Density (g/cc)	2.48
Horizontal Permeability (md)	0.01
Vertical Permeability (md)	50
Porosity (dec)	0.084
Fluid Velocity (m/s)	1500
Fluid Viscosity (Poise)	0.01
Fluid Density (g/cm^3)	1

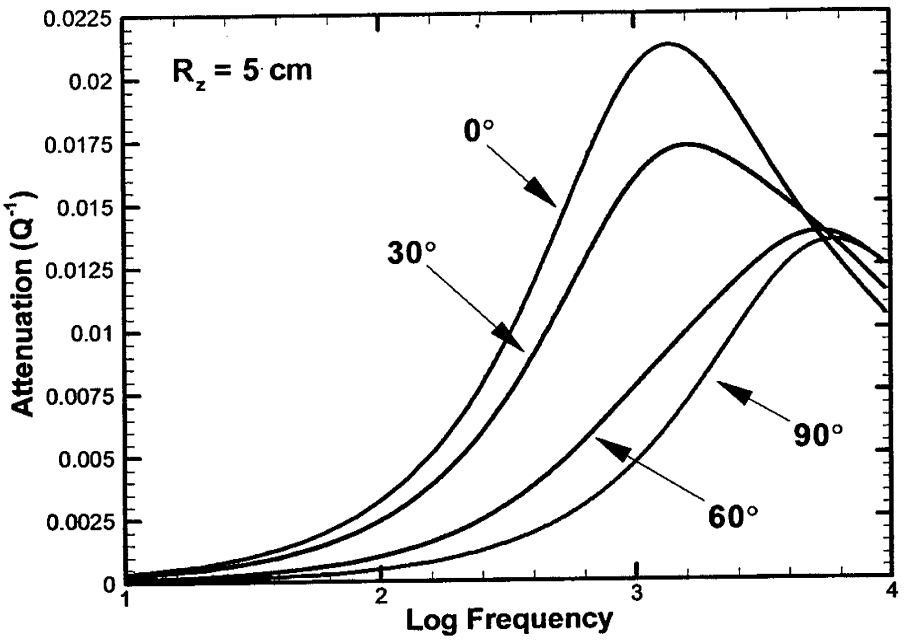

Figure 44. The effect of frequency and azimuths for a global squirt-flow length = 5 cm (representing fluid flow in cracks) and a local squirt-flow length = 0.2 mm (representing fluid flow in tight sands).

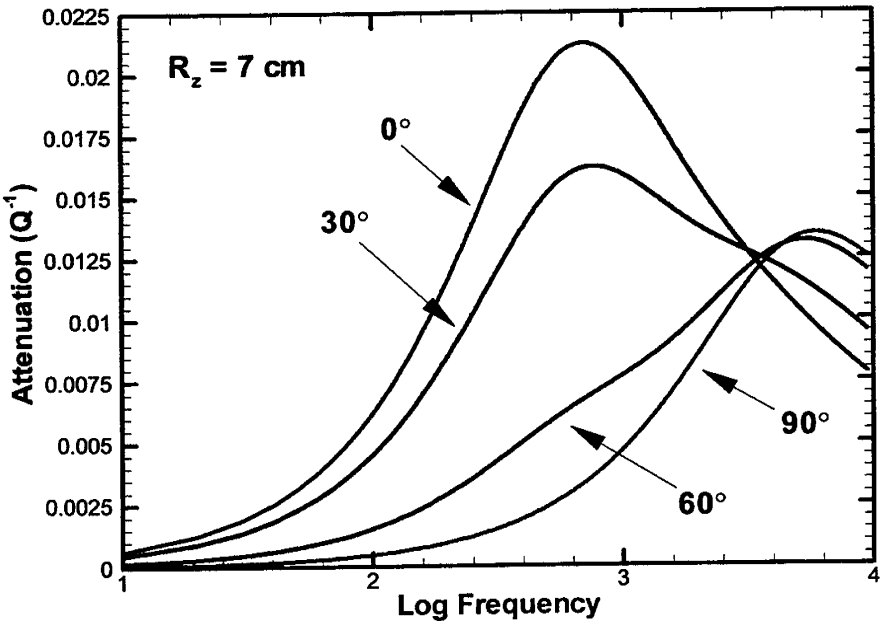

Figure 45. The effect of frequency and azimuths for a global squirt-flow length = 7 cm (representing fluid flow in cracks) and a local squirt-flow length = 0.2 mm (representing fluid flow in tight sands).

This modeling example shows that squirt-flow lengths between 5 and 7 cm produce realistic attenuation in the range of acoustic/seismic measurements, with attenuation peaks corresponding to quality factors of about 40. These results show that attenuation can be strongly affected by wave-induced squirt-flow in the plane of the fracture. We also observe in Figures 44 and 45 that attenuation in the tight sands due to microscopic squirt-flow is associated with a Q of 80 at high frequencies. Fluid flow in tight sands is not causing attenuation as strong as that in fractured formations with porosities on the order of 20 percent and permeability on the order of 10 md, where quality factors in the range of 20-40 (Hackert et al., 2000) have been observed. In this environment, the results predict that as long as there is fluid flow in the rock matrix towards the fractures, the fluid motion will attenuate the acoustic/seismic waves. In the event that there is no fracture-induced fluid flow, we cannot expect high attenuation for waves traveling perpendicular to the fracture system. In this case the Biot mechanism will control any fluid interaction between the pore fluid and the rock matrix in the direction parallel to P-wave propagation. Since the permeability in the tight sands is about 0.01 md, the Biot flow will be practically zero in the direction normal to the fracture plane.

Next, we study in more detail the scattering attenuation associated with the layered sequence of sands, shales, and coals and compare it to the poroelastic attenuation. Model responses are calculated for different azimuths and angles of incidence, and over a broad frequency range. The sequence and thickness of our layered model is determined by the lithology as interpreted from the well logs. Sandstone layers have the properties listed in Table 7. Shale and coal layers have properties derived from the well logs, and these are listed in Table 8. An interpretation of Sturm et al. (2000) indicates that only the sandstones have open fractures, and therefore the shale and coal layers are assumed to be isotropic in the model. In fact, core and FMI observations show that open fractures occur in sandstones, whereas healed fractures occur in shales and coals. Close fractures play an insignificant role in total fracturing in every interval of Almond Formation. Based on this information, we construct a detailed model that consists of a stack of 114 discrete layers representing the Almond Formation to the bottom of the 5-2 well. These layers have a true vertical thickness of 358 feet.

Table 8. Rock Physical Properties for Layer Model

Property	SANDSTONE	SHALE	COAL
Vp	4.1/4.4 K m/s(*)	3.9 Km/s	2.7 Km/s
rho	2.61 g/cc	2.5 g/cc	1.4 g/cc
SGM	37 Gpa	26.8 Gpa	13.3 Gpa
porosity	8%	2%	1%
perm	10 μd/50 md(*)	0.1 μd	1 μd
squirt-flow length	0.2/70 mm(*)	0.5 mm	0.2 mm
tortuosity	3	3	3

(*) The first value corresponds to the rock property in the direction perpendicular to the fracture system. The second value is the property parallel to the fracture system.

The theoretical solution given in Appendix A allows us to extract attenuation information by measuring the transmission coefficient as a function of frequency for a plane wave incident on the top of the stack with arbitrary angle of incidence and azimuth. The plane wave has two modes of operation: elastic, in which the attenuation is solely due to reflections and scattering among the different layers; and poroelastic, in which the amplitude is also reduced by the wave-induced fluid motion (Biot, squirt, and interlayer flow). The transmission coefficient is converted to a Q value through the frequency and distance traveled. For simplicity, the distance traveled is taken to be the vertical thickness divided by the cosine of the incident angle. We have observed that this approach is acceptable, except that for angles closer to horizontal, refraction can significantly change the path length. Measured attenuation for the 75-degree incidence data below (and to a lesser extent, the 45-degree incidence data) is probably too low because the path length is overestimated. In fact, for nearly horizontal propagation, critical refraction and evanescent waves make the path difficult to define. For a given angle of incidence, however, the path length bias is fairly constant, regardless of azimuth angle or elastic or poroelastic operation.

Incidence angles are measured from vertical so that 75-degree incidence is near horizontal. Azimuth is measured relative to the fracture system, so 0-degree azimuth is normal to the fractures, while 90-degree azimuth is parallel to the fractures. Remember that incidence normal to the layers is also parallel to the vertical fractures, so that the largest squirt effect from the fractures will come at 0-degree azimuth and near horizontal angles.

In the modeling method we also include a stochastic representation of the layer sequence. For example, Figure 46 shows the Q^{-1} derived from the normal incidence elastic model (including coal layers) and a prediction of Q^{-1} based on stochastic medium theory (Parra et al., 1999). Agreement is not so good between the deterministic (black line) and stochastic (red line) responses, because the strong impedance contrast between the coals and the other layers violates the assumed Gaussian probability distribution. Replacing the coals by sand and shale layers yields an elastic Q^{-1} in good agreement with stochastic medium theory (see Figure 47). Note too, that when coals are present, modeled attenuation is higher by roughly an order of magnitude. The stochastic model that assumes a Gaussian probability distribution underpredicts the attenuation when coals are present. In Figures 46 and 47 attenuation was predicted in the frequency range of 0.01-10 kHz, to evaluate the applicability of acoustic/seismic techniques for predicting flow units. The results demonstrate that scattering caused by the high impedance contrast between the coal beds and the adjacent clastics is the main cause of high attenuation in the Almond Formation.

In Figure 48, we present the elastic and poroelastic attenuation responses for the same coal-sand-shale layer model used in the example of Figure 46, again considering vertical wave propagation. Elastic attenuation is represented by a black line and poroelastic attenuation associated with fluid flow in fracture-induced anisotropy is represented by a red line. The figure shows that poroelastic attenuation is about the same as elastic attenuation for seismic and crosswell seismic frequencies. On the other hand, poroelastic attenuation is greater than elastic attenuation for frequencies in the borehole acoustic range (i.e., greater than about 1500 Hz). This is consistent with the predicted poroelastic response from the sand layers, as shown in Figure 44. Vertical wave

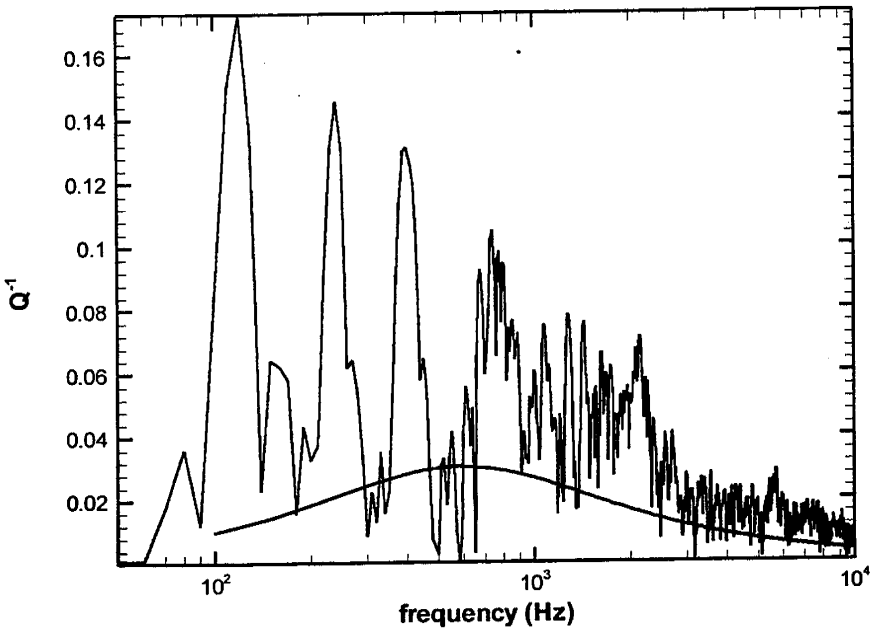

Figure 46. Normal incidence. Black line is elastic, red line is stochastic medium prediction. This is a full model with coal layers. The coals cause a large increase in attenuation, but are too sparse and too different to have a good match from stochastic theory.

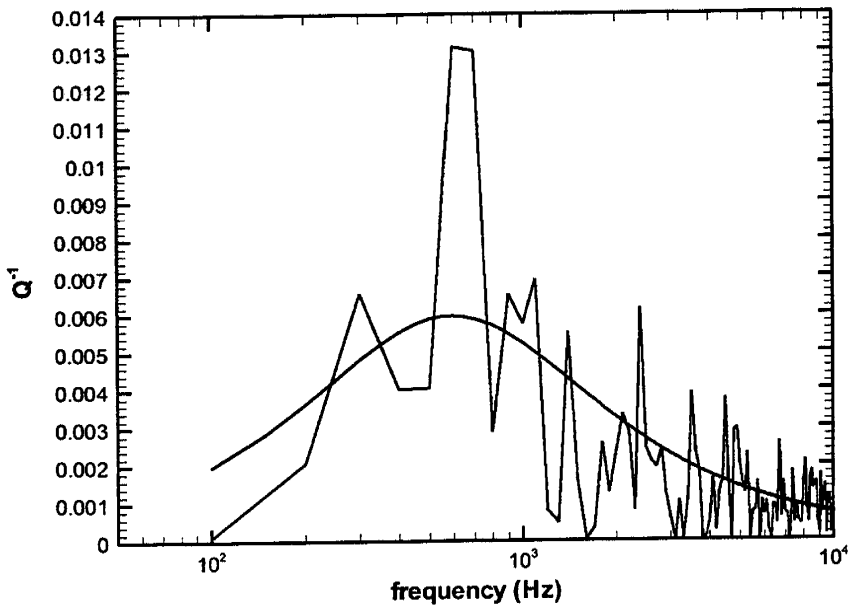

Figure 47. Normal incidence. Black line is elastic, red line is stochastic medium prediction. This is a modified model without coal layers. This model (using sand and shale only) shows a good match with a stochastic medium theory result.

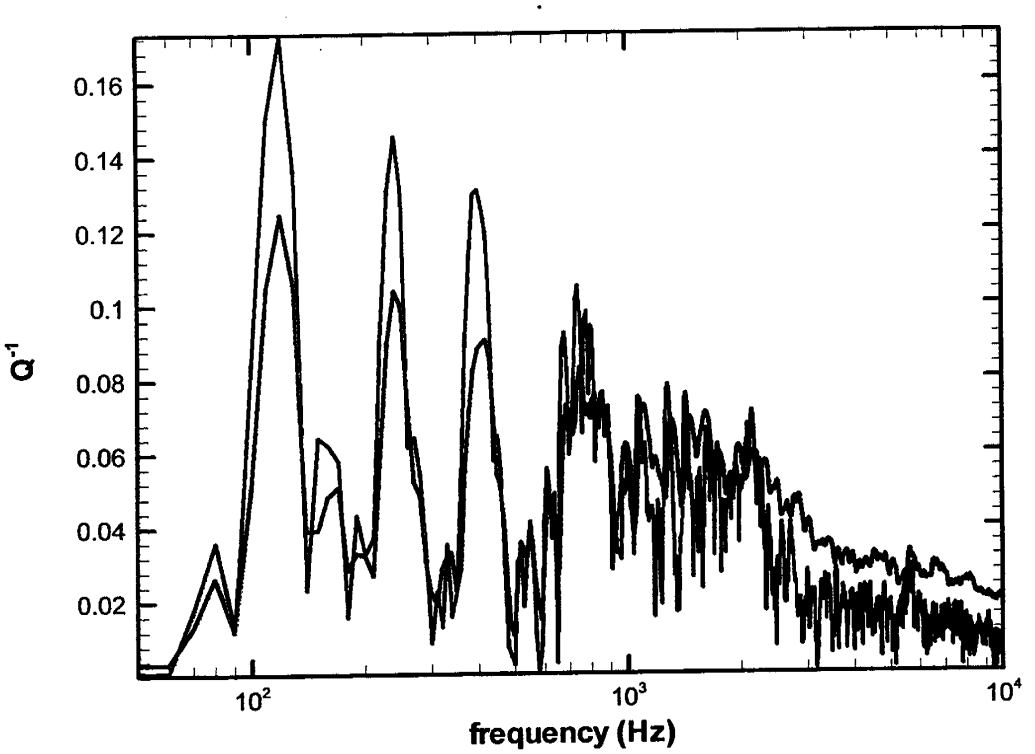

Figure 48. Normal incidence. Black line is elastic only, red line is poroelastic. Vertical incidence is parallel to fractures, so the only real effect is at high frequencies.

propagation is parallel to the fracture plane and so corresponds to the 90° response. Thus, it is only the high frequencies that show an observable poroelastic attenuation response for vertical wave propagation.

In the next series of figures we analyze the effects of angle of incidence and azimuth on the attenuation response. We analyze incidence angles of 45° and 75° for azimuths of 0° and 90°. Figures 49 and 50 show the attenuation response of the same layered model used in the previous example in the presence of a plane wave incident at 45° at azimuths of 0° and 90°, respectively. In both cases, elastic (black line) and poroelastic (red line) responses are presented. In the direction normal to the fracture system, the poroelastic response is greater than the elastic response in the frequency range of 200 to 700 Hz. This was also seen in Figure 45, where the poroelastic response in the sand for propagation normal to the fractures (0° azimuth) peaks in the frequency range near 600 Hz. In the direction of the fracture system (90° azimuth), the elastic and poroelastic attenuation responses are similar.

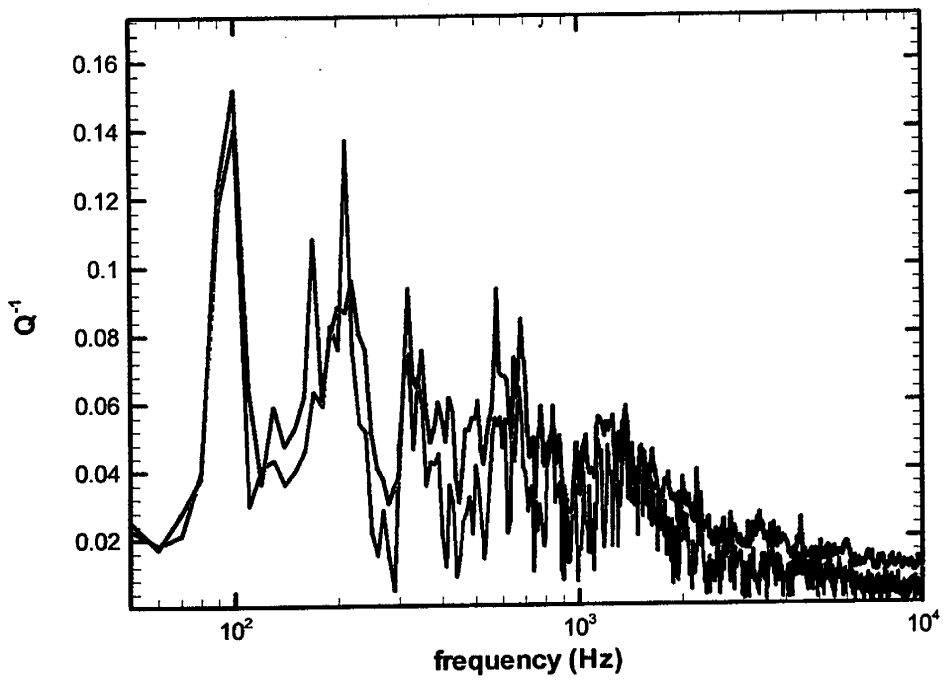

Figure 49. 45 degree incidence, 0 degree azimuth. Black line is elastic only, red line is poroelastic.

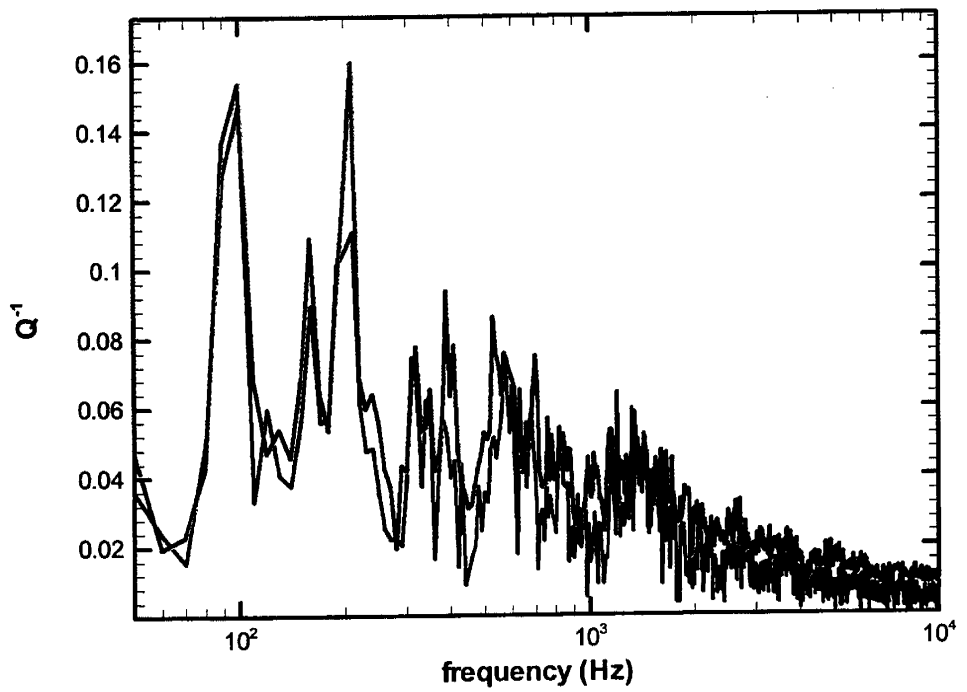

Figure 50. 45 degree incidence, 90 degree azimuth. Black line is elastic only, red line is poroelastic.

There also appears to be more elastic attenuation in the direction parallel to the fracture system than in the direction perpendicular to the fracture system for angles of incidence away from vertical. This is demonstrated in Figures 51 and 52, where the angle of incidence is increased to 75°. Since we are not modeling individual fractures, but only velocity and permeability anisotropy in otherwise homogeneous layers, this effect arises from the fracture-induced velocity anisotropy in the sandstones. Specifically, the sandstone layers have faster velocities in the parallel direction than in the perpendicular direction. As the angle of incidence moves away from vertical, this means that the sand-shale and sand-coal reflection coefficients are higher for waves propagating parallel to the fracture system than perpendicular to it. The higher reflection coefficients lead to increased scattering, and thus more elastic attenuation. Other models incorporating discrete fractures may show an opposite effect, particularly at high frequencies where individual fractures can act as scattering elements. Regardless of the fracture model used, poroelastic attenuation is always highest for waves traveling perpendicular to the fracture system. In this configuration, passing compressional waves have the greatest opportunity to induce squirt-flows along the fracture planes.

This modeling analysis suggests that flow units characterized at the borehole scale, based on standard logs and monopole/dipole data, can be used to construct poroelastic models to evaluate whether acoustic/seismic methods will provide information on fluid movement in the reservoir. The main objective of this work is demonstrate a model to predict attenuation effects that can result from layering (scattering) as well as intrinsic effects that can be associated with fluid flow effects in the reservoir region surrounding a well. We chose a poroelastic model based on the Biot and squirt-flow mechanism because it has the versatility to simulate the effect of fluid flow in fracture-induced anisotropy (i.e., flow units and fluid flow in the vertical and horizontal directions are defined by the permeability and squirt- flow tensors). Understanding these concepts will help the reservoir geophysicist plan crosswell seismic surveys and determine whether high resolution seismic attributes will capture fluid-flow effects. Therefore, before conducting seismic surveys, we suggest applying this model-based interpretation scheme to determine whether high resolution VSP and/or crosswell seismic measurements will provide the information required to map fluid flow and/or geological structures.

6. Conclusions

The modeling results indicate that fracture-induced anisotropy in tight gas sands may be detected using seismic methods in the range of 150 to 1000 Hz at azimuths between 15-30° at angles of incidence near 90°. Also, the results suggest that attenuation is sensitive to fluid flow in the tight sands above 1000 Hz at azimuths greater than 60°. These results indicate that any attempt to map fracture-dominated flow in low permeability and low porosity environments will require multiple frequency measurements in the range of sonic logs or high frequency VSP measurements. To separate intrinsic effects from scattering effects associated with the shale-sand-coal layer sequence in the Siberia Ridge field will require measurements at a minimum of two frequencies (e.g., sonic and VSP).

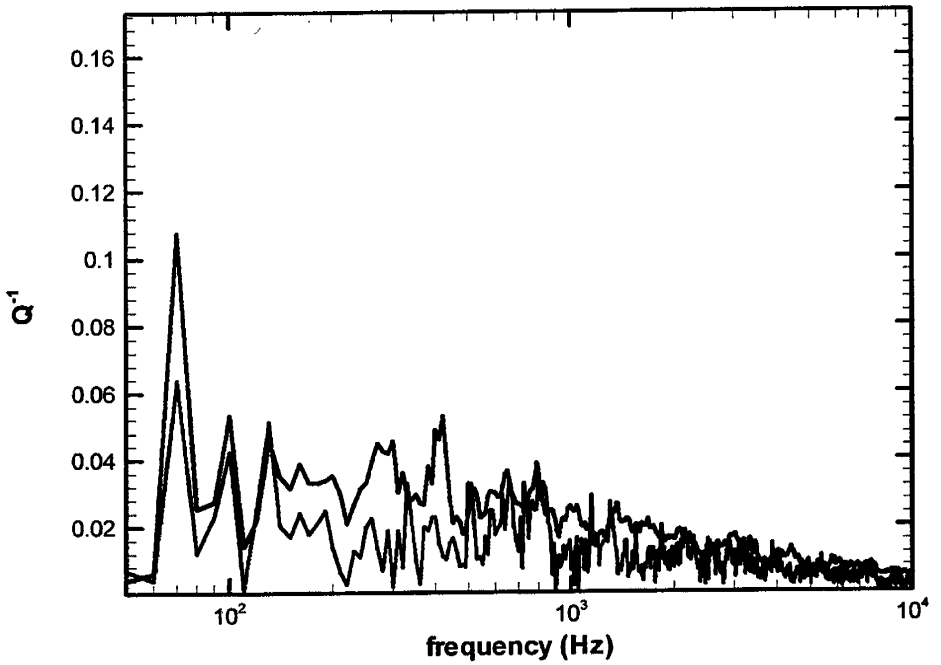

Figure 51. 75 degree incidence, 0 degree azimuth. Black line is elastic only, red line is poroelastic.

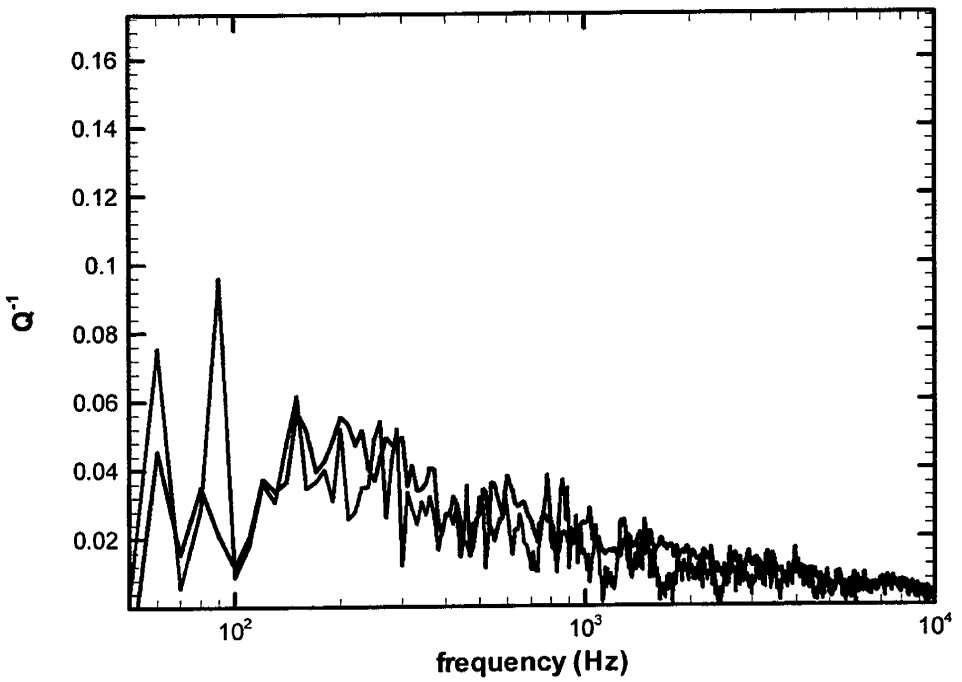

Figure 52. 75 degree incidence, 90 degree azimuth. Black line is elastic only, red line is poroelastic.

The analysis results provide a modeling approach based on borehole data to predict whether flow units can be detected at acoustic and seismic scales. The flow units are constructed using core and borehole data. The model based on these two scales predicts attenuation responses at the borehole and crosswell scales and can be applied to other reservoirs with different petrophysical characteristics and reservoir parameters. In this application, permeability and porosity are derived from NMR well logs calibrated with core data.

The final results of the model provide insight into planning crosswell or high resolution VSP for mapping flow units. In this particular reservoir, the measurements were sensitive to fluid flow effects in the frequency range of borehole related surveys. Any interwell or VSP system that cannot transmit energy in the frequency range of 500-2000 Hz will not be able to capture fluid flow in fracture-induced anisotropy. However, this modeling approach does not prevent the capture of fracture-induced anisotropy associated with large fracture zones and faults that may be presented in the region using 3D seismic surveys.

References

Akbar, N., Mavko, G., Nur, A., and Dvorkin, J. (1994) Seismic signatures of reservoir transport properties and pore fluid distribution: *Geophysics*, v. 59, p. 1222-1236.

Biot, M.A. (1956) Theory of propagation of elastic waves in fluid-saturated porous solid: I. Low-frequency range, II. Higher frequency range: *Journal of the Acoustical Society of America*, v. 28, p. 168-191.

Biot, M.A. (1962) Generalized theory of acoustic propagation in porous dissipative media: *The Journal of the Acoustical Society of America*, v. 34, p. 1254-1264.

Dvorkin, J., and Nur, A. (1993) Dynamic poroelasticity: a unified model with the squirt and the Biot mechanisms: *Geophysics*, v. 58, p. 523-533.

Gurevich, B., and Shoenberg, M. (1999) Interface conditions for Biot's equations of poroelasticity: *The Journal of the Acoustical Society of America*, v. 105, p. 2585-2589.

Gurevich, B., Zyrianov, V.B., and Lopatnikov, S.L. (1997) Seismic attenuation in finely layered porous rocks: Effects of fluid flow and scattering: *Geophysics*, v. 62, p. 3319-324.

Hackert, C. L., and Parra, J. O. (2000) Analysis of multiscale scattering and poroelastic attenuation in a real sedimentary rock sequence: *J. Acoust. Soc. Am.* 107, pp. 3028-3034.

Parra, J.O. (2000) Poroelastic model to relate seismic wave attenuation and dispersion to permeability anisotropy: *Geophysics*, v. 65, p. 1-9.

Parra, J.O. (1997) The transversely isotropic poroelastic wave equation including the Biot and the squirt mechanisms: Theory and application: *Geophysics*, v. 62, p. 309-318.

Parra, J.O. (1995) A feasibility study of high-resolution reverse VSP and interwell seismic methods for hydrocarbon reservoir characterization: *The Log Analyst*, v. 36, p. 64-81.

Parra, J. O. (1991) Analysis of elastic wave propagation in stratified fluid-filled porous media for interwell seismic applications: *The Journal of the Acoustical Society of America*, 90, 2557-2575.

Parra, J. O., and Xu, P.-C. (1994) Dispersion and attenuation of acoustic guided waves in layered fluid-filled porous media: *The Journal of the Acoustical Society of America*, 95, 91-98.

Parra, J.O., Collier, H.A., Datta-Gupta, A., Owen, T., Peddibhotla, S., Xu, P.-C., and Zook, B. (1997) Characterization of fractured reservoirs using static and dynamic data: from sonic and 3D seismic to permeability distribution: Report DOE/DC/91008 (DE96001284), National Petroleum Technology Office, Department of Energy, Tulsa, Oklahoma.

Parra, J.O., Hackert, C.L., Ababou, R., and Sablik, M.J. (1999) Dispersion and attenuation of acoustic waves in randomly heterogeneous media, *Journal of Applied Geophysics,* v. 42, p. 99-115.

Sturm, S. D., Evans, L.W., Keusch, B.F., and Clark, W. J. (2000) Multi-disciplinary analysis of tight gas sandstone reservoirs, Almond Formation, Siberia Ridge field, Greater Green River Basin: Gas Research Institute, Report GRI-00/0026, Chicago, Illinois.

Tang, X., Gelinsky,S., Chunduru, R., and Cheng, C.H. (1997) permeability from borehole acosutic logs: an overview with recent advance, 67th Ann. Internat. Mtg., Soc. Explr. Geophys., Expanded Abstracts, 274-277.

Tang, X.M., Cheng, C.H., and Toksoz, M.N. (1991) Dynamic permeability and borehole Stoneley waves: A simplified Biot-Rosenbaum model: *Journal of the Acoustical Society of America*, 90, 1632-1646.

Tang, X., Altumbay, M., and Shorey, D. (1998) Joint interpretation of formation permeability from wireline acoustic, NMR, and image log data, *39th SPWLA Annual Logging Symposium Transactions*, Paper KK.

B. Characterization of Fractured Low Q Zones at the Buena Vista Hills Reservoir

1. Summary

Attenuation of high-resolution interwell seismic and acoustic waves based on dispersion analysis relates to fluid flow effects in fractured and shale-sand sequence formations at the Buena Vista Hills reservoir, California. Fractured low Q zones in the Brown Shale and Antelope Shale reservoir intervals in the Monterrey Formation correlate with a system of fractures having permeabilities on the order of 2.5 to 5 md. Vertical fractures oriented at azimuths from 0-30 degrees were detected in the frequency range of 1-10 kHz. The use of a poroelastic model based on the Biot/squirt-flow (BISQ) mechanism is a reasonable approach to relate the low Q zones in the Brown Shale and Antelope Shale units with the presence of fractures. Since the Brown Shale does not have sands, it is an ideal formation in which to evaluate the response of a fracture system to attenuation. The BISQ mechanism, adapted to simulate fluid flow in fracture-induced anisotropy, provides flow properties parallel and perpendicular to the fractures in the siliceous shale formations. The model assumes that the principal axes of the stiffness constant tensor are aligned with the axes of the permeability tensor and the squirt-flow tensor. We simulate the system of fractures by considering: (1) squirt-flow length on the order of centimeters to represent fluid flow in fractures, and (2) squirt-flow length less than 1 mm to represent flow in low permeability shales. Two types of fractures at the site are joint-like tectonic fractures and sigmoidal vein fractures. Their fracture permeability of about 5 md and squirt-flow lengths between 1-2 cm predict a quality factor of about 20 that fits the observed Q in a Brown Shale zone. We found that fractures associated with squirt-flow lengths ≥

3 cm can be sensitive to horizontal attenuation for a frequency range of 120-1000 Hz. In addition, the horizontal quality factor derived from sonic and crosswell data is about 5 times less than the vertical quality factor associated with waves originating from the earth's surface. In this case, the vertical attenuation based on a multilayered poroelastic modeling scheme demonstrates that only high-resolution borehole-related measurements can be effective in mapping fracture density at the Buena Vista Hills reservoir.

2. Introduction

The Buena Vista Hills site is located 25 miles (40 km) southwest of Bakersfield, in the southern San Joaquin Valley of California (Figure 53). Chevron USA Production Company conducted a reservoir characterization program in the Antelope shale at the Buena Vista Hills field to establish the viability of CO_2 enhanced oil recovery. As a result of this work, a comprehensive report was produced, which includes the application of advanced reservoir techniques to characterize the Antilope Shale (Morea, 1999). In particular, the study focused on a new infill well (653Z) and the four 1950s wells that surround it (these well numbers are 553, 563, 554, and 564). These five wells, shown in Figure 54, were used for a CO_2 pilot flood program, with the new well serving as the injector. The shale-sand sequence at this field is characterized by layering that was resolved by core analysis. This sequence is considered finer than that resolvable by sonic logging. In some sections the layer thickness ranges from a fraction of a centimeter to tens of centimeters, while in others zone bed thicknesses can vary from centimeters to meters. These thin beds are associated with turbidite deposition and contribute to the apparent anisotropy in the sonic to seismic frequency range. This concept was the motivation to study the contribution of scattering attenuation associated with the laminated siliceous shale and the intrinsic attenuation associated with the sands on acoustic/seismic waves in the Antelope Shale Member by Parra et al. (1998) and Hackert et al. (2001). In that study a processing technique was devised to separate intrinsic properties from scattering effects associated with the laminated medium. As a result, the effective Q as a function of depth was obtained, and it represents energy losses of seismic waves propagating in the reservoir interwell region.

Buena Vista Hills consists of a northwest-southeast trending, doubly plunging anticline with two structural highs. The study area is located on the west high, which is called West Dome. The producing interval is a 1300-foot (396-meter) thick section of the Upper Miocene Monterrey Formation. Locally, the interval is referred to as the Antelope Shale, and is divided into three units: the Brown Shale (upper quarter), the Upper Antelope Shale (middle half), and the Lower Antelope Shale (lower quarter). Geochemical analysis of the produced oil suggests that most of the present production comes from the Brown and Upper Antelope shales.

Approximately 95 percent of the Antelope Shale consists of thin (1 to 5 cm), graded, clay-free, siliceous shale beds. Very thin (1 mm to 25 cm) clayey sand laminae and carbonates are intercalated with the siliceous shale. The cores of the new infill well, 653Z, contain 748 sand laminae; all but one are in the Upper Antelope Shale. The porosity averages 28 percent, but the formation permeability averages only 70 μd, mostly due to low permeability in the siliceous shale. The rock was deposited in a restricted basin as distal turbidite and hemipelagic siliceous beds.

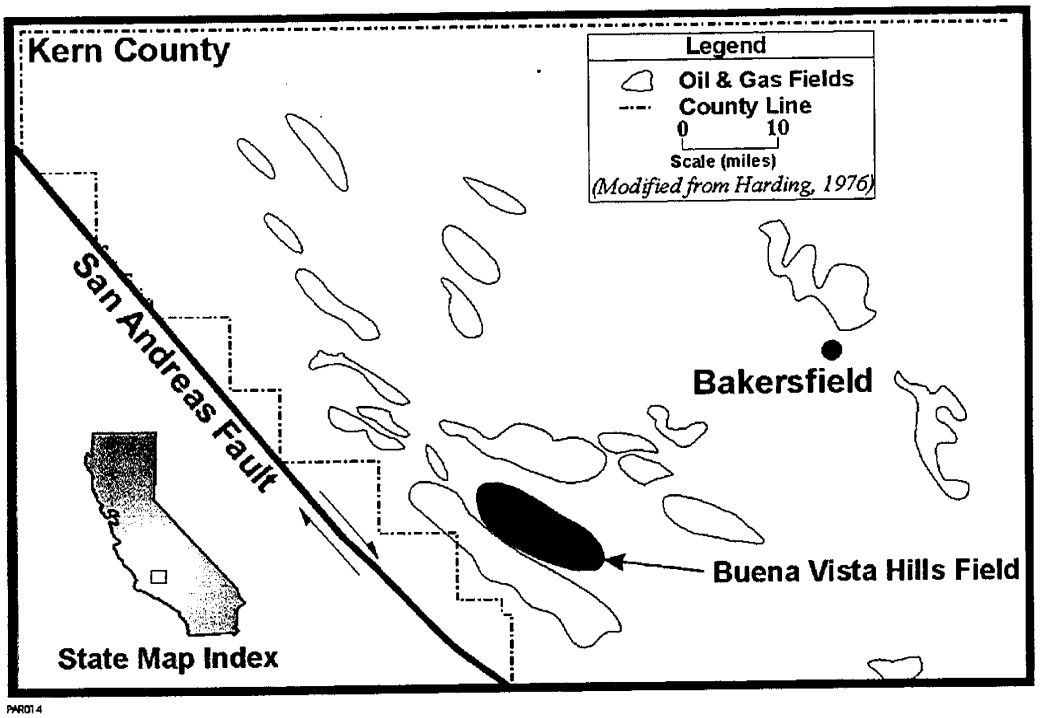

Figure 53. Map of Buena Vista Hills field near Bakersfield, California

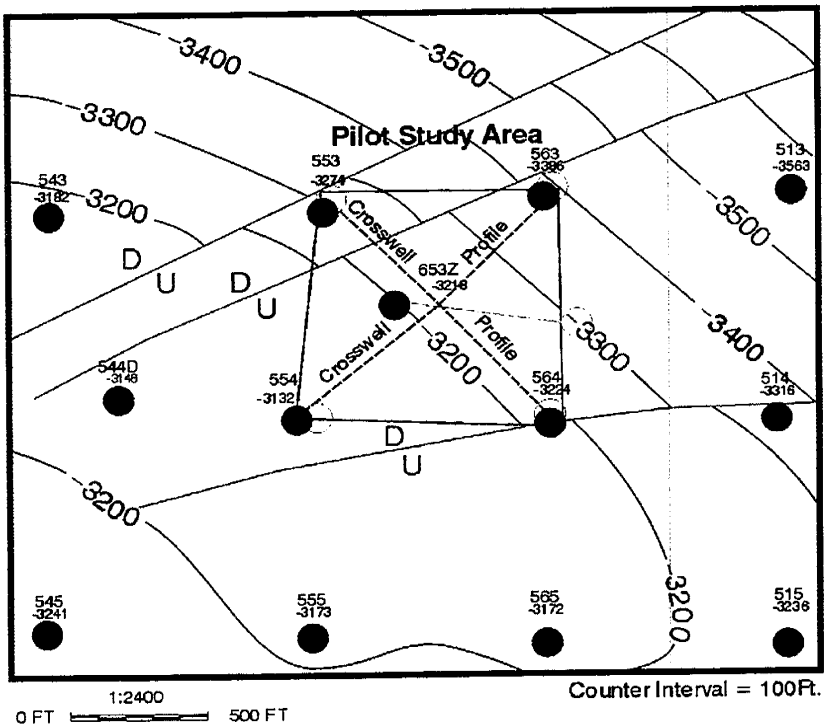

Figure 54. Structural map and well locations.

Mercury porosimetry tests indicate that at reservoir conditions only the sands are capable of producing oil (Morea, 1999). The sands, however, consist of only five percent of the rock, so fractures are contributing to hydrocarbon production. The extent of fracturing within the Antelope Shale and the significance of the fractures in fluid transport are subjects of debate. Pressure buildup analyses indicate that the fracture system is not pervasive. Cores and image logs, however, indicate that fractures are widespread in the borehole and occur on a variety of scales (Morea, 1999).The cores also reveal the presence of sigmoidal vein fractures at the interface of the siliceous shale host rock and the vein fill. However, the development of these fractures is restricted to the Brown Shale, as was indicated by Jacobs (1999), who studied how sigmoidal veins enhance the permeability of siliceous shale reservoirs.

The first objective of this paper is to explore the use of horizontal attenuation to characterize fractures at the Buena Vista Hills reservoir based on sonic and crosswell seismic data. A second objective is to understand the role of vertical attenuation in reservoir characterization to evaluate whether or not VSP or surface seismic measurements can be sensitive to fluid flow effects at the Buena Vista Hills field. The crosswell data set for the present analysis was recorded between the injector and the four producers wells. In each case, the source was placed in the producer well and the receiver in the injector well. Sources and receiver were at 5-foot (1.5-meter) intervals in the wells over a range of about 1500 ft. (457 m). Waveforms were recorded for more than 30,000 source-receiver combinations for each well pair. The resulting tomograms yielded compressional wave velocity information with 2-foot (61-centimeter) vertical resolution and approximately 5-foot (1.5-meter) horizontal resolution, depending on the specific profile (Guan et al., 1998). As an example, the tomogram profile between wells 653Z and 553 is shown in Figure 55. In addition, a Q profile was determined from velocity dispersion analyses based on sonic and crosswell seismic data in the region between 4000 and 4300 ft. (1220-1310 m) of infill well 653Z (Hackert et al. 2001). The profile exhibits two low quality factor anomalies: a shallow anomaly in the Brown Shale and a bottom anomaly in the Antelope Shale. Hackert et al. demonstrated that the low quality factor in the Antelope Shale is due in part to the presence of scattering/intrinsic attenuation and fluid flow effects in the sands.

To reach our objectives, we used petrophysics and the dispersion results from Hackert et al. (2001), together with a poroelastic model that relates P-wave attenuation to tensor permeability. The model is based on work done by Parra (1997, 2000), Dvorkin and Nur (1993), and Akbar et al. (1994). Akbar et al. considered wave-induced squirt fluid flow at two scales: (1) local microscopic flow at the smallest scale of saturation heterogeneity, and (2) macroscopic flow at the larger scale of fluid-saturated and dry patches. They observed two peaks of acoustic wave attenuation – one at low frequency (caused by macroscopic squirt-flow) and another at higher frequency (caused by local flow). We apply this concept to simulate fluid flow in fracture-induced anisotropy to demonstrate that fractures contribute to attenuation at the Buena Vista Hills reservoir, and to predict the fracture system characteristics. To address vertical attenuation, we use the plane wave solution of an arbitrary plane in a layered transversely isotropic poroelastic medium with x being the axis of symmetry. We briefly describe the solution in Appendix A, and we use it to analyze the effect on vertical attenuation of fluid flow in fractures and sands in the siliceous shale. We then simulate the responses based on a shale-sand layer sequence and a shale-shale fractured layer sequence.

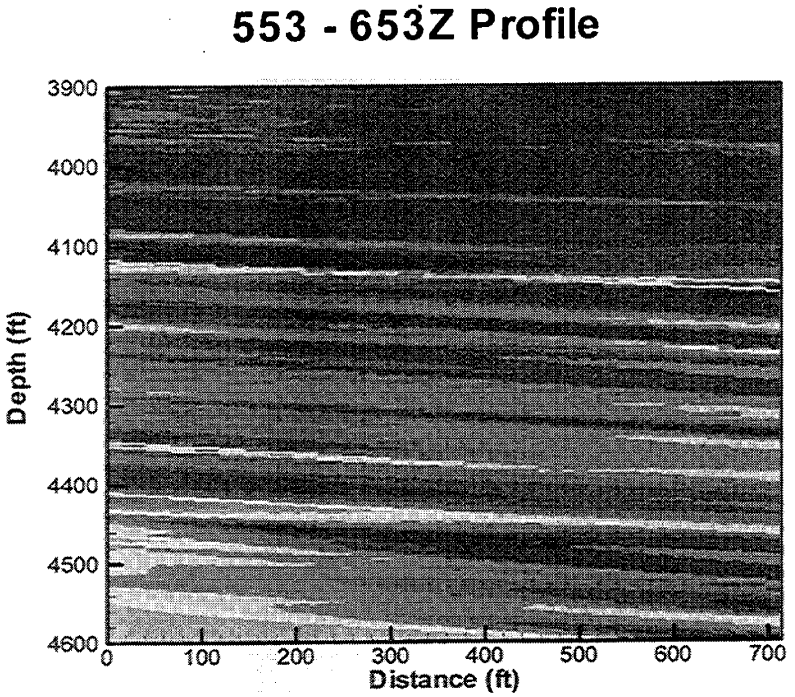

Figure 55. P-wave velocity image between wells 553-653Z at Buena Vista Hills

3. Data Analysis and Interpretation

a. Method

To simulate a fractured zone containing fluids, we adopt a poroelastic model characterized by the stiffness constant, squirt-flow, and permeability tensors. We simulate the fracture system by assuming that the horizontal x-axis is the axis of symmetry. Figure 56 shows a 3D view of the fracture medium with the horizontal axis, x, illustrating an arbitrary plane characterized by an azimuthal angle, Ω, measured from the horizontal x-axis, and an incident angle, Φ, measured from the z-axis. To relate attenuation and dispersion to the presence of fractures embedded in shales, we define the plane of the fractures (yz) as a plane of high permeability and the direction perpendicular to the fractures (x) as low permeability shales. In addition, the model assumes that the principal axes of the stiffness constant tensor are aligned with the permeability tensor and the squirt-flow tensor. To simulate the fracture system we consider two scales: (1) squirt-flow length on the order of centimeters to represent fluid flow in fractures, and (2) squirt-flow length less than or equal to 1 mm to represent flow in the unfractured rock (on the order of the grain scale). These two squirt-flow lengths are used to simulate attenuation associated with fluid transport properties in a porous medium, and they represent the fluid flow in fracture-induced anisotropy.

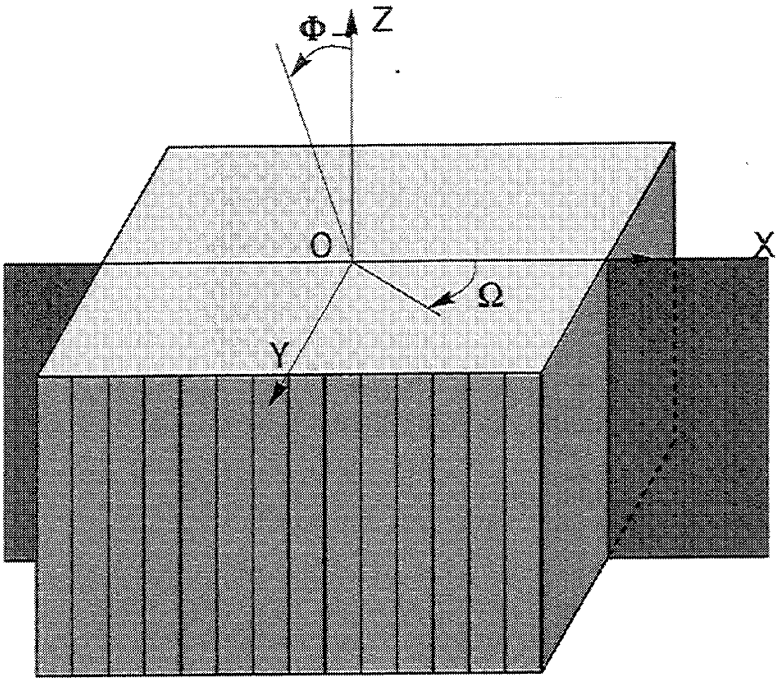

Figure 56. 3D view of fracture medium with axis of symmetry perpendicular to z-axis, showing orientation of azimuthal and propagation angles.

In the model study described below, the macroscopic squirt-flow (in the yz-plane) represents fluid flow within the fracture plane. The representation of a system of fractures based on macroscopic squirt-flow is practical, since we expect a nonuniform fluid distribution in a fracture plane. Because the stiffness constant in the yz-plane can be related to fracture density, the variation in fluid dynamic pressure due to fracture-related flow can simulate the effect of fluid-filled fractures on attenuation.

To address vertical attenuation effects at the Buena Vista Hills reservoir, we simulate the seismic response of a siliceous shale-sand sequence containing vertical fractures. To facilitate an understanding of the procedure involved in the calculations, we present the solution of a plane wave incident to a layered poroelastic transversely isotropic medium having the x-axis of symmetry (horizontal axis) in Appendix A. The solution is aimed at simulating azimuthal anisotropy caused by the presence of vertical fractures in the layers. The fluid flow in fractures is characterized by the permeability and squirt-flow tensors. Each layer has its own degree of anisotropy. Therefore, the complete seismic response is formed by the scattering associated with the multiple layer boundaries, the fracture-induced anisotropy due to vertical fractures, and the fluid flow in fracture-induced anisotropy.

b. Basis for fracture model

One impetus for this work is to find the causes of the low Q anomalies derived from velocity dispersion in a low permeability formation (Hackert et al., 2001). Another

motivating factor is the possible applicability of handling dispersion measurements to map fracture densities at distances away from the borehole. These ideas were developed after the discovery of fractures in cores (Morea, personal communication) at the location of the low quality factors. In the core analysis two types of fractures were observed. The first were sigmoidal vein fractures at the interface of the siliceous shale host rock and the vein fill. The development of these fractures is restricted to the Brown Shale. Based on permeability core measurements, Jacobs (1999) noted that sigmoidal veins enhance the permeability of siliceous shale reservoirs. Jacobs' results demonstrate that the increase in permeability is due to secondary fractures that form along vein margins and serve as conduits for hydrocarbon migration. He also observed that dissolution of the siliceous shale host rock causes porosity increases of up to 50 percent in local areas. Such an increase further enhances the permeability of sigmoidal vein fractures that are formed at the interface. These short, vertical, en echelon fractures are the most common fractures perpendicular to bedding in the Brown Shale, and they vary from 0.4 to 8 cm in length. The second fracture category is joint-like, tectonic fractures with nearly vertical dips and heights averaging 0.44 ft. Fracture densities range from 0 to 12 fractures per 20-foot interval, with the highest density occurring in the Antelope Shale. Large fractures, microfaults, and faults with an attitude perpendicular to bedding are scattered throughout the entire cored interval. This is reliable information with regard to the presence of open fractures at the core scale in the formation intercepted by the well.

Hackert et al. (2001) demonstrated by dispersion analysis that the intrinsic losses in the Antelope Shale were due to intrinsic effects associated with fluid flow in the sand beds, and that the Brown Shale is characterized by the effective Q log that represents intrinsic losses in the laminated diatomaceous shale. Since there are no sands in the Brown Shale, there is a high probability that the upper low effective Q is caused by the presence of fluid flow in open fractures rather than by the laminations themselves. The only data available to verify this statement are the fractures found in cores.

In the following section, to relate fractures with acoustic data, we construct an earth model based on fracture information provided from core analyses and rock physical properties derived from well logs and cores. Then we use the model to calculate attenuation responses to match the observed quality factor log.

c. Relation between fractures and horizontal attenuation

We now relate intrinsic attenuation to fluid flow effects in a fracture system of the siliceous shale at the Buena Vista Hills field. Attenuation was determined via velocity dispersion by integrating crosswell seismic data with well logs and cores. This concept relates the high frequency (~10 kHz) sonic logging velocity (V_{SONIC}) to the lower frequency (1000 Hz) observed crosswell velocity (V_{XWELL}) by

$$V_{SONIC} = V_{XWELL} + \Delta V_{SC} + \Delta V_I,$$

where del Vsc is the change in velocity due to the effects of elastic scattering and ΔV_I is the change in velocity associated with intrinsic attenuation. Theoretical considerations require that the term ΔV_I should always be positive, assuming that the sonic frequency is higher than the crosswell frequency.

The goal is to estimate the scattering part (Δ Vsc) and then extract the unknown intrinsic dispersion from the known data. Since Δ Vsc arises from stratigraphy, impedance, and anisotropy, it is possible to predict it using elastic models.

The resulting attenuation log based on this velocity dispersion algorithm represents the effective attenuation between the 653Z and 564 wells at the depth of interest as given in Figure 57. This figure also shows the correlation between the quality factor as a function of depth and lithology. The low Q zone between 4000-4100 ft. (1219-1250 m) correlates with the fractured Brown Shale as will be demonstrated later. In addition, in the same figure the horizontal P-wave velocity determined from zero-vertical offset waveforms is depicted by indicating a low velocity that correlates with the Brown Shale fractured zone.

The second low Q zone between 4150 and 4300 ft. (1264-1310 m) correlates with the sand and carbonate beds in the Antelope Shale. The attenuation due to the sands is represented by the Biot/squirt-flow mechanism. The application of this model suggests that, between 4150 and 4300 ft (1264-1310 m), horizontal attenuation is controlled by fluid flow in the sands, and the shales have a relatively low intrinsic attenuation compared to the permeable sand beds.

Now we evaluate the low Q anomaly in the Brown Shale Formation, between 4000 and 4100 ft. (1219-1250 m) in profile as shown in Figure 57. To relate the presence of fractures in the siliceous shale to seismic wave attenuation, we select the range of frequencies used in crosswell and sonic logs at the Buena Vista Hills field. We develop computer models based on rock physical parameters, well logs, and fracture information gathered from cores. We establish the model parameters using the works of Jacobs (1999) and Morea (1999). Jacobs provides information on sigmoidal en echelon fractures, and Morea provides information on joint-like, tectonic fractures. These two type of fractures correlate with the low Q and low velocity zone observed in the Brown Shale. To demonstrate quantitatively that fractures indeed affect the attenuation of acoustic and seismic waves, we simulate the low quality factor in the Brown Shale by using the proposed fracture model given in Figure 56.

We calculate the vertical permeability from core data based on fracture aperture and fracture density associated with joint-like tectonic fractures. We do not know the exact fracture density and the lengths of the possible fractures that may occur in the interwell region; however, we do know the range of fracture densities from cores [0-12 fractures per 20 ft. (6 m)]. We also know that average fracture aperture is about 0.03 mm.

As pointed out by Aguilera (1998), open fractures can greatly increase the total permeability of a rock. The intrinsic permeability of a fracture having a fracture width (w) in inches is expressed in darcies as follows,

$$k_i = 54 \times 10^{+6} w^2 \text{ darcy.}$$

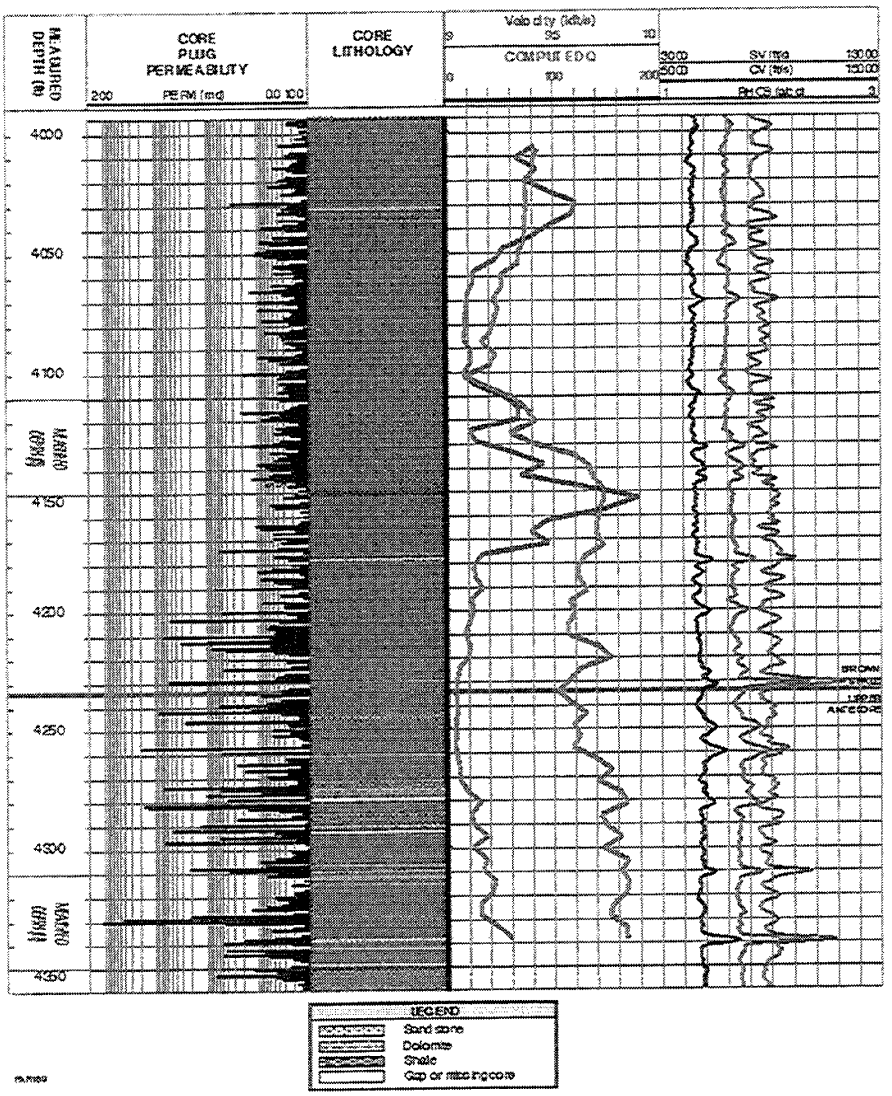

Figure 57. The petrophysics logs of a selected interval in the Antelope shale formation (4000- 4350 ft.), Buena Vista Hills field, Kern County, California. The Q and Vp logs are computed from velocity dispersion data (between 1000 and 10,000 Hz) and they are plotted versus measured depth.

The higher fracture permeability, k_i, only exists parallel to the strike of the fractures, while permeability perpendicular to fracture strike would be approximately equal to the matrix permeability. Fracture permeability, k_i, corresponds to single point properties. We can extend the fracture permeability, k_z, by representing bulk properties of the fracture system for one set of parallel fractures by using the equation

$$k_z = k_i \, w / d$$

where d is the distance between fractures.

For a fracture aperture of 0.03 mm (0.00122 in.) the intrinsic permeability is $k_i = 81$ darcies. Thus, for the minimum separation of one fracture every 20 inches (0.49 m) [based on a maximum fracture density of 12 fractures per 20 ft. (6 m)] or one fracture every 40 inches (0.98 m) [based on an average fracture density of 6 fractures per 20 ft. (6 m)], bulk permeabilities are $k_z = 5$ md and 2.5 md, respectively. The vertical permeability value of 5 md is about the same as the average permeability measured on sigmoidal veins by Jacobs (1999). For the modeling, we select permeabilities perpendicular and parallel to the fracture system to be $k_x = 50$ μd (determined from Figure 56) and $k_z = 5$ md, respectively.

To calculate attenuation as a function frequencies using the BISQ flow mechanism, the only unknown parameter is the squirt-flow length associated with the flow motion in the fracture. This parameter can be determined by calculating attenuation curves based on the model of Figure 56 and the parameters given in Table 9. Rock physical parameters such as stiffness constants, permeability, porosity, and fluid properties are applied to produce attenuation and dispersion curves for different azimuthal angles. In this example we vary the vertical squirt-flow length. Since the oil saturation of the study region is small, total attenuation is calculated assuming water as fluid.

Figures 58-60 illustrate attenuation curves computed with squirt-flow lengths of 1 cm to 3 cm, for an angle of incidence of 90 degrees to simulate energy propagating parallel to the stratification. The family of curves represents attenuation responses for azimuths of 0, 30, and 45 degrees. The figures show the attenuation curves calculated by considering these squirt-flow lengths at azimuthal angles between 0 and 45 degrees. Because we are interested in a frequency range of 1000 to 10,000 Hz, we calculate the quality factors in this frequency range. In general, as squirt-flow length increases, the attenuation peak is shifted towards the low frequency, and for azimuthal angles perpendicular to the fracture system, the attenuation is maximum. In the frequency range and azimuthal angles under study, the average Q value is between 14 and 60

.

Analysis of the modeling results demonstrates that the average Q = 20 in the frequency range of 1000 to 10,000 Hz fits the affective low Q anomaly in the Brown Shale. Thus, a squirt-flow length in the range of 1-2 cm in an open fracture produces the low Q anomaly observed in Figure 57. These squirt-flow lengths are less than the average joint-like 0.44-ft. (13-cm) long tectonic fractures, and near the average of the en echelon fractures (0.4 - 8cm). This implies that the fractures are partially saturated to allow fluid to flow in the fractures when seismic waves propagate at an angle of incidence transverse to a fracture zone. The attenuation curves

Table 9. Properties of the siliceous shale in the interval between 4000 and 4300 ft. (1219-1310 m) at the Buena Vista Hills field

Parameter		Unit	Formation Values
	c_{11}	(GPa)	11.3
Stiffness	c_{13}	(GPa)	5.4
constants	c_{33}	(GPa)	10.8
	c_{44}	(GPa)	2.7
	c_{66}	(GPa)	2.82
Porosity, ϕ		%	27
Grain modulus, K_s		(GPa)	26.76
Grain density, ρ_s		(g/cm^3)	1.9
Fluid velocity, v_f		(km/s)	1.5
Fluid density, ρ_f		(g/cm^3)	1
Viscosity, η		(poise)	0.01
Horizontal permeability, k_x		Darcy	50. e-6
Vertical permeability, k_z		Darcy	0.005
Squirt-flow length (x-axis)		(mm)	0.01
Squirt-flow length (z-axis)		(cm)	1 - 3

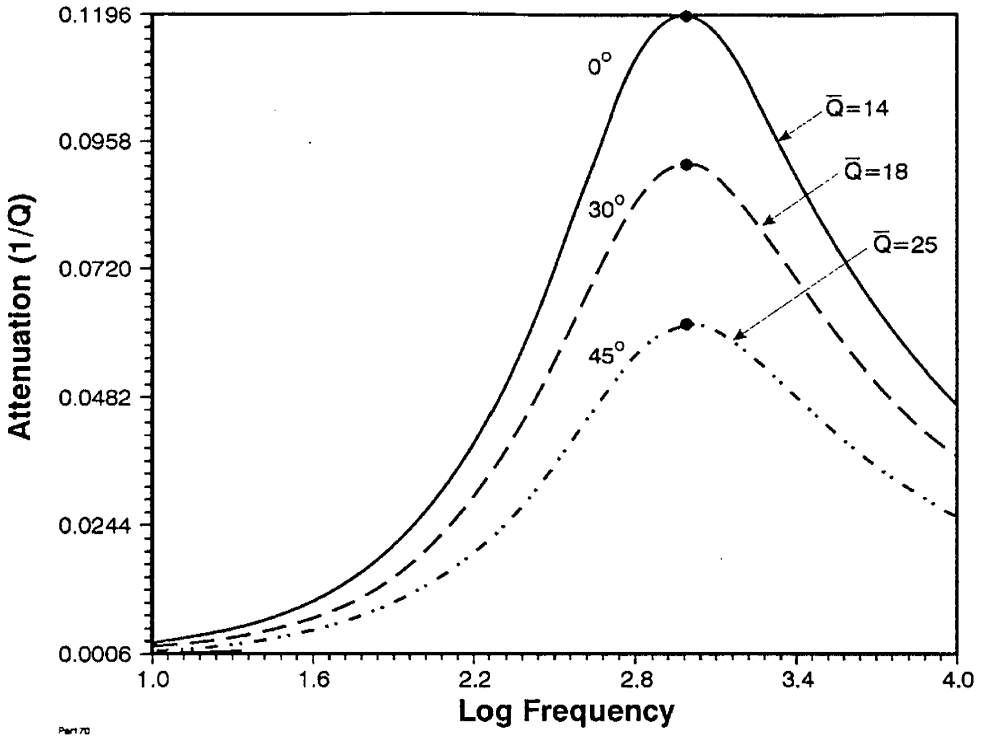

Figure 58. The effect of frequency and azimuth angles on attenuation illustrating the average quality factor in the interval of 1000 to 10,000 Hz at each azimuth, and a propagation angle of Φ = 90°, for a squirt-flow length of 1 cm.

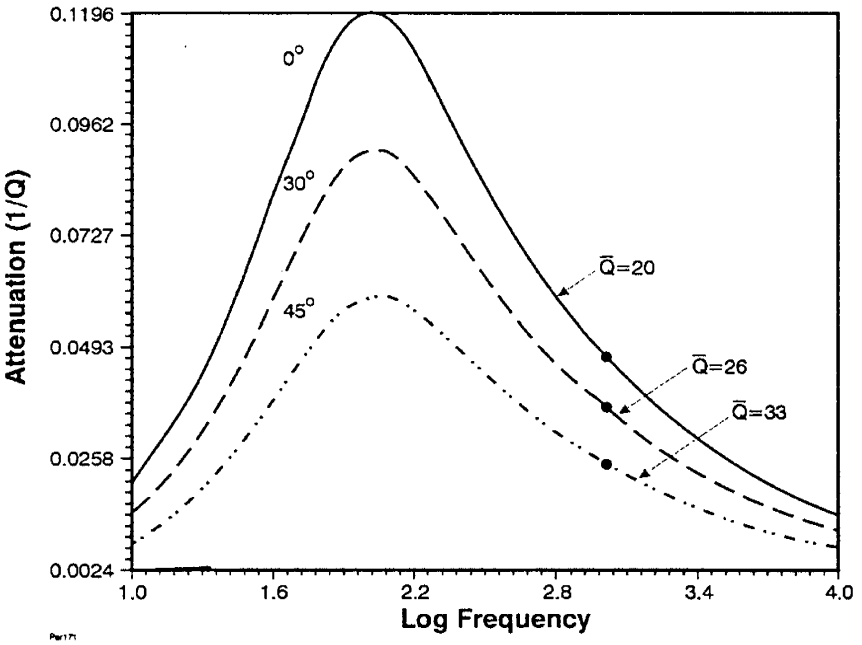

Figure 59. The effect of frequency and azimuth angles on attenuation illustrating the average quality factor in the interval of 1000 to 10,000 Hz at each azimuth, and a propagation angle of Φ = 90°, for a squirt-flow length of 2 cm.

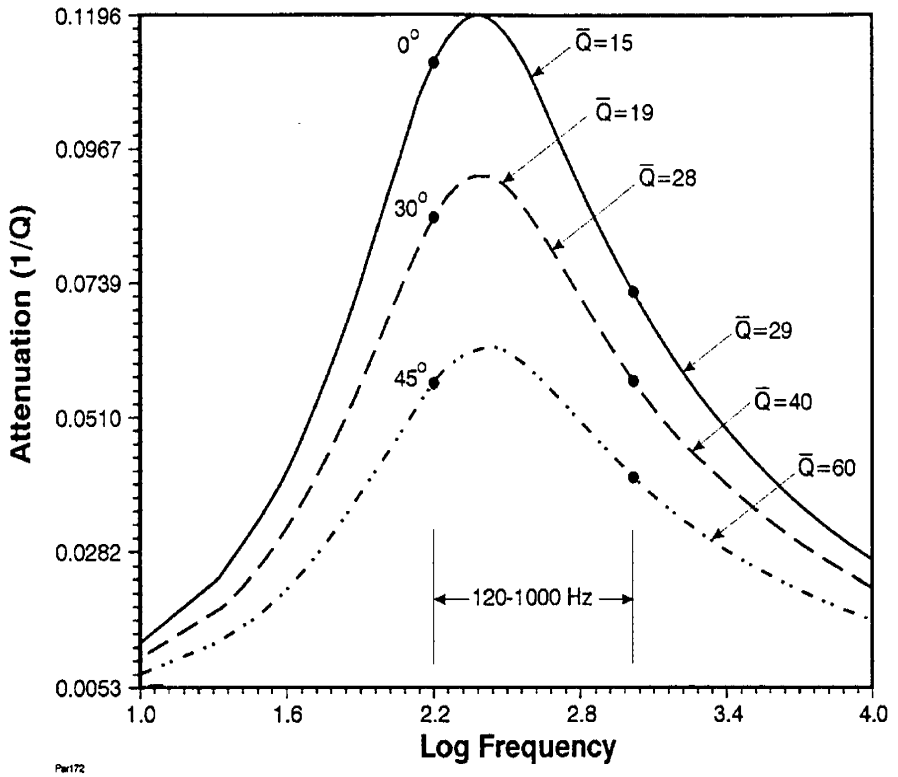

Figure 60. The effect of frequency and azimuth angles on attenuation illustrating the average quality factor in the interval of 1000 to 10,000 Hz at each azimuth, and a propagation angle of Φ = 90°, for a squirt-flow length of 3 cm.

calculated at azimuths of 30 and 45 degrees are computed to illustrate how the quality factor increases when a fracture zone is oriented at an azimuth angle that is not perpendicular to the direction of seismic wave propagation. The results of this interpretation are supported by the vertical open fractures encountered in cores at a depth of 4104 ft. (1250 m) (Morea, personal communication). In this zone the Q is above 25, associated with a squirt-flow length of 2 cm and an azimuthal angle of 30 degrees. In addition, an open fracture encountered at a depth of about 4130 feet correlates to a Q of 20 at that depth. We also calculate Q values of 15, 19 and 28 in the range of 120-1000 Hz, and illustrate in Figure 60 that t attenuation can be affected by fluid flow in fractures associated with a squirt-flow of 3 cm in the Brown Shale unit. This analysis suggests that a fracture permeability of 5 md and fractures having squirt-flow lengths between 1 and 3 cm comprise the most probable model to characterize the effective medium surrounding the borehole. In this case, the low Q of 20 represents a fractured zone in a low permeability medium oriented parallel to the borehole axis. Such a low Q, based on dispersion data, is expected from fractures in a high porosity compliant host rock (at the Buena Vista Hills formation, porosity is about 27 percent). This statement can be explained by the physics of acoustic waves in poroelastic media (Biot, 1962). In general, a P-wave propagating through a porous medium forces the pore spaces to alternately expand and contract. This local change in pore volume and pressure may cause the saturating fluid to flow from contracting to expanding pores such that the fluid is not at rest relative to the solid. Fractures oriented perpendicular to the direction of wave propagation allow fluid to

move from zones of high to low saturation. The squirt-flow mechanism is the dominant contributor to experimentally observed attenuation in sedimentary rocks (Boubier,1997).

d. Relating vertical attenuation to fluid flow effects at the Buena Vista Hills Reservoir

We found that attenuation based on sonic and crosswell seismic measurements indeed captures the intrinsic properties of the formation. Specifically, attenuation effects are addressed by analysis and interpretation of the two quality factor lows given in Figure 57. The results provide practical information that can be integrated with attenuation tomography imaging between wells (Guan, 1998). Since we know how Q can be related to fracture density at the borehole location, it may be possible to relate attenuation tomography data with fracture density. Thus, by extracting amplitude information from the multiple offset interwell seismic data set, we can map fracture density in the interwell region of the Buena Vista Hills field.

However, to demonstrate the applicability of VSP and surface seismic measurements to map the petrophysical properties at the Buena Vista Hills reservoir, we use a computer modeling program and the lithology given in Figure 57. The modeling program is based on the solution given in Appendix A. Thus, to find out whether constructive information can be obtained from attenuation measurements when VSP and/or surface seismic methods are used, it is necessary to study the effects of scattering and intrinsic attenuation for a plane wave propagating from the earth's surface. This can be done by implementing the Buena Vista Hills lithology to model the variability of the laminated siliceous shale as a function of depth. The plane wave propagation is typical for surface seismic and VSP measurements.

Vertical attenuation was computed using a poroelastic layered model, as addressed by Hackert and Parra (2000). The contribution of scattering attenuation was determined assuming a layered shale-sand sequence model, which is based on rock physical properties of the shales and sands from well 653Z cores and well logs (see Figure 61).

Intrinsic attenuation was modeled via the Biot/squirt-flow mechanism by comparing the flow in water-saturated sands (Figure 62a) to the flow in oil-saturated sands (Figure 62b). For the sands the squirt-flow length was 1 mm; the viscosity (η), density (ρ_f), and velocity (v_f) of the oil were 1.8 poise, 0.88 g/cm^3, and 1449 m/s, respectively. We assumed each layer is isotropic and homogeneous, in the solution given in Appendix A, to produce an earth model on the basis of the lithology and velocity/density logs given in Figure 61. Modeling and analysis results demonstrated that attenuation in the vertical direction is associated with combined scattering and fluid flow effects (Figure 62). That is, vertical attenuation is controlled by the average permeability of the siliceous laminated shales (on the order of millidarcies), squirt-flow, and the variability of the sand-shale sequence in the Antelope Shale. Here the lithology is predominantly diatomite shale, with many thin sand beds. The sand is the source of much of the lateral field permeability. In Figure 62, the simulated poroelastic attenuation profile is shown in red and the average elastic scattering background is shown as a green line. In the same figure, the predicted poroelastic attenuation profile based on an analytical solution incorporating the medium properties is shown as a blue curve. The results show that, in general, any attempt to use attenuation or

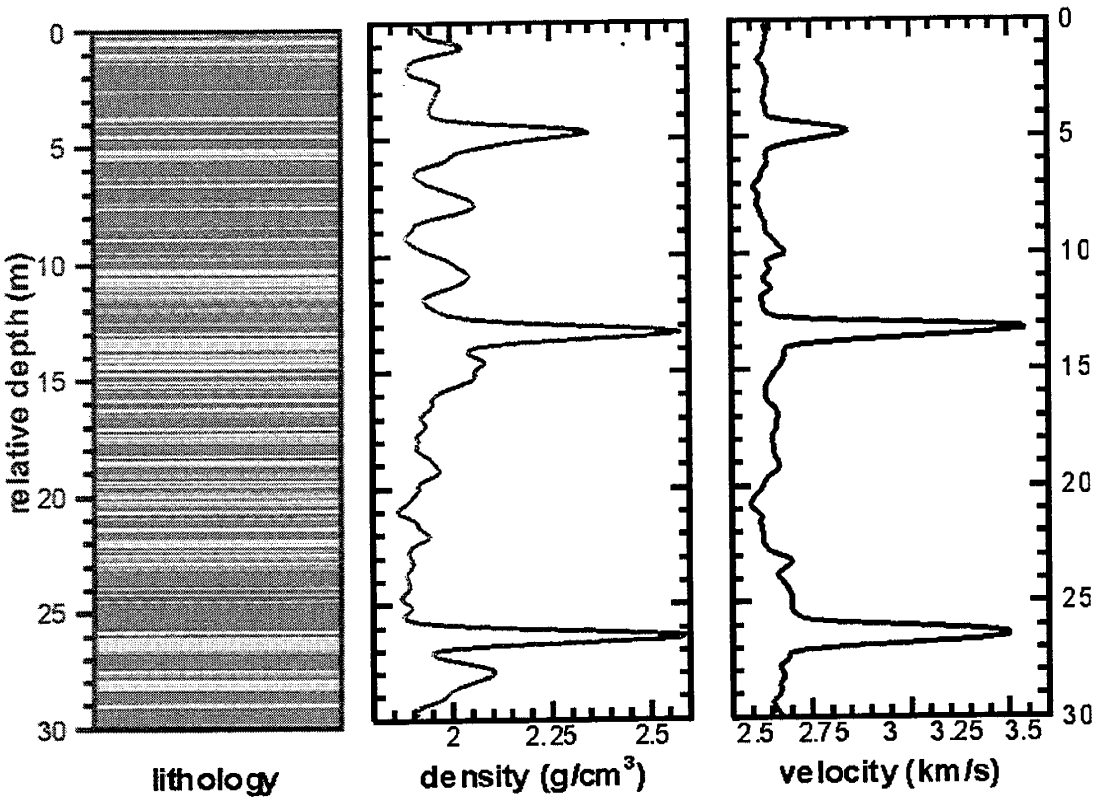

Figure 61. A lithological column of a sand-shale sequence and velocity/density well logs at the Buena Vista Hills field.

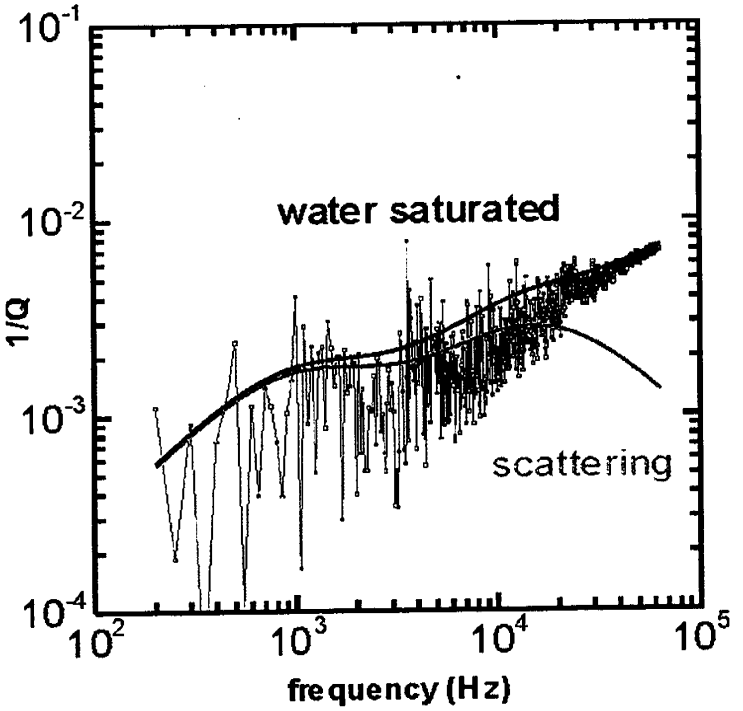

(a)

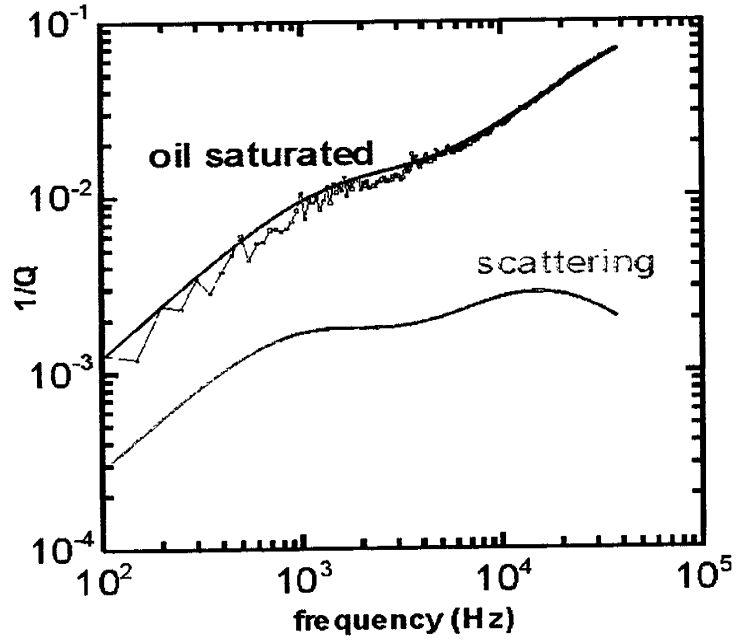

(b)

Figure 62. Attenuation of compressional waves including flow effects using (a) water saturation and (b) oil saturation. In both graphs, the dashed line represents BISQ attenuation in an unbounded sand body and the dotted line represents BISQ attenuation in an unbounded shale body; the dash-dot line is the scattering attenuation from stochastic medium theory, and the heavy solid line is the combined fluid and scattering attenuation based on the poroelastic theory.

dispersion to predict fluid flow effects must be based on relatively high frequency information. Surface seismic data are not practical for imaging the sand-shale laminated sequence at Buena Vista Hills. High frequency VSP or reverse VSP are more appropriate for use in this field. In this zone, a number of fractures are thin and perpendicular to the stratifications, so vertical propagation along the fractures does not contribute to vertical attenuation (Parra, 2000).

Finally, we address the contribution of the fractured laminated siliceous Brown Shale to vertical attenuation. We use the same model-based approach described above, with the exception that the squirt-flow mechanism that represents fractures is a tensor (see Figure 56). We apply the full solution of Appendix A, and we model the laminated Brown Shale in the interval between 4000 to 4100 ft. (1219-1250 m) with a squirt-flow length of 3 cm and a permeability of 5 md, to represent flow in fractures, and a host rock permeability of 0.1 md. The calculations demonstrate that the poroelastic contribution of the laminated shale is equivalent to an attenuation of 0.001 (or a Q value equal to about 1000). Since this interval does not have sand and carbonate layers, we expect its contribution to vertical attenuation will be less than the scattering contribution of the Antelope Shale to vertical attenuation, as shown in Figure 62. In addition, in this interval the isolated vertical fractures may not contribute to vertical attenuation for waves traveling perpendicular to the laminated siliceous shale. Therefore, vertical attenuation in the Brown Shale is controlled by the laminated siliceous shale.

C. Discussions and Conclusions

The modeling shows that the Brown Shale will attenuate very little seismic waves propagating from sources placed at the earth surface, the Q is of the order of 1000. However, the Brown Shale unit strongly attenuates seismic waves propagating parallel to the stratification, in the frequency range of sonic and cross well seismic. The attenuation high is due to the presence of en echelon and joint-like fractures in soft formation. The Brown Shale does not contain sand beds so the horizontal attenuation is indeed due to lateral fracture density in the interwell region.

The permeability values recorded with a minipermeater in cores from the Brown Shale are about the same order of magnitude as those obtained from fracture apertures and fracture densities of joint-like tectonic fractures in the same geological unit. The permeable zone formed by sigmoidal veins correlates with the low Q anomaly in the Brown Shale. This suggests that the vertical permeability of the Brown Shale between 4050 and 4100 ft. is about 5 md. This permeable zone has been related to a Q of 20 based on a squirt-flow in the range of 1-2cm. Since fractures have an average squirt-flow of about 6 cm, the permeable zone appears to be associated with fractures with patchy saturation with patches of dimension 1-3 cm.

In addition, the low Q correlates with a velocity low based on zero-vertical offset interwell seismic data. Although we do not have enough information on the interwell petrophysics, we assume that the low velocity is due to the high porosity encountered in cores where sigmoidal veins occur. The only evidence we have is that based on the thin section analysis done by Jacobs (1999). Porosity can reach up to 70 percent in the boundary between the siliceous shale host rock and the veins.

On the other hand, modeling results in the Antelope Shale for a plane wave propagating from the surface demonstrate that vertical attenuation is more sensitive to sand beds saturated with oil than to those saturated with water. The quality factor deduced from modeling is about 100. This suggests that when a source is placed at the earth's surface, the Antelope Shale can attenuate seismic waves more than the Brown Shale. Alternatively, for waves propagating parallel to stratification and perpendicular to open fractures between 4159 and 4250 ft. in the Antelope Shale, the Q is about 18 to 20, which is associated with a vertical permeability of 5 md. Thus, the presence of vertical open fractures in the Antelope Shale Formation has produced a Q about 20 times smaller than the Q associated with vertical attenuation. This indicates that crosswell seismic measurement is the most appropriate technique to map fracture zones and flow units in the interwell region of the Antelope Shale. In particular, high resolution attenuation measurements have the potential to map lateral fracture density at the Buena Vista Hills field. The layer sequence responses are significant when attempting to understand the differences between vertical and horizontal attenuation in terms of reservoir characterization, and when evaluating whether VSP or surface seismic measurements are sensitive to fluid flow effects at the Buena Vista Hills field.

References

Aguilera, R., 1998, Geological aspects of naturally fractured reservoirs: The Leading Edge, **17**, 1667- 1670.

Akbar, N., Mavko, G., Nur, A., and Dvorkin, J., 1994, Seismic signatures of reservoir transport properties and pore fluid distribution: Geophysics, **59,** 1222-1236.

Bourbie, T., Coussy, O., and Zinszner, B., 1987, Acoustics of Porous Media (Editions Technip, Paris), 220-228.

Dvorkin, J. and Nur, A., 1993, Dynamic poroelasticity: a unified model with the squirt and Biot mechanisms: Geophysics, **58,** 523-533.

Guan Y.W., Harris, J.M., Magalhaes, C.G., Julander, D. and Morea, M., 1998, Buena Vista Hills 3-D attenuation and velocity tomography: 68th Ann. Internat. Mtg., Soc. Expl. Geophys., Expanded Abstract.

Jacobs, J.L., 1999, Characterization and formation of veins and associated structures in siliceous shales and their impact on hydrocarbon flow: Master's Thesis, Department of Geological and Environmental Sciences, Stanford University.

Hackert, C.L., and Parra, J.O., 2000, Attenuation of acoustic plane waves from multi-scale scattering and pore flow in heterogeneous permeable media: J. Acoust. Soc. Am., **107**, 3028-3034.

Hackert, C.L., Parra, J.O., Brown, R.L., and Collier, H.A., 2001, Characterization of dispersion, attenuation, and anisotropy at the Buena Vista Hills field, California: Geophysics, **66** (in press).

Morea, M.F., 1999, Advanced reservoir characterization in the Antelope Shale to establish the viability of CO_2 enhanced oil recovery in California's Monterey Formation siliceous shales: Report DOE/BC/1493 8-12, National Petroleum Technology Office, Department of Energy, Tulsa, Oklahoma.

Parra, J.O., 2000, Poroelastic model to relate seismic wave attenuation and dispersion to permeability anisotropy: Geophysics, **65,** 202-201.

Parra, J.O., 1997, The transversely isotropic poroelastic wave equation including the Biot and squirt-flow mechanism: theory and application: Geophysics, **62**, 309-318.

Parra, J.O., 1991, Analysis of elastic wave propagation in stratified fluid-filled porous media for interwell seismic applications: J. Acoust. Soc. Am., **90**, 2557- 2575.

Parra, J.O., and Xu, P.-C., 1994, Dispersion and attenuation of acoustic guided waves in layered fluid-filled porous media: J. Acoust. Soc. Am., **95**, 91-98.

Parra, J.O., Hackert, C.L., Brown, R.L., and Collier, H.A., 1998, Estimation of components of elastic scattering and intrinsic attenuation via well control at the Buena Vista Hills field: 68th Ann. Internat. Mtg., Soc. Expl. Geophys., Expanded Abstract, 256-259.

Parra, J.O., Collier, H.A., Datta-Gupta, A., Owen, T., Peddibhotla, S., Xu, P.-C., and Zook, B., (1997), Characterization of fractured reservoirs using static and dynamic data: from sonic and 3D seismic to permeability distribution: Report DOE/DC91008 (DE96001284), National Petroleum Technology Office, Department of Energy, Tulsa, Oklahoma.

Schmidt, H., and Tango, G., 1986, Efficient global matrix approach to the computation of synthetic seismograms : Geophys. J. Astron. Soc., **84**, 331-359.

APPENDIX A

Plane Wave Solution of an Arbitrary Plane in a Layered Transversely Isotropic Poroelastic Medium with X Being the Axis of Symmetry

The basic plane wave solution for an arbitrary plane in a transversely isotropic poroelastic unbounded medium with x being the axis of symmetry is given by Parra (2000). This solution is important when constructing the multilayer earth model. The following derivation is based on the theory developed by Parra (2000).

The layer medium formulation

To establish the general equations for waves in layered poroelastic media we consider an incident plane wave formed by up-going and down-going waves, respectively. We assume that the displacement vector (u_x, u_y, u_z) and the pressure (p) within a layer are given by

$$\begin{Bmatrix} u_x \\ u_y \\ u_z \\ p \end{Bmatrix} = \begin{bmatrix} 1 & 1 & 1 & 0 & 1 & 1 & 1 & 0 \\ \kappa_1 R_1 & \kappa_2 R_2 & \kappa_3 R_3 & 1 & \kappa_5 R_5 & \kappa_6 R_6 & \kappa_7 R_7 & 1 \\ R_1 & R_2 & R_3 & R_4 & R_5 & R_6 & R_7 & R_8 \\ Q_1 & Q_2 & Q_3 & 0 & Q_5 & Q_6 & Q_7 & 0 \end{bmatrix} \begin{Bmatrix} A_1 e^{-\delta z} \\ A_2 e^{-\epsilon z} \\ A_3 e^{-\gamma z} \\ A_4 e^{-\nu z} \\ A_5 e^{\delta z} \\ A_6 e^{\epsilon z} \\ A_7 e^{\gamma z} \\ A_8 e^{\nu z} \end{Bmatrix} e^{i(\xi_1 x + \xi_2 y)} \tag{1}$$

In equation (1) the wave propagation numbers δ, ϵ, and γ (see Parra ,1991; Parra and Xu, 1994), as well as the ratio $\kappa_j = u_y/u_z$ for j = 1,2,3,5,6,7, are for fast and slow quasi-P and quasi-SV waves. R_4,

$$\begin{aligned} \kappa_1 &= -i\frac{\xi_2}{\delta} \quad \kappa_2 = -i\frac{\xi_2}{\epsilon} \quad \kappa_3 = -i\frac{\xi_2}{\gamma} \\ \kappa_5 &= i\frac{\xi_2}{\delta} \quad \kappa_6 = i\frac{\xi_2}{\epsilon} \quad \kappa_7 = i\frac{\xi_2}{\gamma} \\ R_4 &= -\frac{\nu}{i\xi_2} \quad R_8 = \frac{\nu}{i\xi_2} \end{aligned} \tag{2}$$

R_8 is the ratio u_z/u_y for the SH wave, respectively. Because of the symmetry of the elastic and permeable properties in the *y-z* plane, we have

In equation (2), ζ, ξ_1, and ξ_2 are wave numbers that are functions of the azimuthal angle Ω and the incident angle Φ (see Figure 53). The coefficients $\{R_i, Q_i\}$, j =1,2,3,5,6,7 in equation (1) represent the ratios $\{u_z/u_y\}$ and $\{ p/u_x\}$, and they can be obtained from equation (11) of Parra (2000) by

$$R_j = \frac{\Delta_R}{\Delta} \qquad Q_j = \frac{\Delta_Q}{\Delta} \qquad j = 1,2,3,5,6,7 \tag{3}$$

dividing the two sides of each equation by u_x. These coefficients are

$$\begin{aligned}
\Delta &= a_{30}a_{44} - a_{34}a_{40} \\
\Delta_R &= -a_{31}a_{44} + a_{41}a_{34} \\
\Delta_Q &= -a_{41}a_{30} + a_{31}a_{40} \\
a_{30} &= a_{33} + \kappa_j a_{32} \\
a_{40} &= a_{43} + \kappa_j a_{42} \\
a_{31} &= (C_{13} + C_{44})\xi_1\zeta \\
a_{32} &= (C_{12} + C_{66})\xi_2\zeta \\
a_{33} &= C_{44}\xi_2^2 + C_{66}\xi_2^2 + C_{11}\zeta^2 - \omega^2\overline{\rho_1} \\
a_{34} &= i\zeta\overline{\alpha_1} \\
a_{41} &= i\xi_1\overline{\alpha_3} \\
a_{42} &= i\xi_2\overline{\alpha_1} \\
a_{43} &= i\zeta\overline{\alpha_1} \\
a_{44} &= \theta_3\xi_1^2 + \theta_1(\xi_2^2 + \zeta^2) + \beta
\end{aligned} \tag{4}$$

In equation (4), α_1 and α_2 are elements of the second-rank elastic tensor α; β is the compressibility coefficient, and θ is the normalized frequency-dependent generalized Darcy tensor; C11, C12, C13, C44, and C66 are elements of the stiffness constants tensor, **C**.

To solve the general boundary value problem for an arbitrary incident plane wave (see Parra and Xu, 1994), it is necessary to have expressions of all stresses and volumetric flux components in three dimensions. These expressions can be obtained directly from the constitutive relations given by

These expressions are derived in terms of up-going and down-going waves, and they are given explicitly by Parra et al. (1997). To satisfy the wave field at the layer interfaces, the boundary

$$\begin{Bmatrix} \tau_{xx} \\ \tau_{yy} \\ \tau_{zz} \end{Bmatrix} = \begin{bmatrix} C_{33} & C_{13} & C_{13} \\ C_{13} & C_{11} & C_{12} \\ C_{13} & C_{12} & C_{11} \end{bmatrix} \begin{Bmatrix} \frac{\partial u_x}{\partial x} \\ \frac{\partial u_y}{\partial y} \\ \frac{\partial u_z}{\partial z} \end{Bmatrix} - p \begin{Bmatrix} \overline{\alpha_3} \\ \overline{\alpha_1} \\ \overline{\alpha_1} \end{Bmatrix}$$

$$\begin{Bmatrix} \tau_{yz} \\ \tau_{xz} \\ \tau_{xy} \end{Bmatrix} = \begin{bmatrix} C_{66} & 0 & 0 \\ 0 & C_{44} & 0 \\ 0 & 0 & C_{44} \end{bmatrix} \begin{Bmatrix} \frac{\partial u_y}{\partial z} + \frac{\partial u_z}{\partial y} \\ \frac{\partial u_x}{\partial z} + \frac{\partial u_z}{\partial x} \\ \frac{\partial u_x}{\partial y} + \frac{\partial u_y}{\partial x} \end{Bmatrix} \tag{5}$$

$$\begin{Bmatrix} w_x \\ w_y \\ w_z \end{Bmatrix} = \begin{Bmatrix} a_3 u_x \\ a_1 u_y \\ a_1 u_z \end{Bmatrix} + \begin{Bmatrix} b_3 \frac{\partial p}{\partial x} \\ b_1 \frac{\partial p}{\partial y} \\ b_1 \frac{\partial p}{\partial z} \end{Bmatrix}$$

conditions required expressions for the displacement components (u_x, u_y, u_z), the vertical component of displacement relative to the fluid (w_z), and the stress components (τ_{xx}, τ_{yz}, τ_{zz}). Thus, the boundary value problem can be solved for a layered porous medium formed by N parallel horizontal layers overlying a uniform half-space. We assume the *j*th layer has a thickness $h_j = z_j - z_{j-1}$, and that it is bounded by the planes $z = z_{j-1}$ and $z = z_j$. The matrix properties of the *j*th layer are denoted by the grain density, $\rho_s^{(j)}$, the second-range tensor, $\alpha^{(j)}$, the compressibility $\beta^{(j)}$, the stiffness tensor $C^{(j)}$, the porosity, $\phi^{(j)}$, and the horizontal and vertical permeability and squirt-flow lengths $k_x^{(j)}$ and $k_z^{(j)}$, and $R_x^{(j)}$ and $R_z^{(j)}$, respectively. Saturant fluid parameters are viscosity, fluid velocity, and fluid density ($\eta^{(j)}$, $v_f^{(j)}$, and $\rho_f^{(j)}$, respectively).

The global matrix solution

The above analysis provides the formulation for wave motion for the *j*th layer in terms of eight coefficients. To apply the boundary conditions of continuity for fluid pressure, displacements, and stress fields, we write field components and pressure for *j*th layer as follows

$$u_j = J_j \, e_j \, A_j, \tag{6}$$

where

$$u_j = [\, u_x^{(j)},\ u_y^{(j)},\ u_z^{(j)},\ p^{(j)},\ \tau_{xx}^{(j)}\ \tau_{yz}^{(j)}\ \tau_{zz}^{(j)},\ w_z^{(j)}]^T.$$

The vectors e and A and the matrix J are obtained from equation (1) and the expanded expressions of equation (5). To avoid precision problems caused by the growing exponential in individual matrices for large wave numbers, the global matrix method is implemented (Schmidt and Tango, 1986; Mal, 1988), as an alternative to the traditional propagation approach, to determine reflection coefficients and find the solution of the vector wave displacement and pressure.

Denoting m as the label of layers, we define a full space consisting of an upper half-space (m = 1), (N - 1) layers of finite thickness (m = 2, 3,.., N) and a lower half-space (m = N + 1). The global matrix analysis based on equation (6) is written in its vector and matrix form

$$\{u_m(z)\} = [J_m]\,[e_m(z)]\,\{A_m\}, \tag{7}$$

For m = 2, 3, ..., N, the vector $[A_m]$ contains the unknown wave coefficients of wave propagation in both the positive and negative z directions in the layer. Alternatively, due to the radiation conditions, the upper half-space m = 1 contains only the up-going part of the wave coefficients, and the lower half-space m = N + 1 contains only the down-going part. As a result, the corresponding $[J_1]$, $[J_{N+1}]$, $[e_1(z)]$, and $[e_{N+1}(z)]$ should take their reduced form.

In the global matrix formulation, the boundary conditions at the layer interfaces are satisfied in the form of difference of field quantities across the interface. The conditions for the mth interface are represented by using equation (6) as follows:

$$[J_{m+1}]\,[e_{m+1}(z)]\,\{A_{m+1}\} - [J_m]\{e_m(z)]\,\{A_m\} = \{u_{m+1}(z)\} - \{u_m(z_m)\}, \tag{8}$$

where z_m is the coordinate of the interface between the mth and (m+1)th layers. After some algebraical arrangement, a linear system of equations is produced, which is given by

$$[G]\,[A] = \{B\}. \tag{9}$$

The global matrix [G] is composed of submatrices obtained from $[J_m]$, $[e_m(z_m)]$, and $[e_{m+1}(z_m)]$, for m = 1, 2, ..., N + 1. In this case equation (9) includes the upper and lower half-space. These submatrices contain coefficients associated with the physical properties of the skeleton and fluid of the layered poroelastic medium as well as the coordinates of the interfaces. The global vector B represents the external excitation (e.g., incident plane waves) in the form of jump conditions at the interfaces z_m, m = 1, 2, ..., N + 1, which are obtained from the right-hand side of equation (8). The global vector {A} is a collection of the unknown wave coefficients with down-going and up-going waves in the layers. The dimensions of the global matrix [G] are 8(N + 1) x 8(N + 1).

Thus, reflection and transmission coefficients can be obtained from the solution of the global matrix equation given by equation (9). The number of up-going and down-going waves in a layer is eight: four down-going and four up-going waves. These waves are the fast and slow qP, qSV, and qSH waves.

IV. WORK PLAN FOR PHASE III

We have slightly modified the original by proposed Phase III. We will conduct a more aggressive and practical approach to relate the pore structure with the field scale by including crosswell seismic reflection data that will be acquired at South Florida. This data will be acquired in the first part of Phase III and will be analyzed, modeled and integrated in the second part of Phase III. In addition, we will continue analyzing the data from Siberia Ridge. Following are the major tasks that will be performed in Phase III.

Task 1. Attenuation measurements

An understanding of the intrinsic and scattering attenuation in reservoir rock has been an important goal in this project. We have developed and applied methods to simulate the scattering attenuation using deterministic and stochastic responses at the Buena Vista Hills and at the Siberia Ridge fields. We have conducted these studies at the borehole and field scales. In phase III we have the opportunity to team with Lawrence Berkeley Laboratories. This organization will conduct attenuation measurements at the core scale to determine the Q associated with the vuggy carbonates at different saturations and confining pressures. We expect to implement attenuation mechanisms that can be used to extract the vuggy porosity from sonic logs. As a result, in this task we will implement techniques to invert monopole full waveform sonic. The main steps that we expect to accomplish are as follow:

(A) At the core scale based on two long cores about 1 m in length:
  (1) Core preparations
  (2) Ultrasonic measurements
  (3) Petrography

(B) At the borehole scale:
  (1) Implement algorithm to calculate Q from sonic logs
  (2) Simulate full waveform sonic logs based on the well log information
  (3) Calculate Q from monopole real data

(C) Calibrate Q log with the Q from core measurements.

Task 2. Characterization of the pore structure of vuggy carbonates

We have 18 core plugs from the carbonate reservoir to be studied at the pore and core scales. The objective is to characterize the rock fabric of vuggy carbonates using different measurement and imaging techniques to interpret NMR, resistivity, and acoustic well logs and to improve the calibration of NMR well logs. In addition, in this Task we will develop new permeability equations based on the NMR core measurements to predict flow units from NMR well logs. The steps to accomplished this goal:

(A) Conduct NMR measurements and analysis.
(B) Conduct ultrasonic measurements.
(C) Conduct resistivity measurements.
(D) Produce OM and SEM images.
(E) Conduct petrography.

Task 3. Digital image processing

In this task we will digitally process the optical macroscopic and SEM images to determine the pore size distributions and the pore shapes. The objective will be to relate these pore scale attributes to permeability. We expect to find how image processing can give insight on the rock permeability, so we can evaluate NMR log measurements. The results of this task will be used to calculate synthetic NMR core and well log signatures in Task 4. This task includes the following subtasks:

(A) Process images produced in Task 1.
(B) Process images produced in Task 2.
(C) Correlate pore sizes and shapes with permeability and petrography.

Task 4. NMR modeling

A theoretical solution will be implement to calculate NMR signatures. The solution will consider the coupling between the micropores, macropores and vugs. The pore size distribution that will be produced in Task 3 will be used to calculate the synthetics. This task includes the following subtasks:

(A) Implement solution to calculate NMR synthetics.
(B) Calculate synthetics based on the results of Task 2.
(C) Compare synthetic with observed NMR signatures at the core and borehole scales.

Task 5. Well log analysis and calibration

The variable T2 cut offs produced in Task 2 will be used to calibrate the NMR well log that was recorded in well PBF 10. The new permeability well log will be compared with those permeability logs based on one T2 cut-off, and T2 cut-offs derived from nine core plugs. The new permeability well log also will be integrated with the Vp , Vs, density, and porosity well logs based on flow unit indicators. The objective will be to characterize the formation surrounding the borehole. In this task we will relate the Q logs derived in Task 1 to permeability. The Vp/Vs relations developed at the borehole scale will be used to convert velocity and impedance cross sections (derived in Task 6) to permeability and porosity profiles in the interwell region. This task includes the following subtasks:

(A) Re-calibrate the NMR well logs with new T2 cut-offs based on the 18 plugs.
(C) Calculate permeability logs based on a new set of T2 cut-offs.
(D) Process and analyze all the well logs in well PBF10.

Task 6. Integration between borehole and interwell data

In this task we will apply all the computer modeling techniques that were developed in Phases I and II as well as in previous DOE project and internal SwRI projects. The objective is to validate these programs with real data and with an understanding of the geology. A second objective is to apply the concepts developed in the present project to address real reservoir characterization problems. The steps involved in this process are:

(A) Characterize the South Florida carbonate:
   (1) Conduct high resolution cross well seismic measurements
   (2) Process multiple offset seismic data
   (3) Perform finite different modeling of crosswell seismic data
   (4) Invert reflection data
   (5) Produce permeability and porosity cross sections based on well log information

(B) Complete characterization of the Siberia Ridge field using data from a new well: SB 27-4.
   (1) Construct a reservoir model based on wells SRU 5-4 and SRU 27-4
   (2) Correlate Vp, Vs, and density with permeability and porosity for each lithological unit
   (3) Determine the flow units associated with fractures and the matrix porosity based on the FMI data
   (4) Establish the fracture orientations in the reservoir based on the FMI and core data
   (5) Calculate dipole sonic full waveforms based on fracture-induced anisotropy information and a dipole modeling program
   (6) Verify the dipole code with observed dipole sonic data recorded in well SB 27-4

Task 7. Technology transfer and project coordination

All papers and presentations (oral and posters) will be included on the project Home Page. One paper including the integration of acoustic and NMR data with core images will be presented at a meeting of the Society of Petroleum Well Log Analysts in June 2001 in Houston. The ultrasonic modeling/CT images and the acoustic sonic modeling/CT images will be presented in two papers at the SEG International Meeting in September 2001 in San Antonio. We will prepare three poster presentations for these two conferences. We are currently collaborating with the University of Texas by providing project results and core image data to a U.T. student. We are anticipating strong collaborations with other students. We are also collaborating with Lawrence Berkeley Laboratories. Core data and results of our core analysis will be used to support the results of the attenuation core measurements that one student at LBL will perform. In addition, we will collaborate with TomoSeis by providing the results of core and well log analyses to image the interwell region at the South Florida carbonate aquifer. We are expecting that all the collaboration efforts will result in a successful integration of the different measurements.